

DOT/FAA/TC-TT16/44

Federal Aviation Administration
William J. Hughes Technical Center
Aviation Research Division
Atlantic City International Airport
New Jersey 08405

An Anisotropic and Asymmetric Material Model for Simulation of Metals Under Dynamic Loading

November 2016

Technical Thesis

The research described in this report was funded by the FAA as part of its mission to improve aircraft safety. The views and opinions expressed are those of the author alone and do not necessarily represent the views of the FAA. The FAA assumes no liability for the contents or use thereof. The FAA has not edited or modified the contents of the report in any manner.

This document is available to the U.S. public through the National Technical Information Services (NTIS), Springfield, Virginia 22161.

This document is also available from the Federal Aviation Administration William J. Hughes Technical Center at actlibrary.tc.faa.gov.



U.S. Department of Transportation
Federal Aviation Administration

NOTICE

This document is disseminated under the sponsorship of the U.S. Department of Transportation in the interest of information exchange. The U.S. Government assumes no liability for the contents or use thereof. The U.S. Government does not endorse products or manufacturers. Trade or manufacturers' names appear herein solely because they are considered essential to the objective of this report. The findings and conclusions in this report are those of the author(s) and do not necessarily represent the views of the funding agency. This document does not constitute FAA policy. Consult the FAA sponsoring organization listed on the Technical Documentation page as to its use.

This document represents the views of the author and does not represent the views of the FAA. The FAA assumes no liability for the contents or use thereof. The FAA has not edited or modified the contents of the report in any manner.

This report is available at the Federal Aviation Administration William J. Hughes Technical Center's Full-Text Technical Reports page: actlibrary.tc.faa.gov in Adobe Acrobat portable document format (PDF).

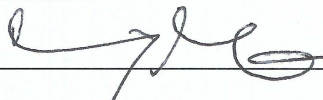

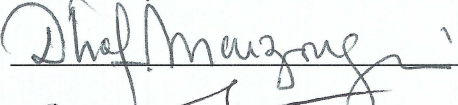



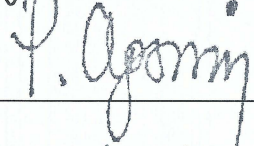
1. Report No. DOT/FAA/TC-TT16/44		2. Government Accession No.		3. Recipient's Catalog No.	
4. Title and Subtitle An Anisotropic and Asymmetric Material Model for Simulation of Metals Under Dynamic Loading				5. Report Date November 2016	
				6. Performing Organization Code	
7. Author(s) Sean Harrison Haight				8. Performing Organization Report No.	
9. Performing Organization Name and Address The George Mason University 4400 University Drive, MSN 4C6 Fairfax, VA 22030				10. Work Unit No. (TRAIS)	
				11. Contract or Grant No. 13-G-0020	
12. Sponsoring Agency Name and Address U.S. Department of Transportation Federal Aviation Administration Air Traffic Organization Operations Planning Office of Aviation Research and Development Washington, DC 20591				13. Type of Report and Period Covered Final Report	
				14. Sponsoring Agency Code ANE-110	
15. Supplementary Notes The FAA William J. Hughes Technical Center Aviation Research Division Technical Monitor was Dan Cordasco.					
16. Abstract The purpose of this research is to develop a fully-tabulated, anisotropic, asymmetric, strain rate, and temperature dependent material model for solid finite elements. Physical testing of several metallic materials has shown them to have anisotropic (or orthotropic) characteristics. While many material models in finite element codes currently have anisotropic options, they tend to focus on material forming applications – not crash and impact analysis. Unlike most available anisotropic forming material models, this model includes: rate dependency, temperature dependency, tabulated hardening (as opposed to parameterized inputs), mesh regularization, and can be utilized with three-dimensional solid elements. The implementation of this anisotropic model is an extension of the currently existing Generalized Yield Surface (GYS) variant of the Tabulated Johnson-Cook material model. This new model builds upon the previously available features of both of these well-established material models. Strain rate and temperature dependencies are utilized as independent tabulated values. Yield curves for tension, compression and shear are also tabulated and independent. Isotropic failure is retained from the Tabulated Johnson-Cook model as a function of triaxiality, Lode parameter, strain rate, temperature and element size. Lastly, tabulated plasticity for tension and compression allows the user to specify yield stress in the 0-degree, 45-degree, 90-degree, and thickness directions (as a function of strain rate). Therefore, this model applies to thick orthotropic metallic plates as it is assumed that a thickness direction can be recognized in the structure (although no plane state of stress is assumed) and that the response under 135-degree and 45-degree are identical. Due to the fully tabulated nature of the material law, rate and temperature dependency and asymmetry are all orthotropic in nature which is a unique feature of this current approach. Physical testing (tension and compression) of Al-2024 and Ti-6Al-4V specimens were used to validate the development of this material model. Using a single material model for each metal, the author was able to replicate test results in each specimen direction. Lastly, this model was used to simulate ballistic impacts of a 0.25 inch Ti-6Al-4V plate and compared to other models with comparable inputs. This material model is available in LS-DYNA as MAT264.					
17. Key Words LS-DYNA, Tabulated Material Failure, Triaxiality, LODE Angle, MAT_Tabulated_Johnson_Cook_Ortho_Plasticity, MAT264,			18. Distribution Statement This document is available to the U.S. public through the National Technical Information Service (NTIS), Springfield, Virginia 22161.		
19. Security Classif. (of this report) Unclassified		20. Security Classif. (of this page) Unclassified		21. No. of Pages 176	
				22. Price	

AN ANISOTROPIC AND ASYMMETRIC MATERIAL MODEL FOR SIMULATION
OF METALS UNDER DYNAMIC LOADING

by

Sean Harrison Haight
A Dissertation
Submitted to the
Graduate Faculty
of
George Mason University
in Partial Fulfillment of
The Requirements for the Degree
of
Doctor of Philosophy
Computational Sciences and Informatics

Committee:

	Dr. Cing-Dao "Steve" Kan, Dissertation Director
	Dr. Fernando E. Camelli, Committee Member
	Dr. Dhafer Marzougui, Committee Member
	Dr. Chi Yang, Committee Member
	Dr. Kevin Curtin, Acting Department Chair
	Dr. Donna M. Fox, Associate Dean, Office of Student Affairs & Special Programs, College of Science
	Dr. Peggy Agouris, Dean, College of Science
Date: <u>4/15/2016</u>	Spring Semester 2015 George Mason University Fairfax, VA

An Anisotropic and Asymmetric Material Model for Simulation of Metals under
Dynamic Loading

A Dissertation submitted in partial fulfillment of the requirements for the degree of
Doctor of Philosophy at George Mason University

by

Sean Harrison Haight
Master of Science
The George Washington University, 2013
Bachelor of Science
Texas Christian University, 2009

Director: Cing-Dao “Steve” Kan, Professor
Department of Physics and Astronomy

Spring Semester 2016
George Mason University
Fairfax, VA



This work is licensed under a [creative commons attribution-noncommercial 3.0 unported license](https://creativecommons.org/licenses/by-nc/3.0/).

DEDICATION

This dissertation is dedicated to my wife, Veronica, who has inspired, motivated and supported me throughout this research.

ACKNOWLEDGEMENTS

I would like to personally thank Professor Cing-Dao “Steve” Kan and Paul Du Bois for their support during this research. Without them, this work would not have been possible and I am forever thankful for their efforts. They have both provided all the necessary resources and have always made themselves, and their vast knowledge, available to me. I have learned so much from these two scholars that I will carry with me for the rest of my life.

I would also like to thank the faculty and staff of the Center for Collision Safety and Analysis (CCSA) and the George Mason University. They have provided academic, financial, and technological support during my graduate studies.

I am also thankful to my dissertation committee at George Mason University. Professor Cing-Dao “Steve” Kan, Professor Dhafer Marzougui, Professor Chi Yang, and Professor Fernando Camelli have all been extremely helpful during my academic career and have each prepared me for research of this magnitude.

I would like to thank William Emmerling and the Federal Aviation Administration’s Aircraft Catastrophic Failure Prevention Research Program for their technical and financial support during this research. Additionally, I would like to thank Dr. Kelly Carney and the members of the NASA Glenn Research Center for their technical support.

I would also like to acknowledge Professor Amos Gilat and Dr. Jeremy Seidt of the Ohio State University for their assistance and expertise in material testing. They have also been very helpful in providing much of the test data used in this research. I would also like to thank all the members of the FAA Aerospace Working Group including Dr. Tom Vasko, Dr. Daniel Cordasco, Dr. J. Michael Pereira, Dr. C. K. Park, Dr. Douglas Wang, and Stefano Dolci.

Special thanks to Gunther Blankenhorn and Dr. John O. Hallquist of the Livermore Software Technology Corporation (LSTC). They were very helpful in providing the tools necessary for completing the computational parts of this dissertation.

I would like to personally thank the friends and colleagues that have supported me throughout my life. I would especially like to thank my friends Ryan, Michael, Tommy, Shaun, and Jeff who have allowed me to bounce ideas and get technical feedback during my research. I would also like to thank my colleagues in Stuttgart Germany, especially

Dr. Stefan Krojer, all the exchange students, Dr. Markus Feucht, and Dr. Filipe Andrade for their friendship and technical inspiration leading up to this dissertation.

Lastly, I would like to acknowledge my family: Veronica, Russell, Caitlin, Connor, Donna, Shelly, and especially my father Rusty. You have all inspired me and shaped my life into what it is now. Without your support, I would never be able to accomplish this and I am forever thankful.

TABLE OF CONTENTS

	Page
List of Tables	viii
List of Figures	ix
List of Equations	xi
List of Abbreviations and Symbols.....	xiii
Abstract	xiv
Chapter 1 - Introduction.....	1
1.1 Background and Motivation.....	1
1.2 Research Objectives	6
Chapter 2 - Literature Review.....	10
2.1 – Introduction to Yielding	10
2.1.1 – Isotropic Yield Criteria for Metals	11
2.1.2 – Anisotropic Yield Criteria for Metals.....	14
2.2 – Notable Existing Material Models	15
Chapter 3 - Methodology	28
3.1 – Material Law	28
3.1.1 – Yield Surface	28
3.1.2 – Flow Rule	39
3.1.3 – Convexity.....	42
3.2 – Implementation into the LS-DYNA Code	48
3.2.1 – Source Code Overview	54
3.2.2 – Single Element Verification	69
3.3 – Visualization of the Yield Surface	89
Chapter 4 - Material Model Validation.....	96
4.1 – Al-2024 Material Validation	96
4.1.1 – Al-2024 Material Testing Program.....	96
4.1.2 – Al-2024 Material Model Parameters	98

4.1.3 – Al-2024 Material Model Validation Program	108
4.2 – Ti-6Al-4V Material Validation	110
4.2.1 – Ti-6Al-4V Material Testing Program.....	110
4.2.2 – Ti-6Al-4V Material Model Parameters	114
4.2.3 – Ti-6Al-4V Material Model Validation Program	126
4.2.4 – Ti-6Al-4V Ballistic Impact Simulations.....	129
Chapter 5 - Summary, Conclusions, and Recommendations for Future Research.....	144
Appendix.....	149
References.....	155

LIST OF TABLES

Table	Page
Table 1: Notable Existing Material Models [11]	16
Table 2: Coefficients of the orthotropic Lode parameters	38
Table 3: Material model input descriptions	50
Table 4: Single element strain rate yield curve scale factors.....	78
Table 5: Single element temperature yield curve scale factors.....	82
Table 6: Computational cost as a function of number of iterations	88
Table 7: History variables used to visualize yield surface.....	90
Table 8: Composition of 12.7mm thick 2024-T351 aluminum plate [14].....	96
Table 9: Material model properties for Al-2024.....	99
Table 10: Al-2024 material axis options for each specimen direction in tension.....	109
Table 11: Composition of 6.35mm thick Ti-6Al-4V plate [15].....	111
Table 12: Material model properties for Ti-6Al-4V	115
Table 13: Ti-6Al-4V material axis options for each specimen direction in tension.....	127
Table 14: Ti-6Al-4V material axis options for each specimen direction in compression	127
Table 15: Strain rate input yield curve scale factors.....	131
Table 16: Temperature input yield curve scale factors	131

LIST OF FIGURES

Figure	Page
Figure 1: Diagram of aluminum components used in the 2015 Ford F-150 [4]	2
Figure 2: Photographs of aluminum components used in the 2015 Ford F-150.....	2
Figure 3: Examples of an uncontained engine failure [8] [9]	4
Figure 4: Tensile test results from multiple titanium alloy plates in different orientations to show anisotropy [15]	6
Figure 5: Elastic and plastic deformation in uniaxial tension test	10
Figure 6: Tresca and von Mises yield criteria.....	13
Figure 7: Graphical representation of Hill convexity condition #7	47
Figure 8: Convexity enforcement algorithm.....	48
Figure 9: Material input keyword format.....	49
Figure 10: Material model routine flow chart.....	55
Figure 11: Isotropic single element verification	70
Figure 12: Isotropic Generalized Yield Surface input	71
Figure 13: Isotropic implementation of the anisotropic material model.....	71
Figure 14: Isotropic single element verification simulation longitudinal stress	72
Figure 15: Isotropic single element verification simulation results.....	72
Figure 16: Anisotropic material model input.....	73
Figure 17: Anisotropic single element verification	74
Figure 18: Anisotropic single element verification simulation longitudinal stress	75
Figure 19: Anisotropic single element simulation results.....	76
Figure 20: Anisotropic and strain rate dependent material model input.....	77
Figure 21: Single element input velocities for strain rate verification.....	79
Figure 22: Single element verification for strain rate results.....	80
Figure 23: Single element strain rate verification.....	81
Figure 24: Anisotropic and temperature dependent material model input	82
Figure 25: Single element verification for thermal results	84
Figure 26: Single element simulation results with varying number of iterations	86
Figure 27: Single element simulation results with varying convergence tolerance.....	87
Figure 28: Visualization of Anisotropic symmetric yield surface	94
Figure 29: Visualization of Anisotropic and directional asymmetric yield surface	95
Figure 30: Al-2024 uniaxial tension specimen specifications	97
Figure 31: Al-2024 uniaxial tension test data	98
Figure 32: Al-2024 true stress vs. true strain.....	100
Figure 33: Al-2024 yield point	101
Figure 34: Al-2024 true stress vs. plastic strain.....	102

Figure 35: Al-2024 determination of the necking point for the 0-degree specimen.....	104
Figure 36: Al-2024 extrapolated yield curves for 0-degree specimen.....	106
Figure 37: Al-2024 uniaxial tension specimen finite element mesh.....	107
Figure 38: Al-2024 simulation results with Tabulated Johnson-Cook material model ..	107
Figure 39: Al-2024 selected yield curves	108
Figure 40: Material input card for Al-2024 (0-degree).....	109
Figure 41: Al-2024 simulation results with anisotropic material model	110
Figure 42: Ti-6Al-4V uniaxial tension specimen specifications	112
Figure 43: Ti-6Al-4V compression specimen specifications.....	112
Figure 44: Ti-6Al-4V uniaxial tension test data	113
Figure 45: Ti-6Al-4V uniaxial compression test data.....	114
Figure 46: Ti-6Al-4V true stress vs. true strain	116
Figure 47: Ti-6Al-4V yield point.....	117
Figure 48: Ti-6Al-4V true stress vs. plastic strain.....	118
Figure 49: Ti-6Al-4V determination of the necking point for the 0-degree specimen ...	120
Figure 50: Ti-6Al-4V extrapolated yield curves for 0-degree specimen	122
Figure 51: Ti-6Al-4V uniaxial tension specimen finite element mesh.....	123
Figure 52: Ti-6Al-4V tension simulation results with Tabulated Johnson-Cook material model.....	123
Figure 53: Ti-6Al-4V selected tension yield curves	124
Figure 54: Ti-6Al-4V selected compression yield curves	125
Figure 55: Ti-6Al-4V compression simulation results with Tabulated Johnson-Cook material model	125
Figure 56: Material input card for Ti-6Al-4V (0-degree material axis options).....	127
Figure 57: Ti-6Al-4V tension simulation results with anisotropic material model	128
Figure 58: Ti-6Al-4V compression simulation results with anisotropic material model	128
Figure 59: Ti-6Al-4V ballistic impact test set up [16].....	129
Figure 60: Anisotropic material input card for Ti-6Al-4V ballistic simulation.....	133
Figure 61: Isotropic material input card to Ti-6Al-4V ballistic simulation.....	134
Figure 62: Ballistic projectile mesh	135
Figure 63: Comparison of isotropic models (internal energy) – 229 m/s initial velocity	136
Figure 64: Comparison of isotropic models (internal energy) – 278 m/s initial velocity	136
Figure 65: Comparison of isotropic models (projectile velocity)	137
Figure 66: Comparison of isotropic models (plastic strain).....	138
Figure 67: Comparison of isotropic and anisotropic models (internal energy) – 229 m/s initial velocity	139
Figure 68: Comparison of isotropic and anisotropic models (internal energy) – 278 m/s initial velocity	139
Figure 69: Comparison of isotropic and anisotropic models (projectile velocity)	140
Figure 70: Comparison of isotropic and anisotropic models (plastic strain)	141
Figure 71: von Mises stress distribution with isotropic material model - 229 m/s.....	142
Figure 72: von Mises stress distribution with anisotropic material model - 229 m/s	142

LIST OF EQUATIONS

Equation	Page
Equation 1: Basic yield function formulation.....	12
Equation 2: Deviatoric part of stress tensor.....	12
Equation 3: Stress tensor.....	12
Equation 4: Three stress invariants.....	12
Equation 5: Yield function with invariants.....	13
Equation 6: Tresca yield function.....	13
Equation 7: von Mises yield function.....	13
Equation 8: Hill 1948 yield criterion [21].....	15
Equation 9: Tabulated Johnson-Cook material model yield formulation.....	29
Equation 10: Tabulated Johnson-Cook material model thermal formulation.....	29
Equation 11: Lode Parameter as used in the Generalized Yield Surface Model.....	29
Equation 12: Generalized Yield Surface material model yield function formulation.....	30
Equation 13: Generalized Yield Surface computation of c coefficients.....	30
Equation 14: Definition of material directions.....	31
Equation 15: Orthotropic third deviatoric invariant.....	32
Equation 16: Orthotropic Lode Parameter under hydrostatic loading.....	32
Equation 17: Isochoric condition of third deviatoric invariant.....	32
Equation 18: Orthotropic Lode Parameter.....	32
Equation 19: Uniaxial state of stress in 0-degree direction.....	33
Equation 20: Uniaxial state of stress in 90-degree direction.....	33
Equation 21: Uniaxial state of stress in 45-degree direction.....	33
Equation 22: Uniaxial state of stress in thickness direction.....	33
Equation 23: Orthotropic Lode Parameter for uniaxial state of stress (0-degree).....	33
Equation 24: Orthotropic Lode Parameter for uniaxial state of stress (90-degree).....	33
Equation 25: Orthotropic Lode Parameter for uniaxial state of stress (thickness).....	34
Equation 26: Orthotropic Lode Parameter for uniaxial state of stress (45-degree).....	34
Equation 27: Hill yield function.....	34
Equation 28: Hill yield function for uniaxial state of stress (0-degree).....	34
Equation 29: Hill yield function for uniaxial state of stress (90-degree).....	35
Equation 30: Hill yield function for uniaxial state of stress (thickness).....	35
Equation 31: Hill yield function for uniaxial state of stress (45-degree).....	35
Equation 32: Orthotropic generalization of GYS material model.....	35
Equation 33: Determination of the 0-degree orthotropic coefficients.....	36
Equation 34: Determination of the 90-degree orthotropic coefficients.....	36
Equation 35: Determination of the 45-degree orthotropic coefficients.....	36

Equation 36: Determination of the thickness orthotropic coefficients	37
Equation 37: First condition for beta coefficient	38
Equation 38: Second condition for beta coefficient.....	39
Equation 39: Associated flow rule.....	40
Equation 40: Derivatives of the Hill yield function.....	40
Equation 41: Derivatives of the third orthotropic invariant.....	41
Equation 42: Effective stress	42
Equation 43: Derivative of the effective stress	42
Equation 44: Convexity conditions for Hill yield function	43
Equation 45: Convexity conditions for model implementation of Hill yield function	44
Equation 46: Simplification of Hill convexity condition #4.....	45
Equation 47: Simplification of Hill convexity condition #7.....	46
Equation 48: Yield surface visualization equation for 00-90 plane.....	91
Equation 49: Yield surface visualization equation for 00-45Shear plane.....	91
Equation 50: Yield surface visualization equation for 00-Thickness plane	92
Equation 51: True stress calculation	99
Equation 52: True strain calculation	99
Equation 53: Plastic strain calculation	101
Equation 54: State of stress before necking.....	103
Equation 55: State of stress after diffuse necking.....	103
Equation 56: State of stress after local necking	103
Equation 57: Yield curve extrapolation equation	104
Equation 58: Yield curve continuous extrapolation.....	104
Equation 59: Yield curve smooth extrapolation	105
Equation 60: Yield curve extrapolation equation for parameter k.....	105
Equation 61: Yield curve extrapolation equation for parameter e.....	105
Equation 62: True stress calculation	115
Equation 63: True strain calculation	116
Equation 64: Plastic strain calculation.....	117
Equation 65: State of stress before necking.....	119
Equation 66: State of stress after diffuse necking.....	119
Equation 67: State of stress after local necking	119
Equation 68: Yield curve extrapolation equation	120
Equation 69: Yield curve continuous extrapolation.....	120
Equation 70: Yield curve smooth extrapolation	121
Equation 71: Yield curve extrapolation equation for parameter k.....	121
Equation 72: Yield curve extrapolation equation for parameter e.....	121
Equation 73: Tension in thickness direction	126

LIST OF ABBREVIATIONS AND SYMBOLS

GYS: Generalized Yield Surface
MPP: Massively Parallel Processing
NASA: The National Aeronautics and Space Administration
FAA: Federal Aviation Administration
LSTC: Livermore Software Technology Corp.
AOPT: Material axis option
 F : Force
 ε : Strain
 σ : Stress
 σ_y : Yield stress
 ε_y : Yield strain
 I_1, I_2, I_3 : Stress invariants
 \mathbf{S} : Deviatoric stress tensor
 f : Yield function
 F, G, H, L, M, N : Hill yield function parameters
 σ_{vm} : von Mises stress
 ε_p : Equivalent plastic strain
 $\dot{\varepsilon}_p$: Equivalent plastic strain rate
 T : Temperature
 T_r : Room temperature
 β : Fraction of plastic work converted into heat
 C_p : Specific heat
 ρ : Density
 θ_L : Lode parameter
 c_1, c_2, c_3 : Yield function parameters
 σ_s : Shear stress
 $\vec{a}, \vec{c}, \vec{d}, \vec{e}_x, \vec{e}_y, \vec{e}_z$: Directional unit vectors
 b, d : Independent yield function parameters
 α, β : First and second orthotropic Lode parameter coefficients
 λ : Plastic multiplier
 σ : Effective stress
 $\sigma_{true}, \sigma_{eng}$: True and engineering stress
 $\varepsilon_{true}, \varepsilon_{eng}$: True and engineering strain
 E : Modulus of elasticity
K: Kelvin

ABSTRACT

AN ANISOTROPIC AND ASYMMETRIC MATERIAL MODEL FOR SIMULATION OF METALS UNDER DYNAMIC LOADING

Sean Harrison Haight, Ph.D.

George Mason University, 2016

Dissertation Director: Dr. Cing-Dao “Steve” Kan

The purpose of this research is to develop a fully-tabulated, anisotropic, asymmetric, strain rate, and temperature dependent material model for solid finite elements. Physical testing of several metallic materials has shown to have anisotropic (or orthotropic) characteristics. While many material models in finite element codes currently have anisotropic options, they tend to focus on material forming applications – not crash and impact analysis. Unlike most anisotropic forming material models, this model has: rate dependency, temperature dependency, tabulated hardening (as opposed to parameterized inputs), associated flow, and the ability to maintain numerical stability for large deformations.

The implementation of this anisotropic model is an extension of the currently existing Generalized Yield Surface (GYS) variant of the Tabulated Johnson-Cook material model. This new model builds upon the previously available features of both of these well-established material models. Strain rate and temperature dependencies are

utilized as independent tabulated values. Yield curves for tension, compression and shear are also tabulated and independent. Isotropic failure is retained from the Tabulated Johnson-Cook model as a function of triaxiality, Lode parameter, strain rate, temperature and element size. Lastly, tabulated plasticity for tension and compression allows the user to specify yield stress in the 0-degree, 45-degree, 90-degree, and thickness directions (as a function of strain rate). Therefore, this model applies to thick orthotropic metallic plates as it is assumed that a thickness direction can be recognized in the structure (although no plane state of stress is assumed) and that the response under 135-degree and 45-degree are identical. Due to the fully tabulated nature of the material law, rate and temperature dependency and asymmetry are all orthotropic in nature which is a unique feature of this current approach.

Physical testing (tension and compression) of Al-2024 and Ti-6Al-4V specimens were used to validate the development of this material model. Using a single material model for each metal, the author was able to replicate test results in each specimen direction. Lastly, this model was used to simulate ballistic impacts of a 0.25 inch Ti-6Al-4V plate and compared to other models with comparable inputs.

CHAPTER 1 - INTRODUCTION

1.1 Background and Motivation

Developing computational material models that can accurately describe the plastic deformation of metals has long been the focus of research for engineers and scientists alike [1]. These developments have been directly applied to multiple types of complex engineering problems through finite element codes. Over the years, simple plasticity models have been redeveloped into models that can accurately predict plastic deformation when a material is subjected to complex loading conditions. For example, more modern plasticity models can handle materials that are subjected to multi-axial states of stress, variable temperature conditions, and high strain rates. Additionally, complex failure models have been developed to predict dynamic material failure.

One common example of the application of advanced material models in finite element simulations is in the automotive industry. While steel components are often used in vehicle structures, many vehicle manufacturers are using lighter materials such as aluminum and magnesium [2]. Specifically, many of these lighter materials are being implemented in vehicle structures or energy absorbing components used in crashworthiness applications [3]. One example of this can be seen in the 2015 Ford F-150 (Figure 1 and Figure 2)

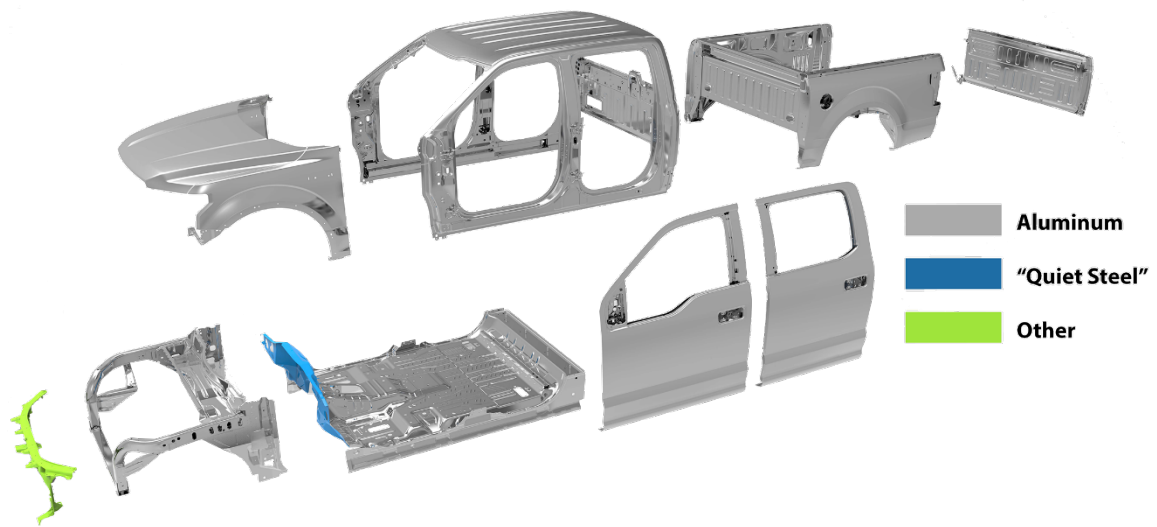


Figure 1: Diagram of aluminum components used in the 2015 Ford F-150 [4]



Figure 2: Photographs of aluminum components used in the 2015 Ford F-150

Traditionally, isotropic material models have been used in crashworthiness simulations where steel components are used. However, now that aluminum and magnesium materials are being implemented more frequently, anisotropic material

models are being considered in crashworthiness simulations [5]. This is the case particularly for extruded parts that have a very pronounced anisotropic flow. Since the use of these materials are only now being implemented in these structural components, there is limited support of anisotropic material model development for use in dynamic impact analysis. Most of the existing anisotropic material models in most finite element codes are primarily focused on manufacturing and forming applications that have limited capabilities for impact simulations.

When performing automobile crashworthiness design and analysis, it can be very important that the material failure is predictive. There have been many advancements in isotropic failure and damage models [6] that can very accurately predict failure based on the state of stress and failure strain. However, when used on a component level, these methods rely heavily on a true representation of the plastic strain. Therefore, if the plastic strain of the material is not accurate in the simulation, the failure prediction will likely not be reliable. This is especially true for materials such as aluminum where the manufacturing process, for both rolled sheets and extrusions, can result in anisotropy.

In addition to automotive applications, the aerospace industry utilizes computational material models to simulate critical safety applications. One such application is the containment of airplane turbine blade failure (as seen in Figure 3) [7]. These simulations are performed to ensure the structural integrity of the engine assembly during flight as well as to ensure satisfactory blade-out certification testing.

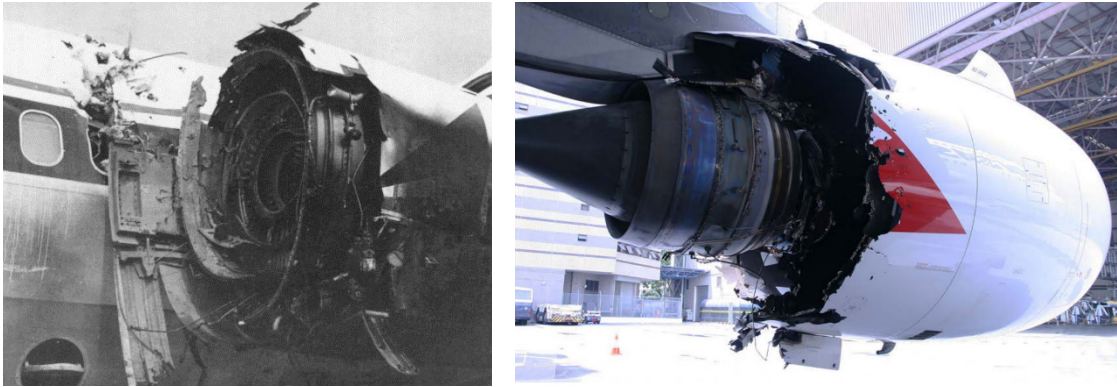


Figure 3: Examples of an uncontained engine failure [8] [9]

In aerospace applications, it is traditional to use lighter materials such as aluminum and titanium alloys in many structural components. One such application is the housing of the turbine engine. It is crucial that this housing be able to contain any projectiles in the rare instance where a turbine blade may fail. Therefore, engine blade-out and containment simulations must be able to accurately predict the result of this impact. These simulations heavily rely on sophisticated plasticity and failure models and can be very sensitive to the characterization of the materials.

Traditionally, the research efforts were focused on applying the Johnson-Cook plasticity model (1983) to simulate the plastic deformation in these simulations [10]. This is due to the model's ability to handle strain rate and temperature sensitive plasticity [11]. More recently, a tabulated version of the Johnson-Cook material model was developed which allows for test data to be directly used in the characterization of the material [12].

Additionally, a modified Tabulated Johnson-Cook material model, known as the Tabulated Johnson-Cook Generalized Yield Surface (GYS) material model, was

developed which is capable to handle tension/compression asymmetry (typically seen in HCP metals like titanium) [13].

While these newly developed models are very valuable for predicting the deformation and failure of ballistic impacts, they are designed for isotropic materials. It has been shown, through physical testing, that many of the materials used in aerospace components do exhibit anisotropic characteristics (Figure 4) [14] [15]. Therefore, it would actually be more appropriate to model these materials with anisotropic plasticity models.

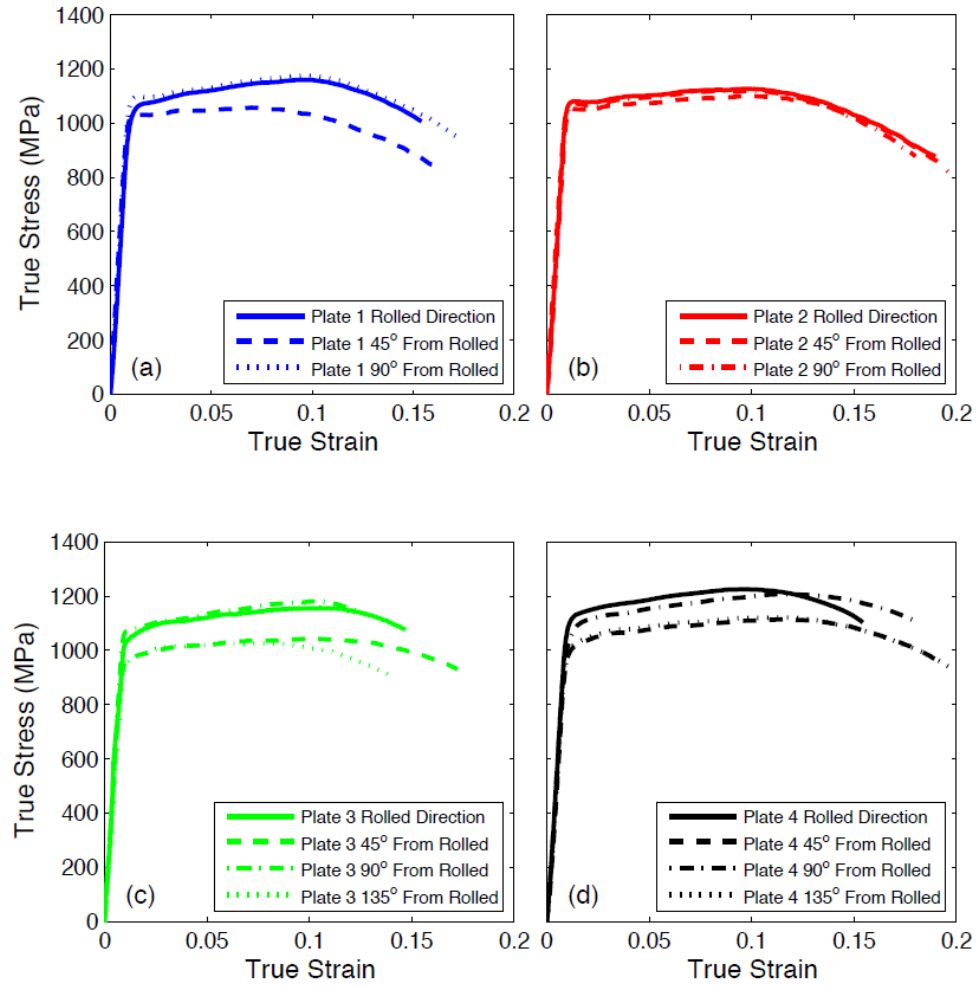


Figure 4: Tensile test results from multiple titanium alloy plates in different orientations to show anisotropy [15]

1.2 Research Objectives

The objective of this research is to develop a new anisotropic computational material model for use in crash and impact applications. Since many of the materials now used in the automotive and aerospace industries can become highly anisotropic during the manufacturing process, this model would be able to assist engineers and researchers better characterize material models for analysis.

This model should be based upon the Tabulated Johnson-Cook Generalized Yield Surface (GYS) material model formulation. This model allows for the simulation of strain rate and temperature sensitive materials and includes a sophisticated failure and damage model based on the state of stress, plastic strain, strain rate, temperature and element size. Additionally, this model includes the ability to simulate materials that exhibit tension/compression asymmetry, in that the yield stress is different in tension and compression. Lastly, this model relies on tabulated inputs for all parameters that allows the analyst to input material testing data into the material model for a more accurate response. This generalized model is the ideal candidate to build an anisotropic model upon.

In addition to all of the features that currently exist in the GYS model, this model should have tabulated inputs that correspond to the flow stress in multiple material directions. The goal of this research is to be able to provide inputs for the flow stress in the 0-degree direction, 45-degree direction, 90-degree direction, and through the thickness direction of the material in both tension and compression. These inputs can be established through a series of anisotropic uniaxial tension and compression tests. Since hardening curves are provided in tension and compression for all four directions, the resulting model exhibits a directional asymmetry.

Similar to the tabulated Johnson-Cook and GYS models, this model should have the ability to simulate the material response at multiple strain rates. This strain rate effect should be input into the material model as a tabulated input and should be directional. This means that there should be tabulated strain rate data for each of the four different

material directions (0-deg, 45-deg, 90-deg, and thickness). Additionally, this strain rate effect should be applied to both tension and compression states of stress.

In addition to strain rate dependency, this material model should be able to model any thermal effects for a given material. Similar to the strain rate input, this model should have the option for tabulated inputs based on the temperature of the material. This thermal effect should also be directional, in that each material direction should have a tabulated input as a function of temperature. Lastly, the fraction of plastic work converted into heat parameter should be available as an independent variable.

Convexity of the yield surface should be enforced within the material subroutine when possible. This means that there should be some numerical method for ensuring that the yield surface is convex at all points. If a mathematical method is not established for a specific combination of model features, then the ability for the user to inspect or visualize the yield surface should be available.

This model should be ready for implementation into a commercial finite element code, such as LS-DYNA. Ideally, this model will be written in the language and format of this commercial code so that the implementation is seamless.

Furthermore, the routine should be able to successfully compile and execute on a massively parallel processing (MPP) system without runtime errors. Lastly, this model should be robust enough to complete complex simulations with over one million element models.

Single element simulations should be completed to ensure that the material routine works as intended. These single element simulations should show that the

resulting flow stress is equivalent to the tabulated inputs. This should be true for each material direction in both tension and compression. These single element simulations should also test the material routine's ability to model varying strain rate and temperature conditions.

Material characterizations should be developed for Al-2024 and Ti-6Al-4V materials to test with this material model. Tabulated yield curves for each material should be developed and used as inputs in the routine. Additionally, tension and compression specimens should be modeled to match any available test data.

Lastly, titanium ballistic impact tests on titanium plates [16] should be simulated using this material model. The results of these simulations are then compared to other models with comparable input parameters.

The most significant contributions of this work to the engineering and scientific field are the development and verification of:

- A tabulated model with directional asymmetry.
- An anisotropic model with tabulated rate effects.
- An anisotropic model with tabulated thermal softening.
- A new material model that is able to simulate large (1M+ element) finite element models.
- An (industrial) anisotropic model characterization for two material plates (Al-2024 and Ti-64).

CHAPTER 2 - LITERATURE REVIEW

2.1 – Introduction to Yielding

When materials, like metals, are loaded such that there is permanent deformation, plastic strains exist even when the loading is reduced or removed. The analysis of this plastic deformation is very important in engineering applications such as impact analysis, crashworthiness, metal forming and others. The moment that a material under loading begins to exhibit plastic deformation is called the yield stress. Before this level of stress, the deformation is considered to be elastic. Figure 5 shows an example of elastic and plastic deformation.

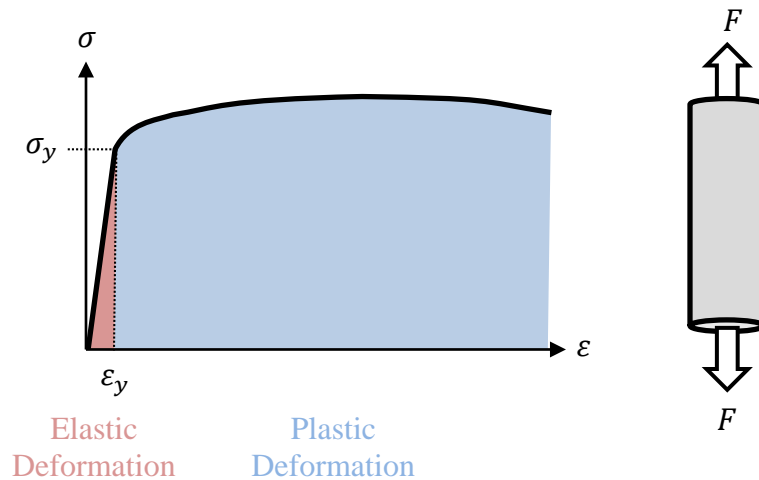


Figure 5: Elastic and plastic deformation in uniaxial tension test

In classic mechanics theory, it is defined that after a material is deformed, past the yield point, and then unloaded, that material does not reassume its original shape and

size. Rather, it retains the plastic deformation while the elastic deformation is reversible. When a material like metal is in the plastic region of deformation, it is typical for the flow stress to increase monotonically as plastic strain is accumulated. When a material is loaded in a multi-axial state of stress, the material's yield point is defined by a mathematical function or *yield surface*. This yield surface defines the locus of all states of stress for which yielding occurs in any given stress space. For a given material under loading, a state of stress inside of the yield surface is considered to be elastic while a state of stress on the surface is considered plastic. States of stress outside of the yield surface is assumed to be not permissible.

2.1.1 – Isotropic Yield Criteria for Metals

There are typically two different approaches when attempting to describe metallic plasticity: the polycrystal and phenomenological approaches [17]. The polycrystal approach adopts the idea that each grain in the material undergoes homogeneous deformation. Additionally, each grain is assumed to be rigid-plastic, or the elastic deformation of the grain is not considered. Therefore, the material properties are determined for each grain and then averaged for the entire polycrystal. While this is sometimes the most appropriate method for forming applications, the polycrystal formulation has some drawbacks. It is very difficult to determine the directions of the individual grains, which usually requires an expensive experimental program. It is also computationally very expensive and requires significant resources when implemented in a finite element code.

By using the phenomenological approach, a yield function (f) is derived to describe the behavior of the material, usually as a function of the deviatoric part of the stress (\mathbf{S}).

Equation 1: Basic yield function formulation

$$f(\mathbf{S}) = 0$$

Equation 2: Deviatoric part of stress tensor

$$\mathbf{S} = \boldsymbol{\sigma} - \frac{1}{3}(\text{tr}\boldsymbol{\sigma})$$

Equation 3: Stress tensor

$$\boldsymbol{\sigma} = \begin{bmatrix} \sigma_{xx} & \sigma_{xy} & \sigma_{xz} \\ \sigma_{xy} & \sigma_{yy} & \sigma_{yz} \\ \sigma_{xz} & \sigma_{yz} & \sigma_{zz} \end{bmatrix}$$

Under isothermal conditions, the yield surface is a function of the state of stress of the material and is, in the isotropic case, commonly described by three stress and/or deviatoric stress invariants [13]:

Equation 4: Three stress invariants

$$\begin{aligned} I_1 &= \sigma_{ii} \\ J_2 &= \frac{1}{2} \mathbf{S}_{ij} \mathbf{S}_{ij} \\ J_3 &= \frac{1}{2} \mathbf{S}_{ij} \mathbf{S}_{jk} \mathbf{S}_{ki} \end{aligned}$$

The first invariant represents the hydrostatic stress while the second invariant is often referred to as the distortional energy in the material. The third invariant is a parameter that can be used to distinguish the yield and flow behavior between tension and compression. Using these three stress invariants, the yield function can be described as:

Equation 5: Yield function with invariants

$$f(\sigma_{ij}) = f(I_1, I_2, I_3) = k^2$$

Some of the most well-known and traditional yield functions are the Tresca [18] and von Mises [19] yield functions (Figure 6).

Equation 6: Tresca yield function

$$\sigma_y = \max\{|\sigma_1 - \sigma_2|, |\sigma_2 - \sigma_3|, |\sigma_3 - \sigma_1|\}$$

Equation 7: von Mises yield function

$$\sigma_y = \frac{1}{\sqrt{2}} \sqrt{(\sigma_1 - \sigma_2)^2 + (\sigma_2 - \sigma_3)^2 + (\sigma_3 - \sigma_1)^2} = \sqrt{3J_2}$$

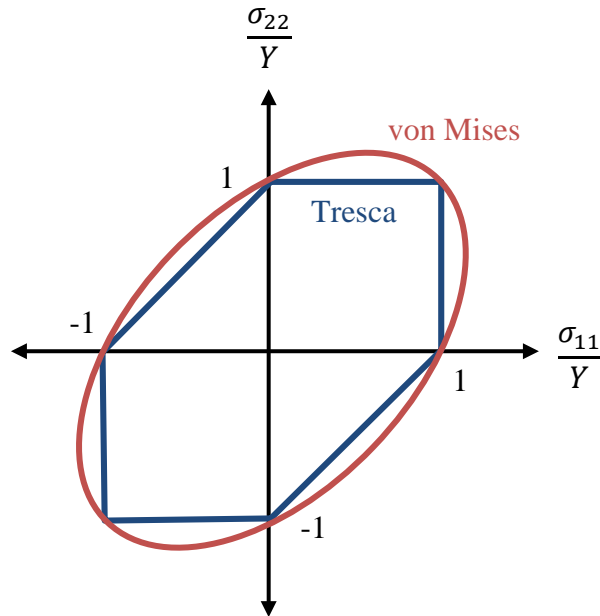


Figure 6: Tresca and von Mises yield criteria

The Tresca criterion (Equation 6) is based on the assumption that the yielding depends on the maximum shear stress. According to this formulation, the material becomes plastic when the maximum shear stress reaches a specific critical value. This criteria is a function of the principal stresses and the yield stress is in uniaxial tension. The von Mises yield criterion is based on the assumption that the hydrostatic pressure should not cause yielding of the material and that the plastic state depends on a critical value of the energy distortion, or second invariant (Equation 7). In both cases the yield stress can be measured directly in uniaxial tension.

2.1.2 – Anisotropic Yield Criteria for Metals

While the von Mises and Tresca yield criteria are commonly used for modeling isotropic metals, other yield criteria have been developed for anisotropic metals [20]. Some of these include Hill (1948) [21], Hill (1979) [22], Hershey (1954) [23], Hosford (1972) [24], Bassani (1977) [25], Gotoh (1977) [26], Logan and Hosford (1980) [27], Jones and Gillis (1984) [28], Budianski (1984) [29], Barlat (1989) [20] and Barlat (2003) [30]. Due to its simplicity, the Hill (1948) criterion has been most commonly used for modeling of anisotropic metals. This is due to Hill's ability to describe the full plastic behavior of orthotropic metals in numerical simulations [20].

A well-known work by Hill in 1948 was to “formulate a theory capable of describing the macroscopic behavior of anisotropic metals” [21]. Hill assumes that the anisotropy has three mutually orthogonal planes of symmetry at each point. These three planes meet in three orthogonal directions which are called the principal axes of

anisotropy. For example, for a rolled or extruded sheet, the three principal axes would likely be oriented in the direction of rolling/extruding, the transverse direction and normal to that plane. Hill went on to develop a yield criteria of the form:

Equation 8: Hill 1948 yield criterion [21]

$$2f \equiv F(\sigma_{yy} - \sigma_{zz})^2 + G(\sigma_{zz} - \sigma_{xx})^2 + H(\sigma_{xx} - \sigma_{yy})^2 + 2L\sigma_{yz}^2 + 2M\sigma_{zx}^2 + 2N\sigma_{xy}^2 = 1$$

Where F, G, H, L, M, N are constants based on the current state of anisotropy. This formulation of the yield function is valid when the principal axes of anisotropy are chosen as the reference axes. For other reference axes, it can be rewritten by transforming the stress components.

2.2 – Notable Existing Material Models

Over the years, many material models have been developed and implemented in commercially available finite element codes. In the following section, some of the most notable and frequently used models that are directly relevant to this research are briefly described. It is noted that the code chosen in this research is the LS-DYNA, developed by the Livermore Software Technology Corporation (LSTC). The numeric designation of the models in Table 1 can be found in the LS-DYNA User Manual [11].

Table 1: Notable Existing Material Models [11]

Material Model Number and Description		Strain Rate	Failure	Thermal	Anisotropic	Damage	Asymmetric
033	Barlat Anisotropic Plasticity (YLD96)	Y			Y		
036	Three-Parameter Barlat Plasticity	Y		Y	Y		
133	Barlat YLD2000	Y		Y	Y		
135	Weak and Strong Textured Model	Y	Y		Y		
224	Tabulated Johnson-Cook	Y	Y	Y		Y	
224G	Tabulated Johnson-Cook Generalized Yield Surface (GYS)	Y	Y	Y		Y	Y
243	Hill 90	Y		Y	Y		

The Tabulated Johnson-Cook material model was developed by Buyuk [1]. This is a thermo-viscoplastic material model with tabular inputs. Mesh regularized failure was also built into this material routine in order to predict failure of structures in impact loading simulations. Additionally, this material model included the ability to account for varying strain rates and temperatures during a given simulation. The Tabulated Johnson-Cook material model is based on an isotropic, isochoric, von Mises type plasticity where strain rate hardening and temperature softening is considered [1]. By way of utilizing plastic work, this model accounts for adiabatic heating and softening. In addition to the constitutive relationship, this material model also includes a robust failure law. The failure locus is based on the state of stress, strain rate and temperature. Lastly, this failure locus can be adapted for varying mesh sizes with a scaling factor. While this material model does include many important features, it does lack the ability to accurately model

materials that have different yield stress in tension, compression and shear. Lastly, this model does not allow for modeling anisotropic materials.

The following are typical material inputs used for the Tabulated Johnson-Cook model [11]:

- Mass density
- Young's modulus (constant or temperature dependent given by a load curve)
- Poisson's Ratio
- Specific heat
- Room temperature
- Fraction of plastic work converted into heat (constant or strain rate dependent given by a load curve)
- Number of integration points which must fail before an element is deleted (or percentage of integration points)
- Table defining the effective stress as a function of the effective plastic strain (yield curve) for each plastic strain rate (isothermal)
- Table defining the quasi-static effective stress as a function of the effective plastic strain for a given temperature
- Table defining the plastic failure strain as a function of triaxiality and Lode parameter
- Load curve defining the plastic failure strain as a function of plastic strain rate

- Load curve defining the plastic failure strain as a function of temperature
- Load curve (or table) defining the plastic failure strain as a function of element side (for each triaxiality)

The Generalized Yield Surface (GYS) variation of the Tabulated Johnson-Cook material model was developed by Sengoz [13]. This material model, which is based on the foundation set by the Tabulated Johnson-Cook material model, allows for the simulation of materials that reflect an asymmetry between the yield stresses in tension, compression and shear. While traditional von Mises type yield criteria cannot simulate these asymmetric materials, this model provides a more generalized isotropic and distortional yield surface that can represent such materials. Similar to the original Tabulated Johnson-Cook material model, the Generalized Yield Surface model also allows for rate and temperature dependencies and includes a failure model that is a function of triaxiality and Lode parameter. This model is an improvement over the original Tabulated Johnson-Cook material model, however it still lacks the ability to simulate anisotropic materials.

The following are typical inputs used for the Tabulated Johnson-Cook Generalized Yield Surface material model [11]:

- Mass density
- Young's modulus (constant or temperature dependent given by a load curve)
- Poisson's Ratio
- Specific heat

- Room temperature
- Fraction of plastic work converted into heat (constant or strain rate dependent given by a load curve)
- Number of integration points which must fail before an element is deleted (or percentage of integration points)
- Table defining the effective stress as a function of the effective plastic strain (yield curve) for each plastic strain rate (isothermal)
- Table defining the quasi-static effective stress as a function of the effective plastic strain for a given temperature
- Table defining the plastic failure strain as a function of triaxiality and Lode parameter
- Load curve defining the plastic failure strain as a function of plastic strain rate
- Load curve defining the plastic failure strain as a function of temperature
- Load curve (or table) defining the plastic failure strain as a function of element size (for each triaxiality)
- Table defining the compressive yield stress as a function of plastic strain for each plastic strain rate
- Table defining the quasi-static compressive yield stress as a function of strain for a given temperature
- Table defining the shear yield stress as a function of the plastic strain for each plastic strain rate

- Table defining the quasi-static shear yield stress as a function of strain for a given temperature
- Scale factor on the initial estimate of the plastic multiplier
- Number of secant iterations to be internally performed

The Barlat Anisotropic Plasticity model was developed in 1997 and primarily used in metal forming applications [31]. At that time, optimization, material selection and manufacturing methods were becoming very important in aerospace, automotive and packaging applications. Instead of applying traditional steel material models to materials such as aluminum alloy sheets, the developers designed a new model that could accurately simulate anisotropic materials. In the implementation to many of the finite element codes, this material model is only available for shell elements. This material does not allow for asymmetric inputs, thermal dependency, or a dedicated failure model.

The following are typical inputs used for the Barlat Anisotropic Plasticity (YLD96) material model [11]:

- Mass density
- Young's modulus
- Poisson's ratio
- Strength coefficient or a coefficient in Voce equation
- Strain corresponding to the initial yield or b in Voce equation
- Hardening exponent for yield strength or c in Voce equation
- Power-law rate sensitivity
- Exponent for strain rate effects

- Hardening option (load curve, power-law, or Voce equation)
- Flow potential exponent
- Components of the deviatoric stress tension
- Principal axis coefficients
- Material axis options

The Three-Parameter Barlat Plasticity model is based on research conducted by Barlat and Lian in 1989 [20]. Like the Barlat Anisotropic Plasticity model, this model was designed to more accurately simulate the forming process for sheet metals. Therefore, this model was designed and only applies to shell elements in plane stress applications. However, this material model does allow for the use of the Lankford parameters, or the R-value, as an input variable to define the anisotropy [11]. This model also allows for a constant Young's modulus or one that is defined as a function of plastic strain.

In this material model, there are many options when defining the hardening rule including: linear, exponential (Swift), tabulated curve, tabulated table with strain rate effects, exponential (Voce, Gosh, or Hockett-Sherby), tabulated curves in each of three material directions, table with temperature dependence or a three dimension (3-D) table with temperature and strain rate dependence. Depending on the hardening rule, different material parameters can be defined. In addition to the hardening rule, the Lankford parameters in the 0-degree, 45-degree, and 90-degree directions can be defined as a constant value or tabulated as a function of plastic strain and temperature.

The ability to vary the Lankford parameters was initially reported in 2007 by Fleischer, Borrvall, and Bletzinger [32]. Instead of using constant values for hardening and Lankford parameters, the authors used tabulated inputs. It was concluded that in order to get a more realistic mathematical description of the actual material behavior, the material model should have: variable Lankford parameters, variable Young's modulus, variable volume and three independent yield curves for the 0-degree, 45-degree, and 90-degree material directions (relative to the rolling direction).

The following are typical inputs used for the Three-parameter Barlat Plasticity material model [11]:

- Mass density
- Young's modulus (constant or load curve as a function of plastic strain)
- Poisson's ratio
- Hardening rule type
- Material parameters (depending on hardening rule)
- Barlat yield surface exponent
- Chaboche-Rousselier hardening parameters
- Lankford parameters (constant or tabulated)
- Barlat89 parameters
- Material axis options
- Cowper-Symonds strain rate model coefficients
- Volume correction curve
- Optional load curves for biaxial stress and shear stress

The Barlat YLD2000 material model was adapted by Barlat et al. in 2003 [30]. This model, which is an improvement over the Barlat YLD96 model, is developed for shell elements only. With respect to finite element simulations, there were several shortcomings associated with the original YLD96 yield function. First, there was no proof of convexity which is important to assure numerical stability and uniqueness in finite element simulations. Second, the derivatives of the YLD96 yield function were difficult to obtain analytically which makes it difficult to program in a finite element environment. Lastly, while the plane stress implementation of the YLD96 formulation does lead to accurate simulation results, full stress state simulations often lead to some numerical issues. This is likely due to the complexity of the YLD96 formulation and have been seen in practice [30].

The general strategy of this new formulation is to increase stability of incompressible anisotropic plasticity, guarantee convexity and improve the implementation in finite element codes, such as LS-DYNA. Additionally, the authors attempted to take all stresses and Lankford parameters (for each direction) into account for plane stress simulations.

The following are typical inputs used for the Barlat YLD2000 material model [11]:

- Mass density
- Young's modulus (constant or load curve as a function of plastic strain)
- Poisson's ratio
- Material parameter flag

- Hardening parameter
- Material parameters (for exponential hardening, Voce, Hansel, Gosh, and Hockett-Sherby)
- Cowper-Symonds strain rate parameters
- Flow potential exponents
- Chaboche-Rousselier kinematic hardening parameters
- Yield stress in 0-degree, 45-degree and 90-degree directions
- Lankford parameters in 0-degree, 45-degree and 90-degree directions
- Individual xx, yy, xy components of stress on yield surface
- Individual xx, yy, xy components of tangent on yield surface
- Adiabatic temperature calculation options
- Initial temperature and reference temperatures
- Hardening law parameters
- Material axis options
- Post-forming options/parameters

The “Weak and Strong Texture model” is an anisotropic viscoplastic material model that utilizes two yield criteria: a strong texture model (YLD2003) outlined by Aretz [33] and a weak texture model (YLD89) outlined by Barlat and Lian [20]. In comparison to the YLD89 formulation, the YLD2003 formulation includes eight anisotropy parameters that has a simple mathematical form; thus making it efficient for

computational analysis. Like many of the other anisotropic material models, this model is for shell elements in plane stress.

To implement the YLD2003 formulation, the user has two options: prescribe the eight (8) anisotropic parameters individually, or specify yield stresses. If the yield stresses are defined, then the set material parameters of YLD2003 are internally calculated within the material routine. To implement the YLD89 formulation, the user can specify the four anisotropic material parameters individually. Additionally, this model does include strain rate and failure options.

The following are typical inputs used for the Weak and Strong Texture model [11]:

- Mass density
- Young's modulus
- Poisson's ratio
- Failure criterion options
- Initial mean value of yield stress
- Isotropic hardening parameters
- YLD2003 parameters
- Yield stress in 0-degree, 45-degree, 90-degree and biaxial
- Lankford parameters in 0-degree, 45-degree, 90-degree and biaxial
- YLD89 parameters
- Kinematic hardening parameters
- Strain rate parameters

The Hill 90 material model was designed for modeling anisotropic material sheets under plane stress conditions [11]. Fundamentally, the features of this model are the same as the Three-Parameter Barlat Plasticity model. However, the yield function and associated flow formulation are replaced with the Hill 90 yield function [34]. Like the Three-parameter Barlat Plasticity model, this model allows for the direct specification of the Lankford parameters for the definition of the anisotropy.

In this material model, there are many options when defining the hardening rule including: linear, exponential (Swift), tabulated curve, tabulated table with strain rate effects, exponential (Voce, Gosh, or Hockett-Sherby), tabulated curves in each of three material directions, table with temperature dependence or a 3D table with temperature and strain rate dependence. Depending on the hardening rule, different material parameters can be defined. In addition to the hardening rule, the Lankford parameters in the 0-degree, 45-degree, and 90-degree directions can be defined as a constant value or tabulated as a function of plastic strain and temperature. Unlike the Three-Parameter Barlat Plasticity model, this model will allow the user to specify the exponent (m) on the Hill yield surface (as opposed to the Barlat yield surface).

The following are typical inputs used for the Hill90 material model [11]:

- Mass density
- Young's modulus (constant or load curve as a function of plastic strain)
- Poisson's ratio
- Hardening rule type
- Material parameters (depending on hardening rule)

- Hill yield surface exponent
- Chaboche-Rousselier hardening parameters
- Lankford parameters (constant or tabulated)
- Hill90 parameters
- Material axis options
- Cowper-Symonds strain rate model coefficients
- Volume correction curve
- User defined failure flag

CHAPTER 3 - METHODOLOGY

3.1 – Material Law

This section describes the general theory and description of this new anisotropic material model. The description of the yield function is presented as well as the formulation of the flow rule. These components are used, in conjunction with an existing finite element code to verify and validate the model.

3.1.1 – Yield Surface

The goal of this research is to develop a yield surface that allows for directional asymmetry. A plasticity model with asymmetry means that the model allows for different values of yield stress in tension and compression. Directional asymmetry therefore implies that the ratio of tensile to compressive yield can depend on the material direction. Furthermore, this model is to be designed so that the yield surface is distortional, or evolving with plastic deformation. At the time of this writing, no prior implementation of a plasticity model with directional asymmetry is known to the author although this phenomenon is clearly measured in certain HCP metals such as titanium or magnesium.

To begin, this model is based on the foundation set by Buyuk in his development of a tabulated thermos-viscoplastic material model with regularized failure for dynamic ductile failure prediction of structures under impact loading [1]. This model, also known as the Tabulated Johnson-Cook material model, is isotropic and symmetric. The yield surface of this model is based on the von Mises yield criterion where the inputs are based on quasistatic and dynamic tensile tests.

Equation 9: Tabulated Johnson-Cook material model yield formulation

$$\sigma_{vm} \leq \sigma_y(\varepsilon_p, \dot{\varepsilon}_p, T)$$

Equation 10: Tabulated Johnson-Cook material model thermal formulation

$$T = T_R + \int \beta(\dot{\varepsilon}_p) \frac{\sigma_y d\varepsilon_p}{\rho C_p}$$

The added value of the tabulated Johnson-Cook model is the ability to add tabulated dependency of the parameters. In ballistic or impact simulations, it can be very important to consider thermal or rate dependencies in the material; this model allows for that type of analysis. Similar to the Tabulated Johnson-Cook model, this new material model will have tabulated inputs.

Soon after the Tabulated Johnson-Cook model was presented, a more advanced variant was developed. In 2015, Sengoz presented the Generalized Yield Surface (GYS) variant of the Tabulated Johnson-Cook model [13]. This model allows for the simulation of isotropic materials that may have different yield stress values in tension, compression and shear. The key attributes of this model are that it is: isotropic (independent of the reference system), deviatoric (independent of the pressure), and the yield surface is of the third order (the sign of the stress is maintained). To accomplish this, Sengoz utilized the Lode Parameter, which is defined from the third deviatoric stress invariant.

Equation 11: Lode Parameter as used in the Generalized Yield Surface Model

$$\theta_L = \frac{27J_3}{2\sigma_{vm}^3} = \frac{27s_1s_2s_3}{2\sigma_{vm}^3} = \frac{27\det(s)}{2\sigma_{vm}^3} = \frac{27}{2\sigma_{vm}^3} \begin{vmatrix} \sigma_{xx} + p & \sigma_{xy} & \sigma_{xz} \\ \sigma_{yx} & \sigma_{yy} + p & \sigma_{yz} \\ \sigma_{zx} & \sigma_{zy} & \sigma_{zz} + p \end{vmatrix}$$

The key component of the Generalized Yield Surface model is the ability to model isotropic asymmetry through the dependency of the yield stress in the Lode Parameter.

Equation 12: Generalized Yield Surface material model yield function formulation

$$\sigma_{vm}[c_1(\varepsilon_p, \dot{\varepsilon}_p, T) + c_2(\varepsilon_p, \dot{\varepsilon}_p, T)\theta_L + c_3(\varepsilon_p, \dot{\varepsilon}_p, T)\theta_L^2] \leq \sigma_t(\varepsilon_p, \dot{\varepsilon}_p, T)$$

This formulation of the yield surface is based on the tensile yield strength, as it is referenced on the right side of Equation 12. The coefficients c_1 , c_2 and c_3 depend on the equivalent plastic strain, equivalent plastic strain rate and the temperature. These dependencies are tabulated in order to allow for distortional evolution of the tension/compression ratio with plastic deformation. Although other asymmetric models have been implemented in the past, the Generalized Yield Surface model is the first distortional, or tabulated, asymmetric material model. This means that the tension/compression ratio is dependent on the plastic deformation.

In the Generalized Yield Surface model, the values of the Lode parameter are one if the element is in uniaxial tension, negative one in the case of uniaxial compression, and zero in the case of pure shear. These examples show how this model allows for the computation of the coefficients to depend on the measured values of yield stress in tension, compression and pure shear.

Equation 13: Generalized Yield Surface computation of c coefficients

$$\left\{ \begin{array}{l} \sigma_t[c_1 + c_2 + c_3] \leq \sigma_t \\ \sigma_c[c_1 - c_2 + c_3] \leq \sigma_t \\ \sqrt{3}\sigma_s[c_1] \leq \sigma_t \end{array} \right\} \rightarrow \left\{ \begin{array}{l} c_1 + c_2 + c_3 = 1 \\ c_1 - c_2 + c_3 = \frac{\sigma_t}{\sigma_c} \\ c_1 = \frac{\sigma_t}{\sqrt{3}\sigma_s} \end{array} \right\}$$

Embedded into the Generalized Yield Surface implementation is a check for yield surface convexity. This material model not only checks for yield surface convexity at each time step, but also adjusts the parameters to ensure a convex surface.

The material model presented in this dissertation is an orthotropic implementation of the Generalized Yield Surface material model. Orthotropic material models have two planes of symmetry. This is different from monoclinic models that have only one plane of symmetry, or completely anisotropic models that have no symmetry. Since orthotropic models depend on directionality, the yield condition can only be written in the material reference frame. One way to describe the material reference frame is to use unit vectors in each of the Cartesian directions [11] where the x-axis is the rolling or extrusion direction, the y-axis is the long transverse or 90-degree direction and the z-axis is the short transverse or thickness direction.

Equation 14: Definition of material directions

$$\begin{aligned}\vec{e}_x &= \vec{a} \\ \vec{e}_y &= \vec{a} \times \vec{c} \\ \vec{e}_z &= \vec{c} = \vec{a} \times \vec{d}\end{aligned}$$

To implement this orthotropic dependence, the orthotropic third deviatoric invariant is generalized according to Cazacu and Barlat [35].

Equation 15: Orthotropic third deviatoric invariant

$$\begin{aligned}
J_3^o = & \frac{1}{27}(b_1 + b_2)\sigma_{xx}^3 + \frac{1}{27}(b_3 + b_4)\sigma_{yy}^3 + \frac{1}{27}(2b_1 + 2b_4 - b_2 - b_3)\sigma_{zz}^3 \\
& - \frac{1}{9}(b_1\sigma_{yy} + b_2\sigma_{zz})\sigma_{xx}^2 - \frac{1}{9}(b_3\sigma_{zz} + b_4\sigma_{xx})\sigma_{yy}^2 \\
& - \frac{1}{9}\left((b_1 - b_2 + b_4)\sigma_{xx} + (b_1 - b_3 + b_4)\sigma_{yy}\right)\sigma_{zz}^2 + \frac{2}{9}(b_1 + b_4)\sigma_{xx}\sigma_{zz}\sigma_{yy} \\
& - \frac{\sigma_{xz}^2}{3}(2b_9\sigma_{yy} - b_8\sigma_{zz} - (2b_9 - b_8)\sigma_{xx}) - \frac{\sigma_{xy}^2}{3}(2b_{10}\sigma_{zz} - b_5\sigma_{yy} - (2b_{10} - b_5)\sigma_{xx}) \\
& - \frac{\sigma_{yz}^2}{3}(-b_7\sigma_{zz} - b_6\sigma_{yy} + (b_6 + b_7)\sigma_{xx}) + 2b_{11}\sigma_{xy}\sigma_{yz}\sigma_{zx}
\end{aligned}$$

To verify that this third deviatoric invariant is zero under hydrostatic loading,

Equation 15 can be rewritten.

Equation 16: Orthotropic Lode Parameter under hydrostatic loading

$$\begin{aligned}
\frac{J_3^o}{p^3} = & \frac{1}{27}(b_1 + b_2) + \frac{1}{27}(b_3 + b_4) + \frac{1}{27}(2b_1 + 2b_4 - b_2 - b_3) - \frac{1}{9}(b_1 + b_2) \\
& - \frac{1}{9}(b_3 + b_4) - \frac{1}{9}\left((b_1 - b_2 + b_4) + (b_1 - b_3 + b_4)\right) + \frac{2}{9}(b_1 + b_4) = 0
\end{aligned}$$

It can also be confirmed that this formulation of the third deviatoric invariant is isochoric.

Equation 17: Isochoric condition of third deviatoric invariant

$$J_3^o(\boldsymbol{\sigma}) = J_3^o(\boldsymbol{\sigma} + p\boldsymbol{\delta}) \quad \forall \boldsymbol{\sigma}, \forall p$$

This formulation of the third deviatoric invariant is essential because it provides 11 independent coefficients that can be used to correlate a yield surface to anisotropic material testing programs. Using this third deviatoric invariant, an orthotropic Lode parameter can be formulated.

Equation 18: Orthotropic Lode Parameter

$$\theta_L^o = \frac{27J_3^o}{2\sigma_{vm}^3}$$

The uniaxial states of stress in the 0-degree, 90-degree, 45-degree and thickness directions can be written in tensor notation. The state of stress in tension and compression only differ by the sign off the non-zero stress components.

Equation 19: Uniaxial state of stress in 0-degree direction

$$\begin{pmatrix} \sigma_{xx} & 0 & 0 \\ 0 & 0 & 0 \\ 0 & 0 & 0 \end{pmatrix} = \begin{pmatrix} \sigma_{00} & 0 & 0 \\ 0 & 0 & 0 \\ 0 & 0 & 0 \end{pmatrix}$$

Equation 20: Uniaxial state of stress in 90-degree direction

$$\begin{pmatrix} 0 & 0 & 0 \\ 0 & \sigma_{yy} & 0 \\ 0 & 0 & 0 \end{pmatrix} = \begin{pmatrix} 0 & 0 & 0 \\ 0 & \sigma_{90} & 0 \\ 0 & 0 & 0 \end{pmatrix}$$

Equation 21: Uniaxial state of stress in 45-degree direction

$$\begin{pmatrix} \sigma_{xx} & \sigma_{xy} & 0 \\ \sigma_{yx} & \sigma_{yy} & 0 \\ 0 & 0 & 0 \end{pmatrix} = \frac{1}{2} \begin{pmatrix} \sigma_{45} & \sigma_{45} & 0 \\ \sigma_{45} & \sigma_{45} & 0 \\ 0 & 0 & 0 \end{pmatrix}$$

Equation 22: Uniaxial state of stress in thickness direction

$$\begin{pmatrix} 0 & 0 & 0 \\ 0 & 0 & 0 \\ 0 & 0 & \sigma_{zz} \end{pmatrix} = \begin{pmatrix} 0 & 0 & 0 \\ 0 & 0 & 0 \\ 0 & 0 & \sigma_{th} \end{pmatrix}$$

The calculation of the orthotropic Lode parameter (Equation 18) for uniaxial states of stress can be calculated based on the stress components.

Equation 23: Orthotropic Lode Parameter for uniaxial state of stress (0-degree)

$$\theta_L^o \left[\begin{pmatrix} \sigma_{xx} & 0 & 0 \\ 0 & 0 & 0 \\ 0 & 0 & 0 \end{pmatrix} \right] = \frac{27J_3^o}{2\sigma_{vm}^3} = \frac{27}{2\sigma_{vm}^3} (b_1 + b_2) \sigma_{xx}^3 = \frac{b_1 + b_2}{2} \frac{\sigma_{xx}}{|\sigma_{xx}|} = \alpha_{00} \frac{\sigma_{xx}}{|\sigma_{xx}|}$$

Equation 24: Orthotropic Lode Parameter for uniaxial state of stress (90-degree)

$$\theta_L^o \left[\begin{pmatrix} 0 & 0 & 0 \\ 0 & \sigma_{yy} & 0 \\ 0 & 0 & 0 \end{pmatrix} \right] = \frac{27J_3^o}{2\sigma_{vm}^3} = \frac{27}{2\sigma_{vm}^3} (b_3 + b_4) \sigma_{yy}^3 = \frac{b_3 + b_4}{2} \frac{\sigma_{yy}}{|\sigma_{yy}|} = \alpha_{90} \frac{\sigma_{yy}}{|\sigma_{yy}|}$$

Equation 25: Orthotropic Lode Parameter for uniaxial state of stress (thickness)

$$\begin{aligned}\theta_L^o \left[\begin{pmatrix} 0 & 0 & 0 \\ 0 & 0 & 0 \\ 0 & 0 & \sigma_{zz} \end{pmatrix} \right] &= \frac{27J_3^o}{2\sigma_{vm}^3} = \frac{27}{2\sigma_{vm}^3} (2b_1 + 2b_4 - b_2 - b_3) \sigma_{zz}^3 \\ &= \frac{2b_1 + 2b_4 - b_2 - b_3}{2} \frac{\sigma_{zz}}{|\sigma_{zz}|} = \alpha_{th} \frac{\sigma_{zz}}{|\sigma_{zz}|}\end{aligned}$$

Equation 26: Orthotropic Lode Parameter for uniaxial state of stress (45-degree)

$$\begin{aligned}\theta_L^o \left[\begin{pmatrix} \sigma_{xx} & \sigma_{xy} & 0 \\ \sigma_{yx} & \sigma_{yy} & 0 \\ 0 & 0 & 0 \end{pmatrix} \right] &= \frac{27J_3^o}{2\sigma_{vm}^3} \\ &= \frac{27}{2\sigma_{vm}^3} \left[\frac{1}{27} (b_1 + b_2) \sigma_{xx}^3 + \frac{1}{27} (b_3 + b_4) \sigma_{yy}^3 - \frac{1}{9} (b_1 \sigma_{yy} \sigma_{xx}^2 + b_4 \sigma_{xx} \sigma_{yy}^2) \right. \\ &\quad \left. - \frac{\sigma_{xy}^2}{3} (-b_5 \sigma_{yy} - (2b_{10} - b_5) \sigma_{xx}) \right] \\ &= \frac{27}{2\sigma_{vm}^3} \frac{1}{8} \left[\frac{1}{27} (-2b_1 + b_2 + b_3 - 2b_4 + 18b_{10}) \sigma_{45}^3 \right] \\ &= \frac{-2b_1 + b_2 + b_3 - 2b_4 + 18b_{10}}{16} \frac{\sigma_{45}}{|\sigma_{45}|} = \alpha_{45} \frac{\sigma_{45}}{|\sigma_{45}|}\end{aligned}$$

In addition to the generalization of the Lode parameter and third deviatoric invariant components (for orthotropic compression), the von Mises yield function component could also be generalized to obtain an orthotropic yield function in tension. One generalization of the von Mises yield function is the Hill yield function [21].

Equation 27: Hill yield function

$$\sigma_{hill}^2 = F(\sigma_{yy} - \sigma_{zz})^2 + G(\sigma_{zz} - \sigma_{xx})^2 + H(\sigma_{xx} - \sigma_{yy})^2 + 2L\sigma_{yz}^2 + 2M\sigma_{xz}^2 + 2N\sigma_{xy}^2 \leq \sigma_{00}^2$$

For each of the uniaxial stress states, the Hill yield function can be simplified to the directional stress component and the Hill coefficients.

Equation 28: Hill yield function for uniaxial state of stress (0-degree)

$$\sigma_{hill}^2 = (G + H)\sigma_{xx}^2 = (G + H)\sigma_{00}^2 \therefore G + H = 1$$

Equation 29: Hill yield function for uniaxial state of stress (90-degree)

$$\sigma_{hill}^2 = (F + H)\sigma_{yy}^2 = (F + H)\sigma_{90}^2$$

Equation 30: Hill yield function for uniaxial state of stress (thickness)

$$\sigma_{hill}^2 = (G + F)\sigma_{zz}^2 = (G + F)\sigma_{th}^2$$

Equation 31: Hill yield function for uniaxial state of stress (45-degree)

$$\sigma_{hill}^2 = F(\sigma_{yy})^2 + G(\sigma_{xx})^2 + H(\sigma_{xx} - \sigma_{yy})^2 + 2N\sigma_{xy}^2 = (F + G + 2N)\frac{\sigma_{45}^2}{4}$$

With these six independent parameters, the Hill yield function allows for the fitting of the yield stress in tension in each of the four different directions. Now that the orthotropic Lode parameter and the Hill yield function have been defined, the original formulation of the Generalized Yield Surface material model (Equation 12) can be further generalized to provide a yield function that includes directional asymmetry.

Equation 32: Orthotropic generalization of GYS material model

$$\begin{aligned} \sigma_{vm}[c_1(\varepsilon_p, \dot{\varepsilon}_p, T) + c_2(\varepsilon_p, \dot{\varepsilon}_p, T)\theta_L + c_3(\varepsilon_p, \dot{\varepsilon}_p, T)\theta_L^2] &\leq \sigma_t(\varepsilon_p, \dot{\varepsilon}_p, T) \\ \rightarrow \sigma_{hill}[c_1(\varepsilon_p, \dot{\varepsilon}_p, T) + c_2(\varepsilon_p, \dot{\varepsilon}_p, T)\theta_L^{o1} + c_3(\varepsilon_p, \dot{\varepsilon}_p, T)(\theta_L^{o2})^2] &\leq \sigma_{00-t}(\varepsilon_p, \dot{\varepsilon}_p, T) \end{aligned}$$

By using two orthotropic Lode parameters, which resulted in 22 independent coefficients, directional asymmetry can be implemented in this plasticity model. Additionally, with the implementation of the Hill yield function, instead of the von Mises yield function, this plasticity model allows for directionality in tension. In this new formulation, the 0-degree tensile yield is chosen as the reference yield stress.

Now that the orthotropic coefficients are defined in the yield function, they must also be determined based on the uniaxial states of stress. For example, the first and

second orthotropic Lode parameters can be determined for the 0-degree uniaxial tension and compression cases. In this case, the 0-degree formulation coincides with the previously developed Generalized Yield Surface material model.

Equation 33: Determination of the 0-degree orthotropic coefficients

$$\begin{cases} \sigma_{oo-t}[c_1 + c_2\alpha_{00} + c_3\beta_{00}^2] \leq \sigma_{oo-t} \\ \sigma_{oo-c}[c_1 - c_2\alpha_{00} + c_3\beta_{00}^2] \leq \sigma_{oo-t} \end{cases} \rightarrow \begin{cases} c_1 + c_2 + c_3 = 1 \\ c_1 - c_2 + c_3 = \frac{\sigma_{oo-t}}{\sigma_{oo-c}} \end{cases}$$

$\alpha_{00} = 1$ and $\beta_{00} = 1$

Equation 34: Determination of the 90-degree orthotropic coefficients

$$\begin{cases} \sqrt{F+H}\sigma_{90-t}[c_1 + c_2\alpha_{90} + c_3\beta_{90}^2] \leq \sigma_{oo-t} \\ \sqrt{F+H}\sigma_{90-c}[c_1 - c_2\alpha_{90} + c_3\beta_{90}^2] \leq \sigma_{oo-t} \end{cases} \rightarrow \begin{cases} c_1 + c_2\alpha_{90} + c_3\beta_{90}^2 = 1 \\ c_1 - c_2\alpha_{90} + c_3\beta_{90}^2 = \frac{\sigma_{oo-t}}{\sqrt{F+H}\sigma_{90-c}} \end{cases}$$

$$\alpha_{90} = \frac{1 - \frac{\sigma_{90-t}}{\sigma_{90-c}}}{2c_2} = \frac{1 - \frac{\sigma_{90-t}}{\sigma_{90-c}}}{1 - \frac{\sigma_{00-t}}{\sigma_{00-c}}}$$

$$\beta_{90}^2 = \frac{1 + \frac{\sigma_{90-t}}{\sigma_{90-c}} - 2c_1}{2c_3} = \frac{1 + \frac{\sigma_{90-t}}{\sigma_{90-c}} - 2c_1}{1 + \frac{\sigma_{00-t}}{\sigma_{00-c}} - 2c_1}$$

Equation 35: Determination of the 45-degree orthotropic coefficients

$$\begin{cases} \frac{1}{2}\sqrt{F+G+2N}\sigma_{45-t}[c_1 + c_2\alpha_{45} + c_3\beta_{45}^2] \leq \sigma_{oo-t} \\ \frac{1}{2}\sqrt{F+G+2N}\sigma_{45-c}[c_1 - c_2\alpha_{45} + c_3\beta_{45}^2] \leq \sigma_{oo-t} \end{cases}$$

$$\rightarrow \begin{cases} c_1 + c_2\alpha_{45} + c_3\beta_{45}^2 = 1 \\ c_1 - c_2\alpha_{45} + c_3\beta_{45}^2 = \frac{2\sigma_{oo-t}}{\sqrt{F+G+2N}\sigma_{45-c}} \end{cases}$$

$$\alpha_{45} = \frac{1 - \frac{\sigma_{45-t}}{\sigma_{45-c}}}{2c_2} = \frac{1 - \frac{\sigma_{45-t}}{\sigma_{45-c}}}{1 - \frac{\sigma_{00-t}}{\sigma_{00-c}}}$$

$$\beta_{45}^2 = \frac{1 + \frac{\sigma_{45-t}}{\sigma_{45-c}} - 2c_1}{2c_3} = \frac{1 + \frac{\sigma_{45-t}}{\sigma_{45-c}} - 2c_1}{1 + \frac{\sigma_{00-t}}{\sigma_{00-c}} - 2c_1}$$

Equation 36: Determination of the thickness orthotropic coefficients

$$\left\{ \begin{array}{l} \sqrt{F+G}\sigma_{th-t}[c_1 + c_2\alpha_{th} + c_3\beta_{th}^2] \leq \sigma_{oo-t} \\ \sqrt{F+G}\sigma_{th-c}[c_1 - c_2\alpha_{th} + c_3\beta_{th}^2] \leq \sigma_{oo-t} \end{array} \right\} \rightarrow \left\{ \begin{array}{l} c_1 + c_2\alpha_{th} + c_3\beta_{th}^2 = 1 \\ c_1 - c_2\alpha_{th} + c_3\beta_{th}^2 = \frac{\sigma_{oo-t}}{\sqrt{F+G}\sigma_{th-c}} \end{array} \right\}$$

$$\alpha_{45} = \frac{1 - \frac{\sigma_{th-t}}{\sigma_{th-c}}}{2c_2} = \frac{1 - \frac{\sigma_{th-t}}{\sigma_{th-c}}}{1 - \frac{\sigma_{oo-t}}{\sigma_{oo-c}}}$$

$$\beta_{45}^2 = \frac{1 + \frac{\sigma_{th-t}}{\sigma_{th-c}} - 2c_1}{2c_3} = \frac{1 + \frac{\sigma_{th-t}}{\sigma_{th-c}} - 2c_1}{1 + \frac{\sigma_{oo-t}}{\sigma_{oo-c}} - 2c_1}$$

By using the eight conditions derived for each of the orthotropic Lode parameters (two in each direction), the independent parameters (' b ' values) can be determined. For the first orthotropic Lode parameter, a ' b ' variable is used for each of the 11 independent coefficients. For the second orthotropic Lode parameters a ' d ' variable is used for each of the 11 independent coefficients. For each Lode parameter, there are four equations and five parameters. Therefore, one parameter can be freely chosen. Additionally, six parameters are not used in this formulation, or do not appear in the four orthotropic Lode parameter conditions, and can also be freely chosen. For those free coefficients, the value will be set to one. In this case, the free coefficients will be b_1 and d_1 which are set to one. Table 2 shows the coefficients of the orthotropic Lode parameters.

Table 2: Coefficients of the orthotropic Lode parameters

First orthotropic Lode parameter coefficients	Second orthotropic Lode parameter coefficients
$\frac{b_1 + b_2}{2} = \alpha_{00} = 1$	$\frac{d_1 + d_2}{2} = \beta_{00} = 1$
$\frac{b_3 + b_4}{2} = \alpha_{90}$	$\frac{d_3 + d_4}{2} = \beta_{90}$
$\frac{2b_1 + 2b_4 - b_2 - b_3}{2} = \alpha_{th}$	$\frac{2d_1 + 2d_4 - d_2 - d_3}{2} = \beta_{th}$
$\frac{-2b_1 + b_2 + b_3 + 18b_{10}}{16} = \alpha_{45}$	$\frac{-2d_1 + d_2 + d_3 + 18d_{10}}{16} = \beta_{45}$

In some cases, especially with tabulated input values, the value of β^2 will be equal to a negative number (ie. Equation 34). When this happens a computational error will be returned in the form of a NaN. To remedy this, a condition can be established that will force β^2 to be real, and not complex. The value of β^2 will be real if one of the two conditionals are met.

Equation 37: First condition for beta coefficient

$$\beta_{90}^2 = \frac{1 + \frac{\sigma_{90-t}}{\sigma_{90-c}} - 2c_1}{2c_3} = \frac{1 + \frac{\sigma_{90-t}}{\sigma_{90-c}} - 2c_1}{1 + \frac{\sigma_{00-t}}{\sigma_{00-c}} - 2c_1}$$

$$1 + \frac{\sigma_{90-t}}{\sigma_{90-c}} - 2c_1 > 0 \rightarrow 1 + \frac{\sigma_{00-t}}{\sigma_{00-c}} - 2c_1 > 0$$

$$1 + \frac{\sigma_{90-t}}{\sigma_{90-c}} > 2c_1 \rightarrow 1 + \frac{\sigma_{00-t}}{\sigma_{00-c}} > 2c_1$$

$$c_1 < \frac{1}{2} \min \left[1 + \frac{\sigma_{90-t}}{\sigma_{90-c}}, 1 + \frac{\sigma_{00-t}}{\sigma_{00-c}} \right]$$

Equation 38: Second condition for beta coefficient

$$\beta_{90}^2 = \frac{1 + \frac{\sigma_{90-t}}{\sigma_{90-c}} - 2c_1}{2c_3} = \frac{1 + \frac{\sigma_{90-t}}{\sigma_{90-c}} - 2c_1}{1 + \frac{\sigma_{00-t}}{\sigma_{00-c}} - 2c_1}$$

$$1 + \frac{\sigma_{90-t}}{\sigma_{90-c}} - 2c_1 < 0 \rightarrow 1 + \frac{\sigma_{00-t}}{\sigma_{00-c}} - 2c_1 < 0$$

$$1 + \frac{\sigma_{90-t}}{\sigma_{90-c}} < 2c_1 \rightarrow 1 + \frac{\sigma_{00-t}}{\sigma_{00-c}} < 2c_1$$

$$c_1 > \frac{1}{2} \max \left[1 + \frac{\sigma_{90-t}}{\sigma_{90-c}}, 1 + \frac{\sigma_{00-t}}{\sigma_{00-c}} \right]$$

If one of these conditions are not met, then the value of c_1 can be adjusted to ensure that the value of β^2 is positive. For example, if c_1 is greater than the value shown in Equation 37, then the value of c_1 will be reduced so it is less than the specified value in the conditional. Adjusting the values of c_1 and c_3 while leaving c_2 unmodified will affect only the shear strength in the material model thus generating a deviation in the response from the measured yield curve in pure shear.

3.1.2 – Flow Rule

This plasticity methodology is based on the associated flow rule. Given any stress state, there exists a corresponding point in six-dimensional stress space. The yield function can represent a surface where the plastic strain rate is a vector in this space. This plastic strain rate vector is perpendicular to this surface [36]. The general form of the flow rule implemented in this model is shown in Equation 39.

Equation 39: Associated flow rule

$$\dot{\boldsymbol{\epsilon}}^p = \dot{\lambda} \frac{df}{d\boldsymbol{\sigma}} = \dot{\lambda} \begin{pmatrix} \frac{\partial f}{\partial \sigma_{xx}} & \frac{\partial f}{\partial \sigma_{xy}} & \frac{\partial f}{\partial \sigma_{xz}} \\ \frac{\partial f}{\partial \sigma_{yx}} & \frac{\partial f}{\partial \sigma_{yy}} & \frac{\partial f}{\partial \sigma_{yz}} \\ \frac{\partial f}{\partial \sigma_{zx}} & \frac{\partial f}{\partial \sigma_{zy}} & \frac{\partial f}{\partial \sigma_{zz}} \end{pmatrix}$$

In this equation, the variable $\dot{\lambda}$ is the plastic multiplier which allows the plastic strain rate tensor to be proportional to the stress gradient of the yield surface. As f has the dimension of stress, it is clear that the plastic multiplier has the dimension of strain rate. To achieve associated flow computationally, the derivative of the yield surface must be calculated. Due to the complexity of the yield function, this can be accomplished in two stages: derivative of the Hill component, and the derivative of the orthotropic third invariant.

Equation 40: Derivatives of the Hill yield function

$$\begin{aligned} \sigma_{hill}^2 &= F(\sigma_{yy} - \sigma_{zz})^2 + G(\sigma_{zz} - \sigma_{xx})^2 + H(\sigma_{xx} - \sigma_{yy})^2 + 2L\sigma_{yz}^2 + 2M\sigma_{xz}^2 + 2N\sigma_{xy}^2 \\ \frac{\partial \sigma_{hill}^2}{\partial \sigma_{xx}} &= -2G(\sigma_{zz} - \sigma_{xx}) + 2H(\sigma_{xx} - \sigma_{yy}) \\ \frac{\partial \sigma_{hill}^2}{\partial \sigma_{yy}} &= 2F(\sigma_{yy} - \sigma_{zz}) - 2H(\sigma_{xx} - \sigma_{yy}) \\ \frac{\partial \sigma_{hill}^2}{\partial \sigma_{yz}} &= -2F(\sigma_{yy} - \sigma_{zz}) + 2G(\sigma_{zz} - \sigma_{xx}) \\ \frac{\partial \sigma_{hill}^2}{\partial \sigma_{xy}} &= 2N\sigma_{xy} \\ \frac{\partial \sigma_{hill}^2}{\partial \sigma_{yz}} &= 2L\sigma_{yz} \\ \frac{\partial \sigma_{hill}^2}{\partial \sigma_{xz}} &= 2M\sigma_{xz} \end{aligned}$$

Equation 41: Derivatives of the third orthotropic invariant

$$\begin{aligned}
J_3^o &= \frac{1}{27} (b_1 + b_2) \sigma_{xx}^3 + \frac{1}{27} (b_3 + b_4) \sigma_{yy}^3 + \frac{1}{27} (2b_1 + 2b_4 - b_2 - b_3) \sigma_{zz}^3 \\
&- \frac{1}{9} (b_1 \sigma_{yy} + b_2 \sigma_{zz}) \sigma_{xx}^2 - \frac{1}{9} (b_3 \sigma_{zz} + b_4 \sigma_{xx}) \sigma_{yy}^2 \\
&- \frac{1}{9} \left((b_1 - b_2 + b_4) \sigma_{xx} + (b_1 - b_3 + b_4) \sigma_{yy} \right) \sigma_{zz}^2 + \frac{2}{9} (b_1 + b_4) \sigma_{xx} \sigma_{zz} \sigma_{yy} \\
&- \frac{\sigma_{xz}^2}{3} (2b_9 \sigma_{yy} - b_8 \sigma_{zz} - (2b_9 - b_8) \sigma_{xx}) - \frac{\sigma_{xy}^2}{3} (2b_{10} \sigma_{zz} - b_5 \sigma_{yy} - (2b_{10} - b_5) \sigma_{xx}) \\
&- \frac{\sigma_{yz}^2}{3} (-b_7 \sigma_{zz} - b_6 \sigma_{yy} + (b_6 + b_7) \sigma_{xx}) + 2b_{11} \sigma_{xy} \sigma_{yz} \sigma_{zx}
\end{aligned}$$

$$\begin{aligned}
\frac{\partial J_3^o}{\partial \sigma_{xx}} &= \frac{3}{27} (b_1 + b_2) \sigma_{xx}^2 - \frac{2}{9} (b_1 \sigma_{yy} + b_2 \sigma_{zz}) \sigma_{xx} - \frac{1}{9} b_4 \sigma_{yy}^2 - \frac{1}{9} (b_1 - b_2 + b_4) \sigma_{zz}^2 \\
&+ \frac{2}{9} (b_1 + b_4) \sigma_{zz} \sigma_{yy} - \frac{\sigma_{xz}^2}{3} (-2b_9 + b_8) - \frac{\sigma_{xy}^2}{3} (-2b_{10} + b_5) - \frac{\sigma_{yz}^2}{3} (b_6 + b_7)
\end{aligned}$$

$$\begin{aligned}
\frac{\partial J_3^o}{\partial \sigma_{yy}} &= \frac{3}{27} (b_3 + b_4) \sigma_{yy}^2 - \frac{1}{9} (b_1) \sigma_{xx}^2 - \frac{2}{9} (b_3 \sigma_{zz} + b_4 \sigma_{xx}) \sigma_{yy} - \frac{1}{9} (b_1 - b_3 + b_4) \sigma_{zz}^2 \\
&+ \frac{2}{9} (b_1 + b_4) \sigma_{xx} \sigma_{zz} - \frac{\sigma_{xz}^2}{3} (2b_9) - \frac{\sigma_{xy}^2}{3} (-b_5) - \frac{\sigma_{yz}^2}{3} (-b_6 \sigma_{yy})
\end{aligned}$$

$$\begin{aligned}
\frac{\partial J_3^o}{\partial \sigma_{zz}} &= \frac{3}{27} (2b_1 + 2b_4 - b_2 - b_3) \sigma_{zz}^2 - \frac{1}{9} (b_2) \sigma_{xx}^2 - \frac{1}{9} (b_3) \sigma_{yy}^2 - \frac{2}{9} ((b_1 - b_2 + b_4) \sigma_{xx} \\
&+ (b_1 - b_3 + b_4) \sigma_{yy}) \sigma_{zz} + \frac{2}{9} (b_1 + b_4) \sigma_{xx} \sigma_{yy} - \sigma_{xz}^2 (-b_8) - \sigma_{xy}^2 (2b_{10}) - \sigma_{yz}^2 (-b_7)
\end{aligned}$$

$$\frac{\partial J_3^o}{\partial \sigma_{xy}} = -\frac{2\sigma_{xy}}{3} (2b_{10} \sigma_{zz} - b_5 \sigma_{yy} - (2b_{10} - b_5) \sigma_{xx}) + 2b_{11} \sigma_{yz} \sigma_{xz}$$

$$\frac{\partial J_3^o}{\partial \sigma_{yz}} = -\frac{2\sigma_{yz}}{3} (-b_7 \sigma_{zz} - b_6 \sigma_{yy} - (b_6 - b_7) \sigma_{xx}) + 2b_{11} \sigma_{xy} \sigma_{xz}$$

$$\frac{\partial J_3^o}{\partial \sigma_{xz}} = -\frac{2\sigma_{xz}}{3} (2b_9 \sigma_{yy} - b_8 \sigma_{zz} - (2b_9 - b_8) \sigma_{xx}) + 2b_{11} \sigma_{xy} \sigma_{yz}$$

By using these intermediate derivatives, the flow rule can be calculated from the effective stress equation.

Equation 42: Effective stress

$$\sigma_{eff} = \sigma_{hill} \left(c_1 + c_2 \frac{27J_{31}}{2\sigma_{vm}^3} + c_3 \left(\frac{27J_{32}}{2\sigma_{vm}^3} \right)^2 \right) = \sigma_{hill} \left(c_1 + c_2 \frac{27J_{31}}{2\sigma_{vm}^3} + c_3 \frac{729J_{32}^2}{4\sigma_{vm}^6} \right)$$

Equation 43: Derivative of the effective stress

$$\begin{aligned} \frac{\partial \sigma_{eff}}{\partial \sigma} &= \frac{\partial \sigma_{eff}}{\partial \sigma_{vm}} \frac{3s}{2\sigma_{vm}} + \frac{\partial \sigma_{eff}}{\partial J_{31}} \frac{\partial J_{31}}{\partial \sigma} + \frac{\partial \sigma_{eff}}{\partial J_{32}} \frac{\partial J_{32}}{\partial \sigma} + \frac{\partial \sigma_{eff}}{\partial \sigma_{hill}} \frac{1}{2\sigma_{hill}} \frac{\partial \sigma_{hill}^2}{\partial \sigma} \\ \frac{\partial \sigma_{eff}}{\partial \sigma} &= \left(\sigma_{hill} \left(-3c_2 \frac{27J_{31}}{2\sigma_{vm}^4} - 6c_3 \frac{729J_{32}^2}{4\sigma_{vm}^7} \right) \right) \frac{3s}{2\sigma_{vm}} \\ &+ \left(c_2 \frac{27}{2\sigma_{vm}^2} \frac{\partial J_{31}}{\partial \sigma} + 2c_3 \frac{729J_{32}}{4\sigma_{vm}^5} \frac{\partial J_{32}}{\partial \sigma} \right) \\ &+ \left(c_1 + c_2 \frac{27J_{31}}{\sigma_{vm}^3} + c_3 \left(\frac{27J_{32}}{2\sigma_{vm}^3} \right)^2 \right) \frac{1}{2\sigma_{hill}} \frac{\partial \sigma_{hill}^2}{\partial \sigma} \end{aligned}$$

3.1.3 – Convexity

When developing material models for use in finite element simulations, it is highly desirable to maintain full convexity of the yield surface. Therefore, this model will attempt to enforce convexity in most cases. In this model, convexity is enforced when the inputs are isotropic and symmetric (similar to the Tabulated Johnson-Cook model), isotropic and asymmetric (similar to the Generalized Yield Surface Model), and anisotropic with isotropic asymmetry. The only case where convexity is not enforced internally is in simulations with anisotropic and directional asymmetry. Anisotropic asymmetry is when the tension/compression ratio is not the same in each material direction (0-degree, 45-degree, 90-degree and thickness). Therefore, a model can be

anisotropic with isotropic asymmetry and still be directionally dependent. This case would have enforced convexity of the yield surface.

When this model is used to simulate a material with anisotropy and directional asymmetry, it is recommended that the user manually plot the yield surface to evaluate any areas of concavity. One option is to run a single element simulation and export the components of the yield surface. This process is explained thoroughly in section 3.3.

It is known that the isotropic implementation of this model has a yield surface that is convex because it is based on the Tabulated Johnson-Cook material model formulation [1]. Additionally, the isotropic asymmetric implementation of this new model, which is equivalent to the Generalized Yield Surface model, also has enforced convexity conditions developed by Sengoz [13].

In the Generalized Yield Surface model, the yield parameters c_1 , c_2 and c_3 are not completely arbitrary and only some combinations of these parameters satisfy the convexity requirements. In the material routine, the values of these parameters must fall in a specific range, or convexity region. If not, they are adjusted internally to guarantee convexity of the yield surface.

To ensure convexity in the anisotropic case with non-directional asymmetry, a similar convexity enforcement algorithm is developed. The Hill yield function [21] has seven conditions for the anisotropy parameters that must be met to ensure convexity [37]:

Equation 44: Convexity conditions for Hill yield function

1. $F + H \geq 0$
2. $G + H \geq 0$
3. $F + G \geq 0$
4. $N \geq 0$

5. $L \geq 0$
6. $M \geq 0$
7. $FG + GH + HF \geq 0$

Where:

- a. $2F = \frac{1}{\sigma_2^2} + \frac{1}{\sigma_3^2} - \frac{1}{\sigma_1^2}$
- b. $2G = -\frac{1}{\sigma_2^2} + \frac{1}{\sigma_3^2} + \frac{1}{\sigma_1^2}$
- c. $2H = \frac{1}{\sigma_2^2} - \frac{1}{\sigma_3^2} + \frac{1}{\sigma_1^2}$
- d. $2L = \frac{1}{\sigma_5^2}$
- e. $2M = \frac{1}{\sigma_6^2}$
- f. $2N = \frac{1}{\sigma_4^2}$

For this specific model implementation, these parameter definitions can be re-written as:

Equation 45: Convexity conditions for model implementation of Hill yield function

- a. $F + H = \frac{(\sigma_t^{00})^2}{(\sigma_t^{90})^2}$
- b. $G + H = 1$
- c. $F + G = \frac{(\sigma_t^{00})^2}{(\sigma_t^{tt})^2}$
- d. $L = \frac{3}{2}$
- e. $M = \frac{3}{2}$
- f. $N = 2 \left(\frac{(\sigma_t^{00})^2}{(\sigma_t^{45})^2} - \frac{1}{4}F - \frac{1}{4}G \right)$

Using the definitions of the anisotropy parameters in Equation 45, convexity condition 1 (of Equation 44) is always valid because both the 0-degree tension stress and the 90-degree tension stress are always squared, and thus can never be negative. Convexity condition 2 (of Equation 44) is also always valid because the G and H parameters will always be equal to one when combined. Convexity condition 3 (of

Equation 44) will always be valid because the 0-degree tension stress and the thickness tension stress are always squared, and thus can never be negative. Convexity conditions 5 and 6 (of Equation 44) are also always valid because the L and M parameters will always be equal to three halves.

Convexity condition 4 (of Equation 44) is not inherently always valid in this model and a check must be implemented to investigate any convexity issues. By substitution, the value of N can be simplified and re-written as:

Equation 46: Simplification of Hill convexity condition #4

$$\begin{aligned}
 N &= 2 \left(\frac{(\sigma_t^{00})^2}{(\sigma_t^{45})^2} - \frac{1}{8} \left(\frac{(\sigma_t^{00})^2}{(\sigma_t^{90})^2} + \frac{(\sigma_t^{00})^2}{(\sigma_t^{tt})^2} - 1 \right) - \frac{1}{8} \left(-\frac{(\sigma_t^{00})^2}{(\sigma_t^{90})^2} + \frac{(\sigma_t^{00})^2}{(\sigma_t^{tt})^2} + 1 \right) \right) \\
 N &= 2 \left(\frac{(\sigma_t^{00})^2}{(\sigma_t^{45})^2} + \left(-\frac{1}{8} \frac{(\sigma_t^{00})^2}{(\sigma_t^{90})^2} - \frac{1}{8} \frac{(\sigma_t^{00})^2}{(\sigma_t^{tt})^2} + \frac{1}{8} \right) + \left(\frac{1}{8} \frac{(\sigma_t^{00})^2}{(\sigma_t^{90})^2} - \frac{1}{8} \frac{(\sigma_t^{00})^2}{(\sigma_t^{tt})^2} - \frac{1}{8} \right) \right) \\
 N &= 2 \left(\frac{(\sigma_t^{00})^2}{(\sigma_t^{45})^2} - \frac{1}{8} \frac{(\sigma_t^{00})^2}{(\sigma_t^{90})^2} - \frac{1}{8} \frac{(\sigma_t^{00})^2}{(\sigma_t^{tt})^2} + \frac{1}{8} + \frac{1}{8} \frac{(\sigma_t^{00})^2}{(\sigma_t^{90})^2} - \frac{1}{8} \frac{(\sigma_t^{00})^2}{(\sigma_t^{tt})^2} - \frac{1}{8} \right) \\
 N &= 2 \left(\frac{(\sigma_t^{00})^2}{(\sigma_t^{45})^2} - \frac{1}{8} \frac{(\sigma_t^{00})^2}{(\sigma_t^{tt})^2} - \frac{1}{8} \frac{(\sigma_t^{00})^2}{(\sigma_t^{tt})^2} \right) = 4 \left(\frac{(\sigma_t^{00})^2}{(\sigma_t^{45})^2} - \frac{1}{4} \frac{(\sigma_t^{00})^2}{(\sigma_t^{tt})^2} \right) \\
 \text{Condition: } &\frac{(\sigma_t^{00})^2}{(\sigma_t^{45})^2} - \frac{1}{4} \frac{(\sigma_t^{00})^2}{(\sigma_t^{tt})^2} > 0 \rightarrow 2\sigma_t^{tt} > \sigma_t^{45}
 \end{aligned}$$

The simplified convexity condition 4 (of Equation 44) specifies that the thickness yield stress must always be greater than one half of the 45-degree yield stress. If this is not the case, then the yield surface is not guaranteed to be convex. Convexity condition 7 (of Equation 44) can also be evaluated in the same manner. The definitions of the anisotropy parameters are substituted into the convexity condition and the formula is simplified to the following:

Equation 47: Simplification of Hill convexity condition #7

$$\left(\frac{(\sigma_t^{00})^2}{(\sigma_t^{90})^2} + \frac{(\sigma_t^{00})^2}{(\sigma_t^{tt})^2} - 1 \right) \left(-\frac{(\sigma_t^{00})^2}{(\sigma_t^{90})^2} + \frac{(\sigma_t^{00})^2}{(\sigma_t^{tt})^2} + 1 \right) + \left(\frac{(\sigma_t^{00})^2}{(\sigma_t^{90})^2} - \frac{(\sigma_t^{00})^2}{(\sigma_t^{tt})^2} + 1 \right) \left(2 \frac{(\sigma_t^{00})^2}{(\sigma_t^{tt})^2} \right) > 0$$

$$\frac{(\sigma_t^{00})^4}{(\sigma_t^{90})^4} - \frac{2(\sigma_t^{00})^2}{(\sigma_t^{90})^2} + \frac{(\sigma_t^{00})^4}{(\sigma_t^{tt})^4} - \frac{2(\sigma_t^{00})^2}{(\sigma_t^{tt})^2} - \frac{2(\sigma_t^{00})^4}{(\sigma_t^{90})^2(\sigma_t^{tt})^2} + 1 < 0$$

If $\sigma_t^{00} > 0$ and $\sigma_t^{90} > \sigma_t^{00}$:

$$\frac{(\sigma_t^{00^2} - \sigma_t^{90^2}) \sqrt{\frac{\sigma_t^{00^2} \sigma_t^{90^4}}{(\sigma_t^{00^2} - \sigma_t^{90^2})^2}} + \sigma_t^{00^2} \sigma_t^{90}}{\sigma_t^{00^2} - \sigma_t^{90^2}} < \sigma_t^{tt}$$

$$< \frac{(\sigma_t^{00^2} - \sigma_t^{90^2}) \sqrt{\frac{\sigma_t^{00^2} \sigma_t^{90^4}}{(\sigma_t^{00^2} - \sigma_t^{90^2})^2}} - \sigma_t^{00^2} \sigma_t^{90}}{\sigma_t^{00^2} - \sigma_t^{90^2}}$$

If $\sigma_t^{00} > 0$ and $\sigma_t^{90} < \sigma_t^{00}$:

$$\frac{(-\sigma_t^{00^2} + \sigma_t^{90^2}) \sqrt{\frac{\sigma_t^{00^2} \sigma_t^{90^4}}{(\sigma_t^{00^2} - \sigma_t^{90^2})^2}} + \sigma_t^{00^2} \sigma_t^{90}}{\sigma_t^{00^2} - \sigma_t^{90^2}} < \sigma_t^{tt}$$

$$< \frac{(\sigma_t^{00^2} - \sigma_t^{90^2}) \sqrt{\frac{\sigma_t^{00^2} \sigma_t^{90^4}}{(\sigma_t^{00^2} - \sigma_t^{90^2})^2}} + \sigma_t^{00^2} \sigma_t^{90}}{\sigma_t^{00^2} - \sigma_t^{90^2}}$$

If $\sigma_t^{00} > 0$ and $\sigma_t^{90} > \sigma_t^{00}$:

$$\frac{\sigma_t^{00} \sigma_t^{90}}{\sigma_t^{00} + \sigma_t^{90}} < \sigma_t^{tt} < \frac{-\sigma_t^{00} \sigma_t^{90}}{\sigma_t^{00} - \sigma_t^{90}}$$

If $\sigma_t^{00} > 0$ and $\sigma_t^{90} < \sigma_t^{00}$:

$$\frac{\sigma_t^{00} \sigma_t^{90}}{\sigma_t^{00} + \sigma_t^{90}} < \sigma_t^{tt} < \frac{\sigma_t^{00} \sigma_t^{90}}{\sigma_t^{00} - \sigma_t^{90}}$$

This convexity defines a specific acceptable region for the value of the thickness direction yield stress. This region is shown in Figure 7. If the value of the ratio of the yield stress described in each axis is located inside of the green region, then the Hill yield surface is considered to be convex.

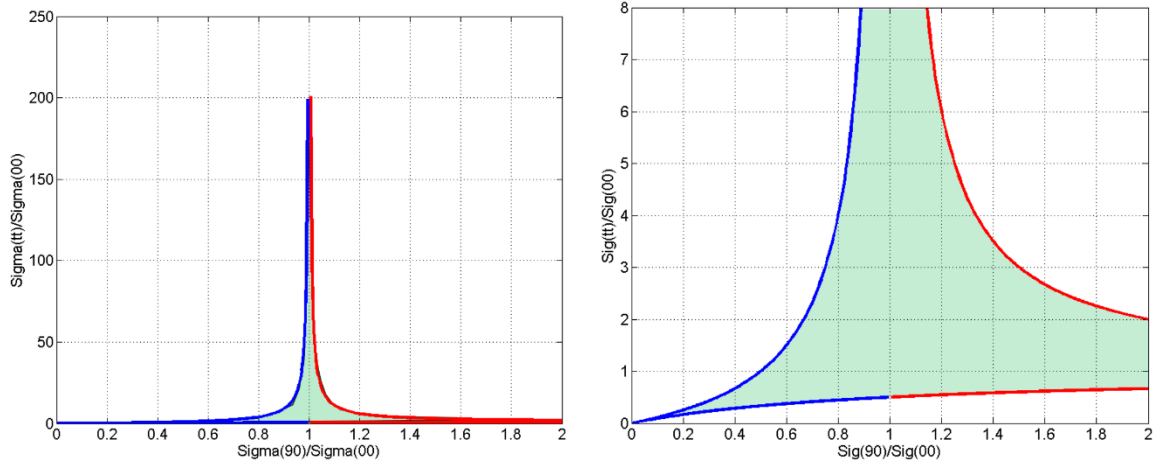


Figure 7: Graphical representation of Hill convexity condition #7

From the seven convexity conditions for the Hill yield function, an algorithm can be developed to ensure that the yield surface, when trying to simulate anisotropic and non-directionally asymmetric materials, is convex. The algorithm to internally force convexity is outlined in Figure 8.

The first step of the convexity check is to see if the tensile thickness yield stress is greater than one half of the 45-degree tension yield stress. If this statement is true, then the algorithm continues, if not, then the value of the tensile thickness yield stress is set to be two times the 45-degree tension yield stress and the algorithm continues. The next

stage is to evaluate if the 0-degree tension yield stress is between zero and the 90-degree tension yield stress. Depending on result of this inequality check, the algorithm can take two different paths through the convexity enforcement algorithm. If the yield stresses are not in the acceptable region described by Figure 7, then the value of the tensile thickness yield stress is adjusted so that convexity is ensured.

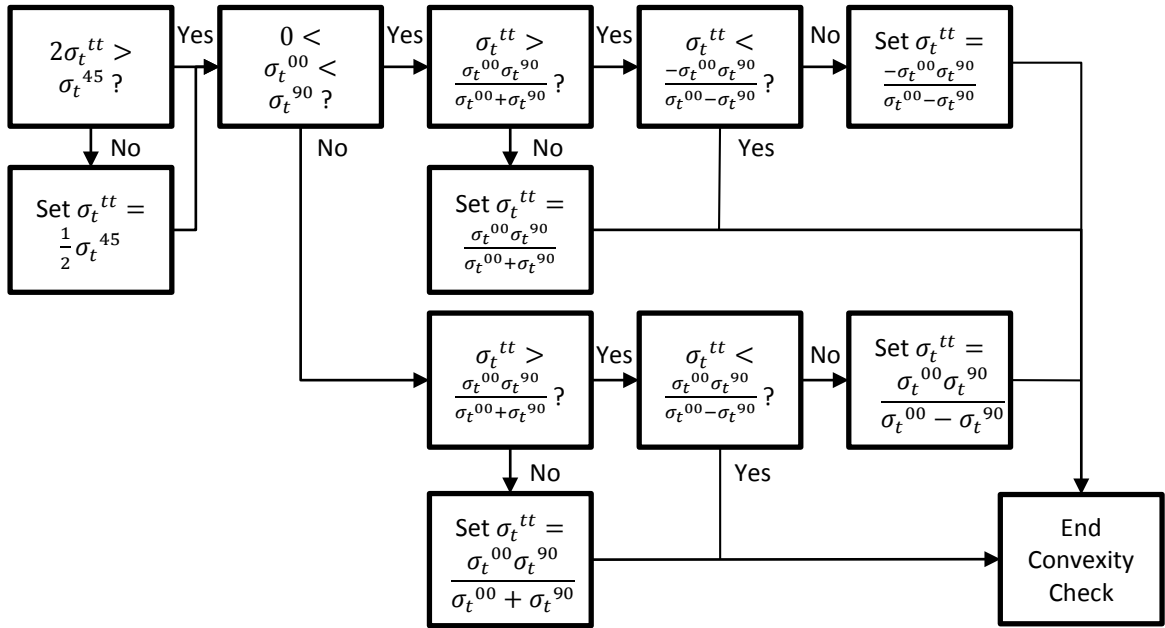


Figure 8: Convexity enforcement algorithm

3.2 – Implementation into the LS-DYNA Code

This methodology, while can be adapted into most currently existing finite element codes, is implemented into the LS-DYNA finite element code developed by the Livermore Software Technology Corporation (LSTC). This material model is written in

the FORTRAN programming language, which is compatible with the LS-DYNA code.

The starting point for the development of this material model is the previously discussed Generalized Yield Surface variant of the Tabulated Johnson-Cook material model.

To accomplish all of the intended goals of this research, specific input data must be provided by the user of the model. These inputs may consist of parameters, curves, or tables. Since this material model is being implemented into the LS-DYNA finite element code, the inputs are defined in the keyword format. Figure 9 shows the input format for this material model when used in LS-DYNA.

*MAT_TABULATED_JOHNSON_COOK_ORTHO_PLASTICITY								
\$	MID	RO	E	PR	CP	TR	BETA	NUMINT
	xxx	xxx	xxx	xxx	xxx	xxx	xxx	xxx
\$	T00R	T00T	LCF	LCG	LCH	LCI		
	xxx	xxx	xxx	xxx	xxx	xxx		
\$	C00R	C00T	S45R	S45T		SFIEPM	NITER	AOPT
	xxx	xxx	xxx	xxx		xxx	xxx	xxx
\$	T90R	T45R	TTHR	C90R	C45R	CTHR		
	xxx	xxx	xxx	xxx	xxx	xxx		
\$	T90T	T45T	TTHT	C90T	C45T	CTHT		TOL
	xxx	xxx	xxx	xxx	xxx	xxx		xxx
\$	XP	YP	ZP	A1	A2	A3	MACF	
	xxx	xxx	xxx	xxx	xxx	xxx	xxx	
\$	V1	V2	V3	D1	D2	D3	BETA	
	xxx	xxx	xxx	xxx	xxx	xxx	xxx	

Figure 9: Material input keyword format

The keyword callout for this material model is

*MAT_TABULATED_JOHNSON_COOK_ORTHO_PLASTICITY and the numerical identification for this material model is 264. Each input option is described in Table 3. More information about some of the inputs can be found in the LS-DYNA material model manual [11].

Table 3: Material model input descriptions

MID	Material identification. A unique number or label not exceeding 8 characters must be specified.
RO	Mass density.
E	Young's modulus: GT.0.0: constant value is used LT.0.0: temperature dependent Young's modulus given by load curve ID = -E
PR	Poisson's ratio.
CP	Specific heat.
TR	Room temperature.
BETA	Fraction of plastic work converted into heat.
NUMINT	Number of integration points which must fail before the element is deleted. EQ.-200: Turns off erosion for solids. Not recommended unless used in conjunction with *CONSTRAINED_TIED_NODES_FAILURE.
T00R	Table ID. The load curve ID defines tensile stress in the 0-degree direction (relative to rolling/extrusion) as a function of plastic strain. The table ID defines for each plastic strain rate value a load curve ID giving the (isothermal) stress (in the 0-degree direction) versus plastic strain for that rate.
T00T	Table ID defining for each temperature value a load curve ID giving the tensile (quasi-static) stress (in the 0-degree direction) versus plastic strain for that temperature.

LCF	Load curve ID or Table ID. The load curve ID defines plastic failure strain as a function of triaxiality. The table ID defines for each Lode parameter a load curve ID giving the plastic failure strain versus triaxiality for that Lode parameter. (Table option only for solids and not yet generally supported).
LCG	Load curve ID defining plastic failure strain as a function of plastic strain rate.
LCH	Load curve ID defining plastic failure strain as a function of temperature
LCI	Load curve ID or Table ID. The load curve ID defines plastic failure strain as a function of element size. The table ID defines for each triaxiality a load curve ID giving the plastic failure strain versus element size for that triaxiality.
C00R	Table ID. The load curve ID defines compressive stress in the 0-degree direction (relative to rolling/extrusion) as a function of plastic strain. The table ID defines for each plastic strain rate value a load curve ID giving the (isothermal) stress (in the 0-degree direction) versus plastic strain for that rate.
C00T	Table ID defining for each temperature value a load curve ID giving the compressive (quasi-static) stress (in the 0-degree direction) versus plastic strain for that temperature.
S45R	Table ID. The load curve ID defines shear stress in the 45-degree direction (relative to rolling/extrusion) as a function of plastic strain. The table ID defines for each plastic strain rate value a load curve ID giving the (isothermal) stress (in the 45-degree direction) versus plastic strain for that rate.
S45T	Table ID defining for each temperature value a load curve ID giving the shear (quasi-static) stress (in the 45-degree direction) versus plastic strain for that temperature.
SFIEPM	Scale factor on the initial estimate of the plastic multiplier.
NITER	Number of secant iterations to be performed.

AOPT	This variable is used to define the material coordinate system. See LS_DYNA User's Manual Volume II Materials MAT_002 for description of this variable and variables on cards 'Local Coordinate System Card 1 and 2'.
T90R	Table ID. The load curve ID defines tensile stress in the 90-degree direction (relative to rolling/extrusion) as a function of plastic strain. The table ID defines for each plastic strain rate value a load curve ID giving the (isothermal) stress (in the 90-degree direction) versus plastic strain for that rate.
T45R	Table ID. The load curve ID defines tensile stress in the 45-degree direction (relative to rolling/extrusion) as a function of plastic strain. The table ID defines for each plastic strain rate value a load curve ID giving the (isothermal) stress (in the 45-degree direction) versus plastic strain for that rate.
TTHR	Table ID. The load curve ID defines tensile stress in the thickness direction (relative to rolling/extrusion) as a function of plastic strain. The table ID defines for each plastic strain rate value a load curve ID giving the (isothermal) stress (in the thickness direction) versus plastic strain for that rate.
C90R	Table ID. The load curve ID defines compressive stress in the 90-degree direction (relative to rolling/extrusion) as a function of plastic strain. The table ID defines for each plastic strain rate value a load curve ID giving the (isothermal) stress (in the 90-degree direction) versus plastic strain for that rate.
C45R	Table ID. The load curve ID defines compressive stress in the 45-degree direction (relative to rolling/extrusion) as a function of plastic strain. The table ID defines for each plastic strain rate value a load curve ID giving the (isothermal) stress (in the 45-degree direction) versus plastic strain for that rate.
CTHR	Table ID. The load curve ID defines compressive stress in the thickness direction (relative to rolling/extrusion) as a function of plastic strain. The table ID defines for each plastic strain rate value a load curve ID giving the (isothermal) stress (in the thickness direction) versus plastic strain for that rate.

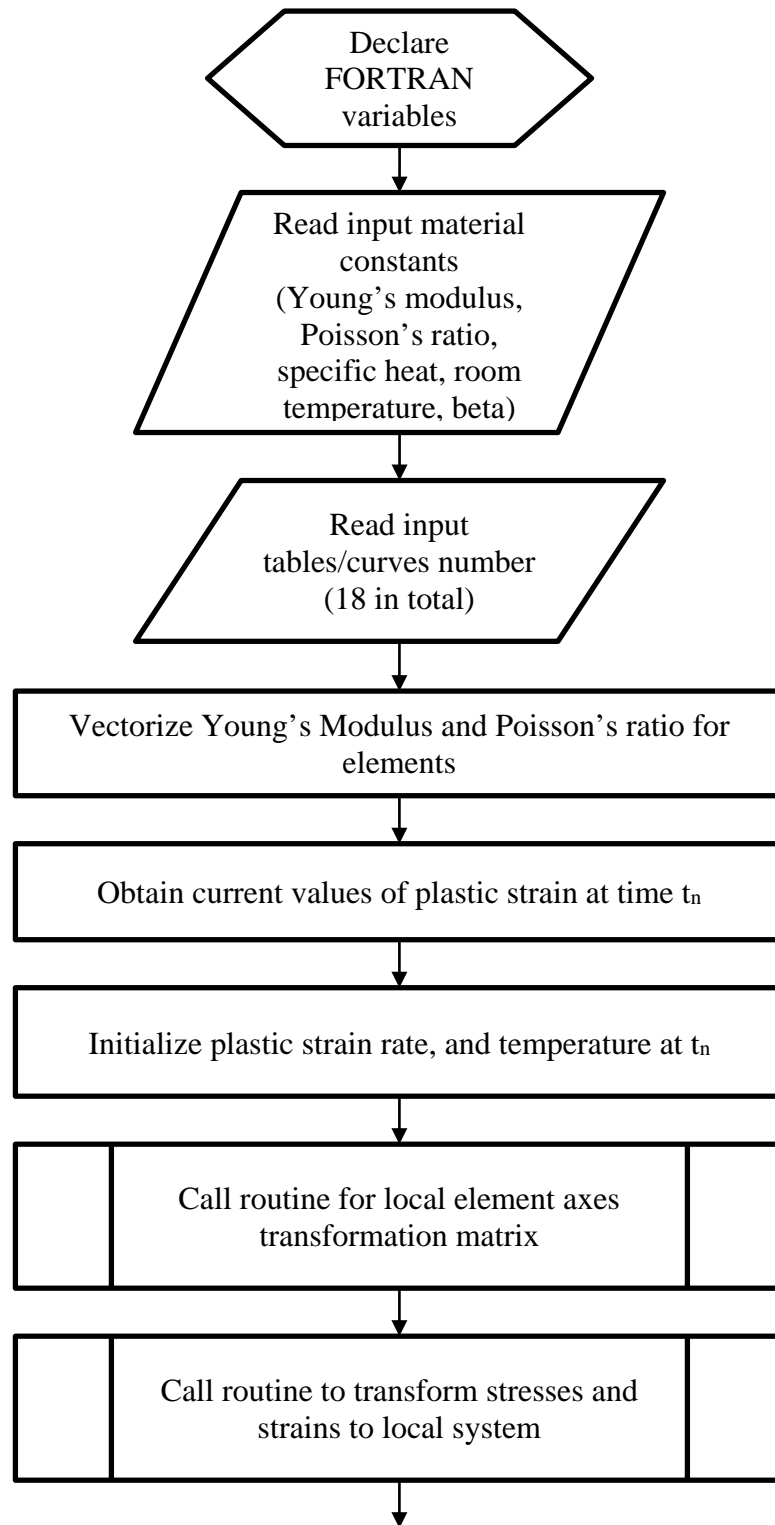
T90T	Table ID defining for each temperature value a load curve ID giving the tensile (quasi-static) stress (in the 90-degree direction) versus plastic strain for that temperature.
T45T	Table ID defining for each temperature value a load curve ID giving the tensile (quasi-static) stress (in the 45-degree direction) versus plastic strain for that temperature.
TTHT	Table ID defining for each temperature value a load curve ID giving the tensile (quasi-static) stress (in the thickness direction) versus plastic strain for that temperature.
C90T	Table ID defining for each temperature value a load curve ID giving the compressive (quasi-static) stress (in the 90-degree direction) versus plastic strain for that temperature.
C45T	Table ID defining for each temperature value a load curve ID giving the compressive (quasi-static) stress (in the 45-degree direction) versus plastic strain for that temperature.
CTHT	Table ID defining for each temperature value a load curve ID giving the compressive (quasi-static) stress (in the thickness direction) versus plastic strain for that temperature.
TOL	Convergence tolerance for plasticity algorithm
XP, YP, ZP	Define coordinates of point p for AOPT = 1 and 4.
A1, A2, A3	Define components of vector a for AOPT = 2.
MACF	Material axes change flag for brick elements: EQ.1: No change, default, EQ.2: switch material axes <i>a</i> and <i>b</i> , EQ.3: switch material axes <i>a</i> and <i>c</i> , EQ.4: switch material axes <i>b</i> and <i>c</i> .

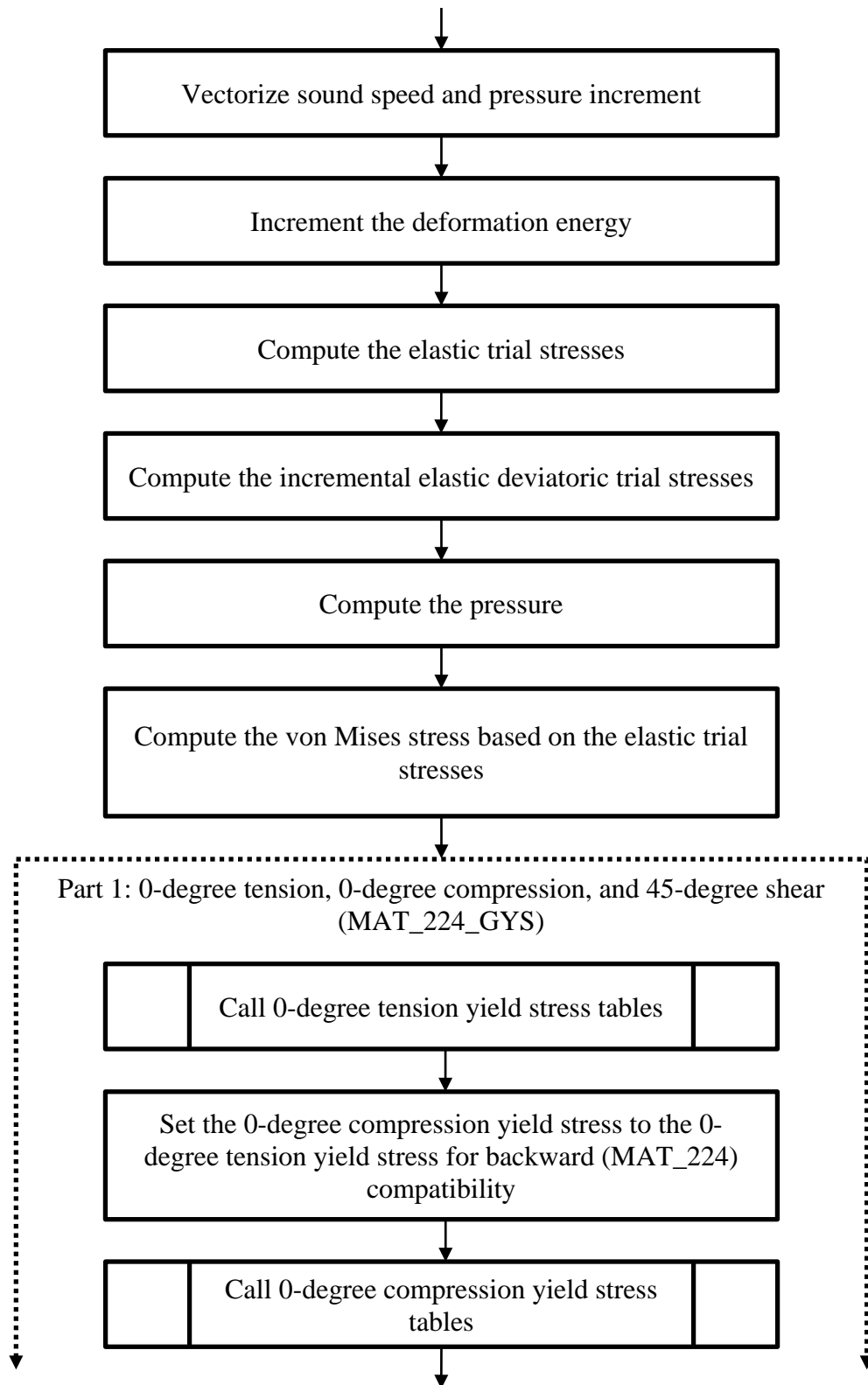
V1, V2, V3	Define components of vector v for AOPT = 3 and 4.
D1, D2, D3	Define components of vector d for AOPT = 2.
BETA	Material angle in degrees for AOPT = 3, may be overridden on the element card, see *ELEMENT_SHELL_BETA or *ELEMENT_SOLID_ORTHO.

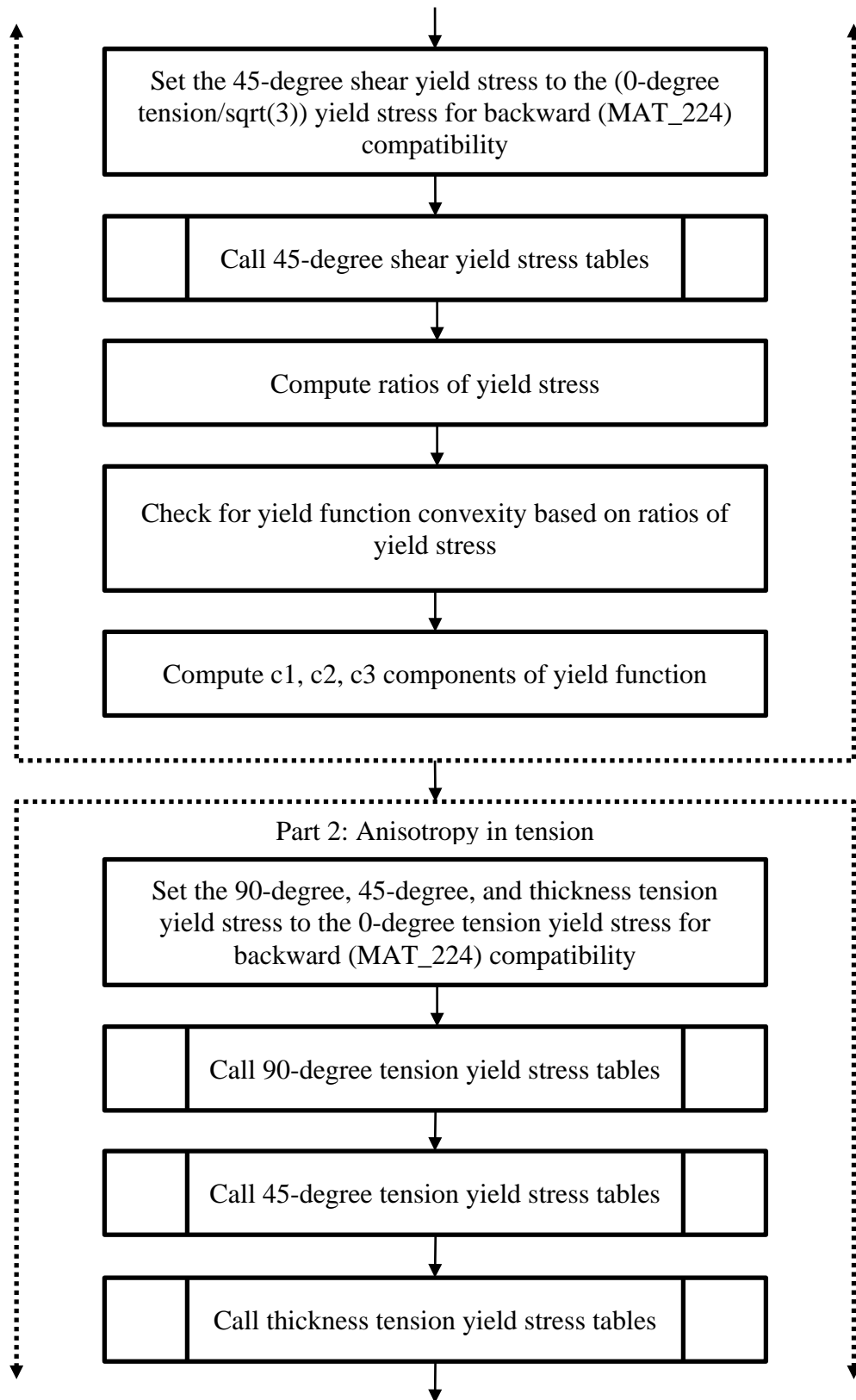
3.2.1 – Source Code Overview

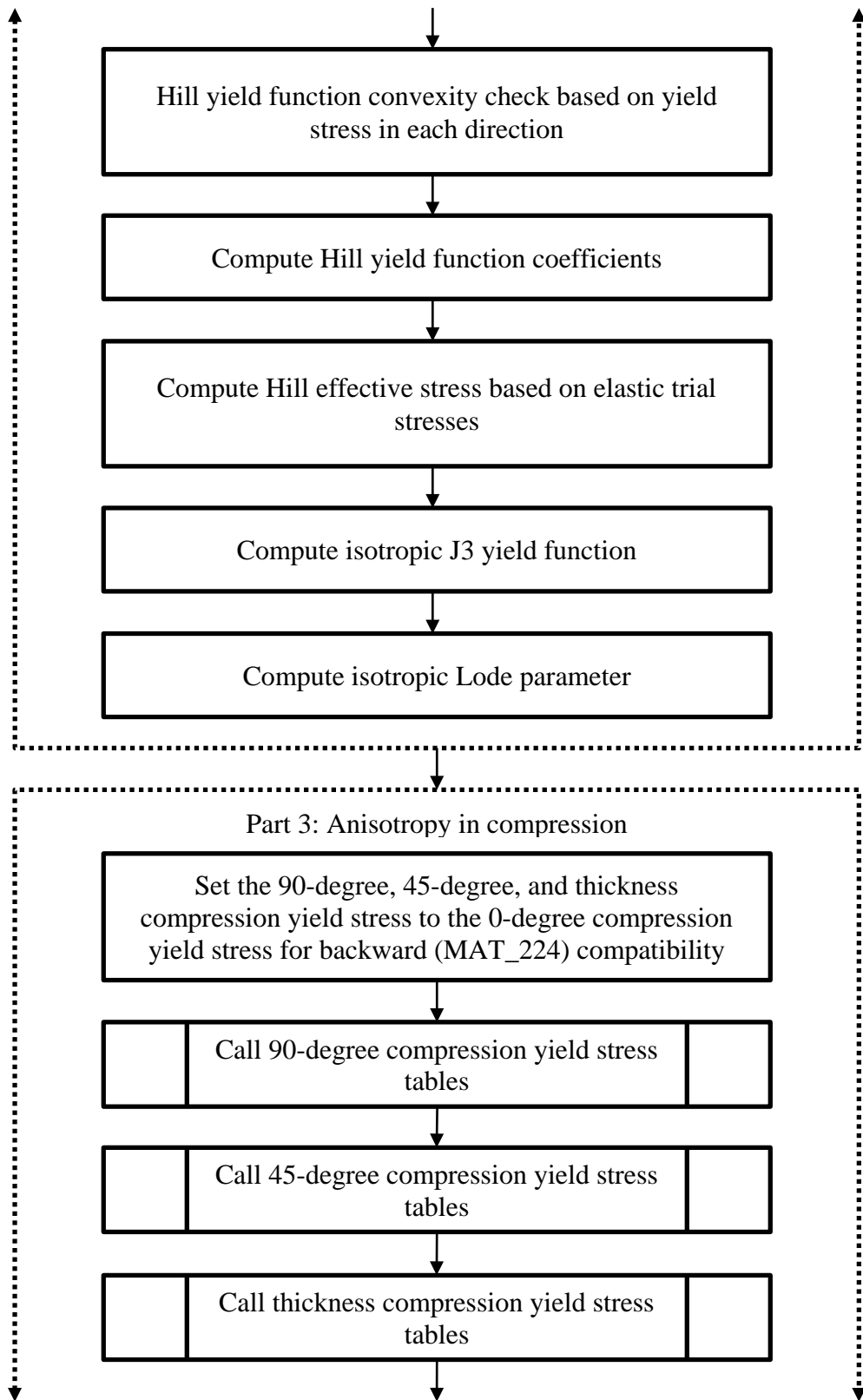
This section provides a full overview of the material subroutine portion of the finite element code. This routine can be called by the user using the appropriate keyword.

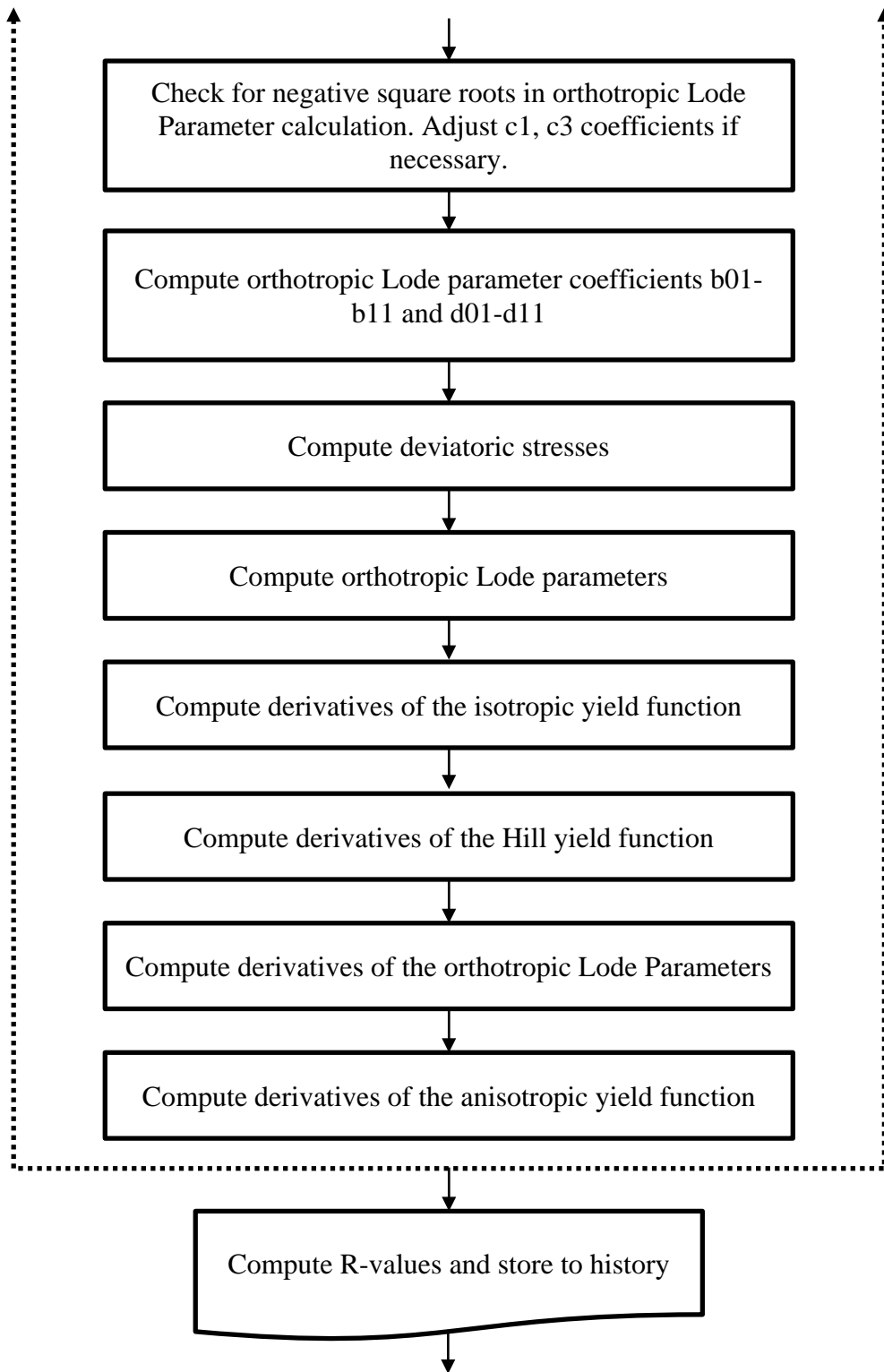
Figure 10: Material model routine flow chart

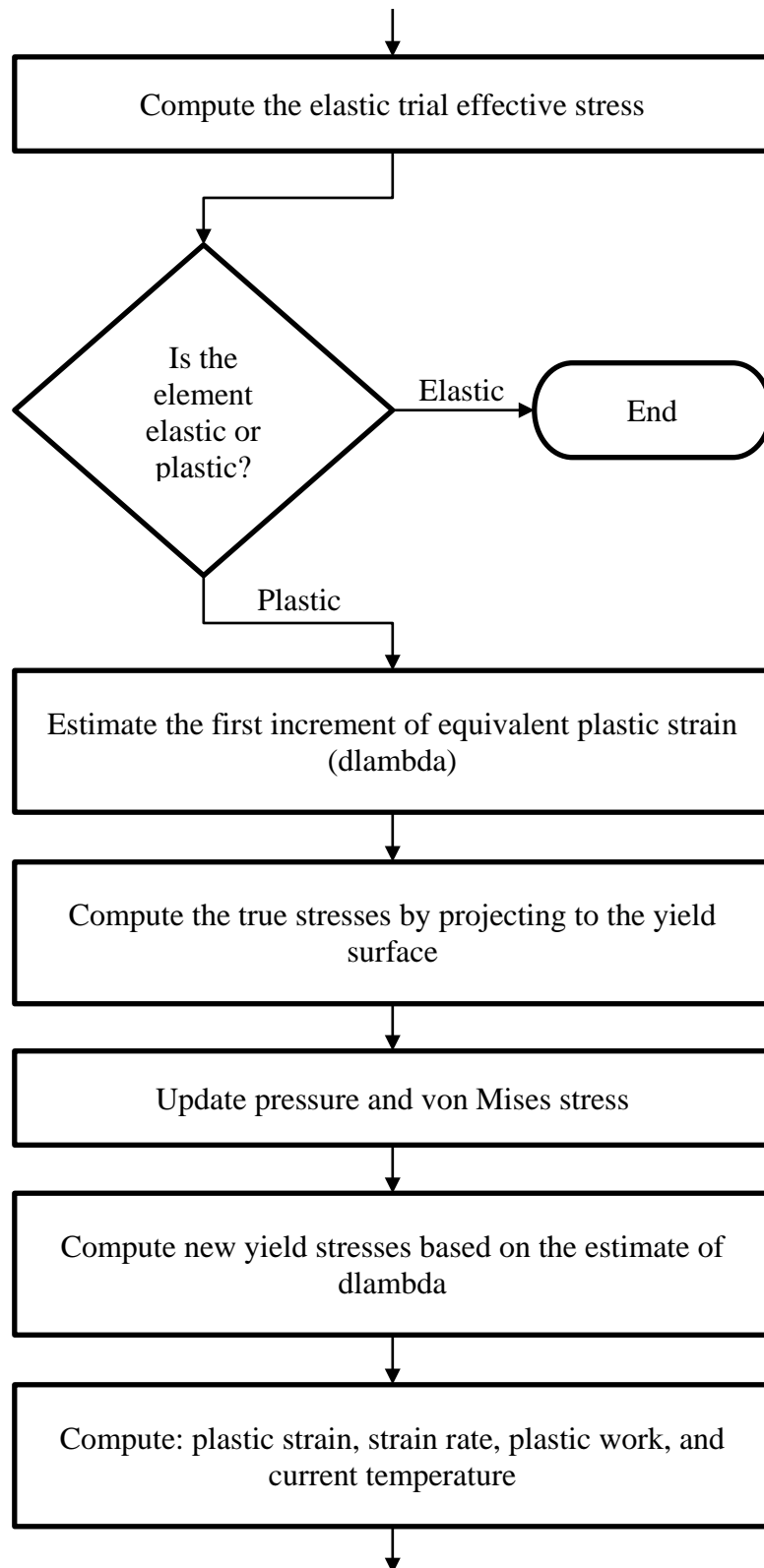


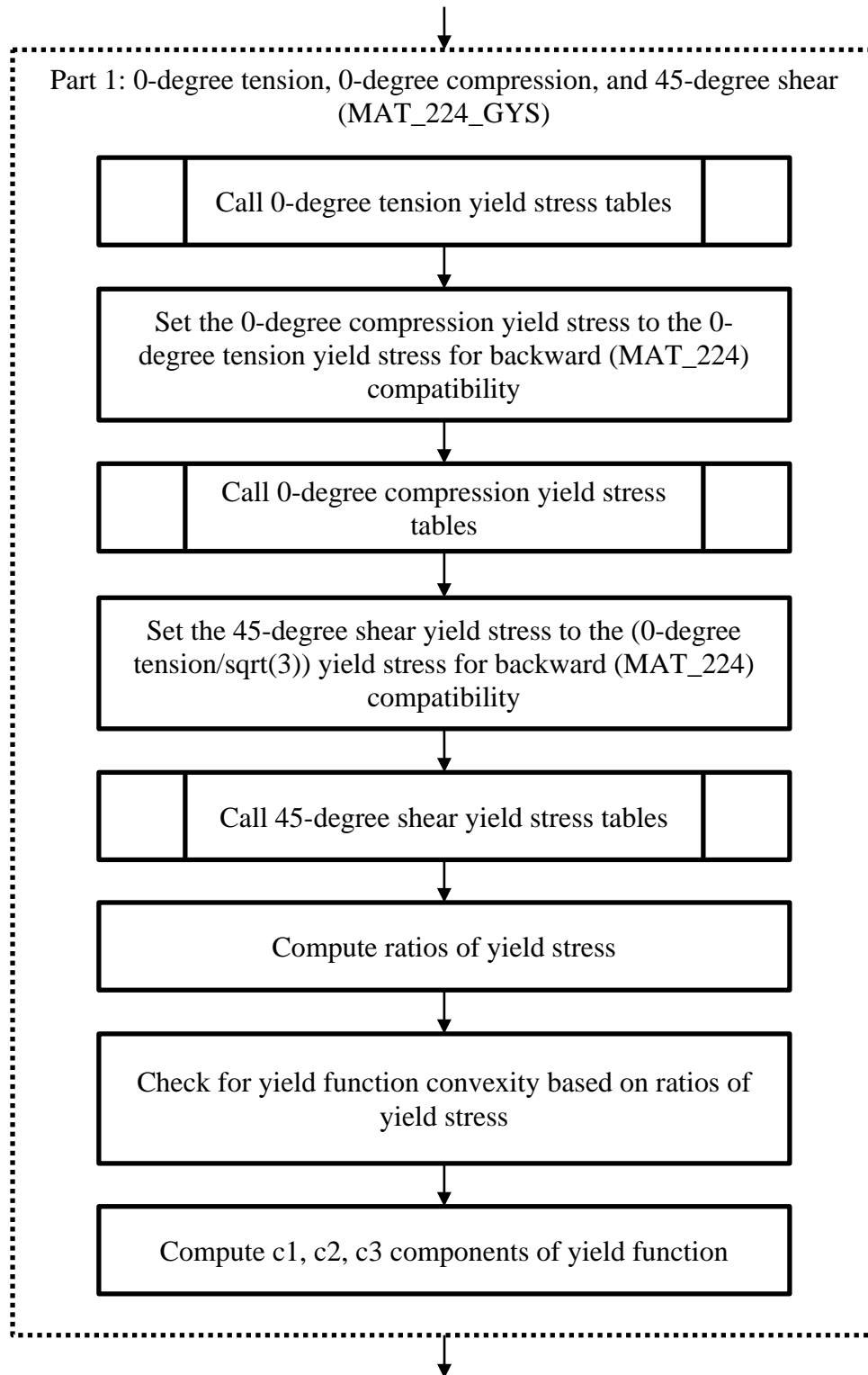


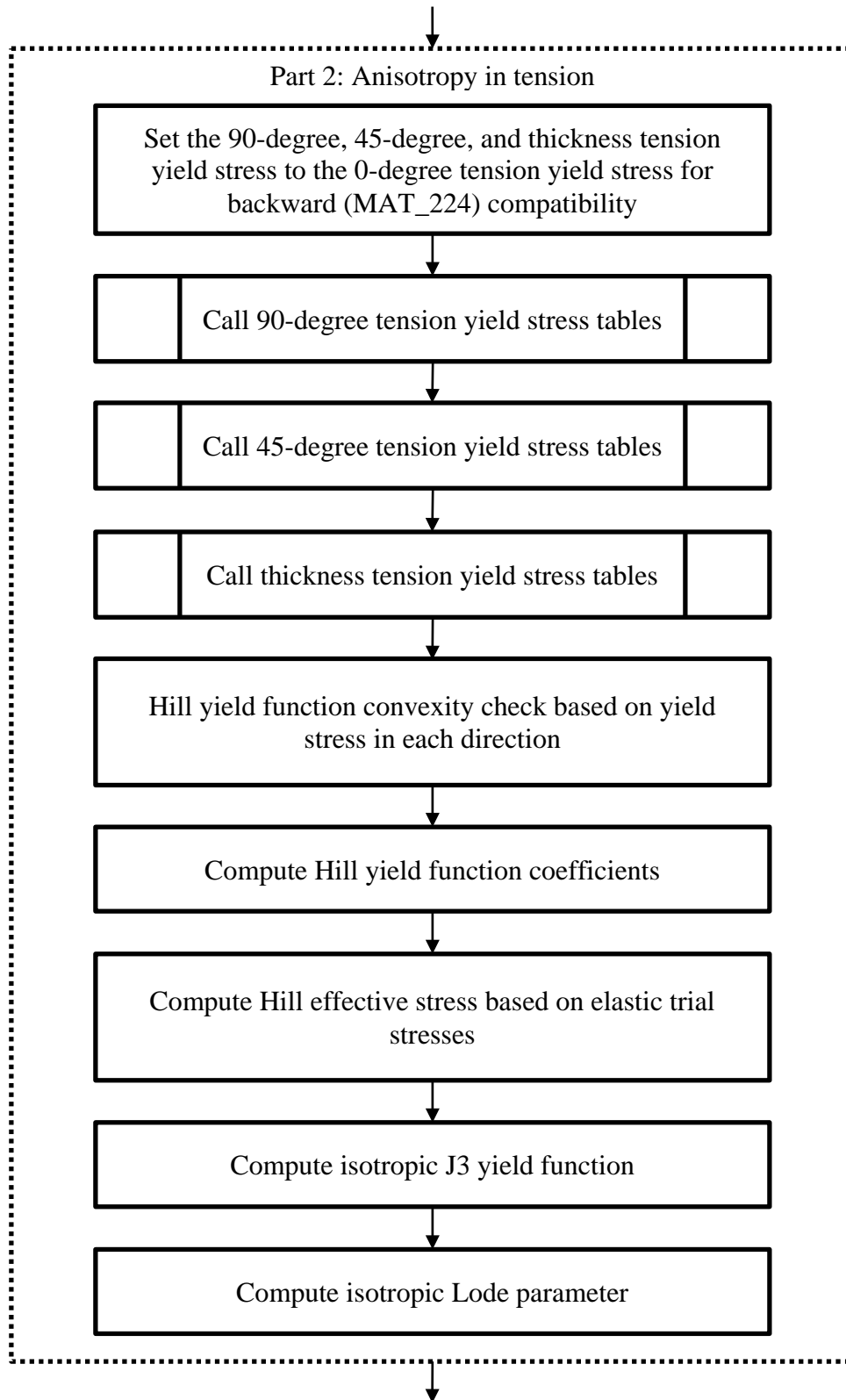


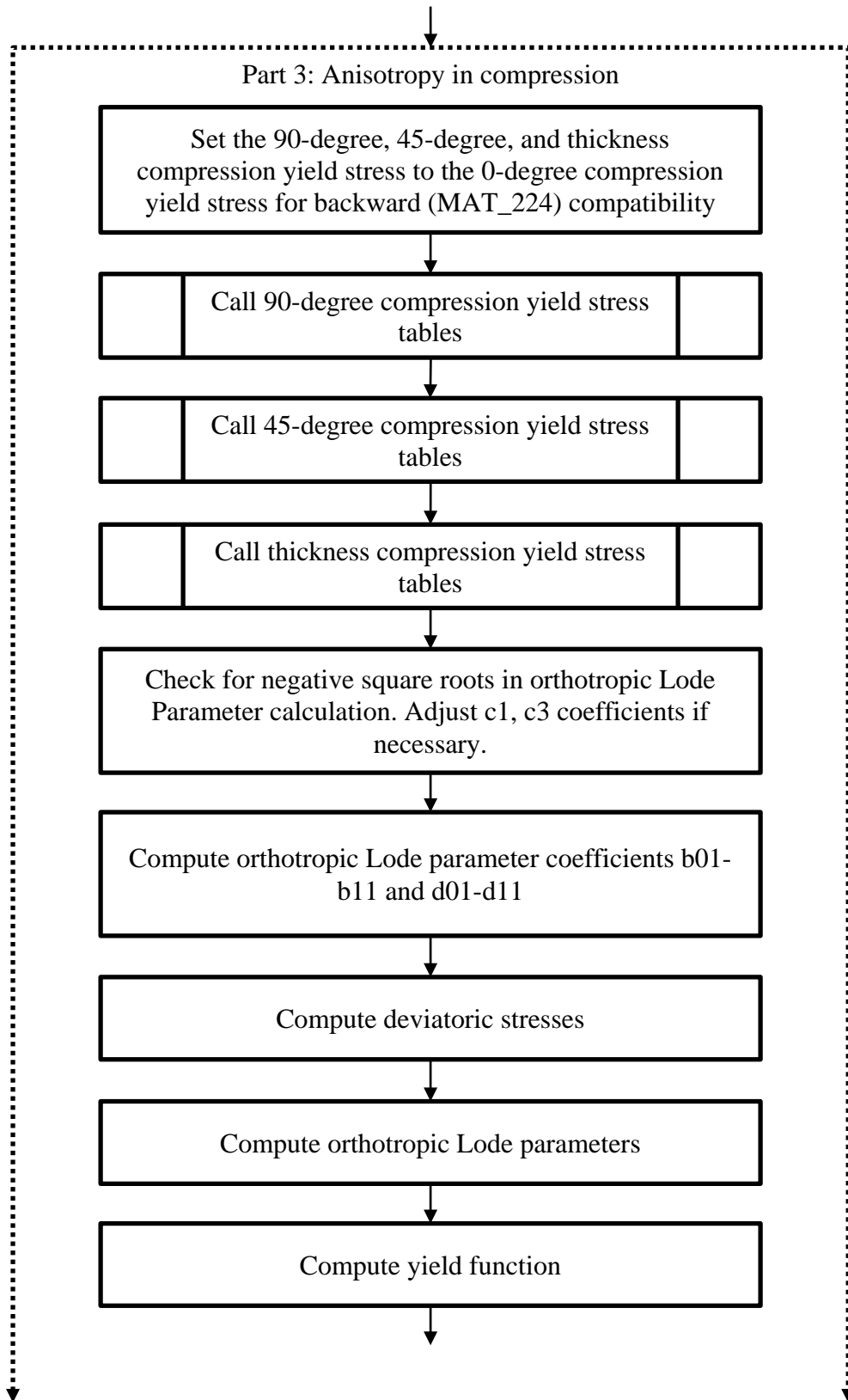


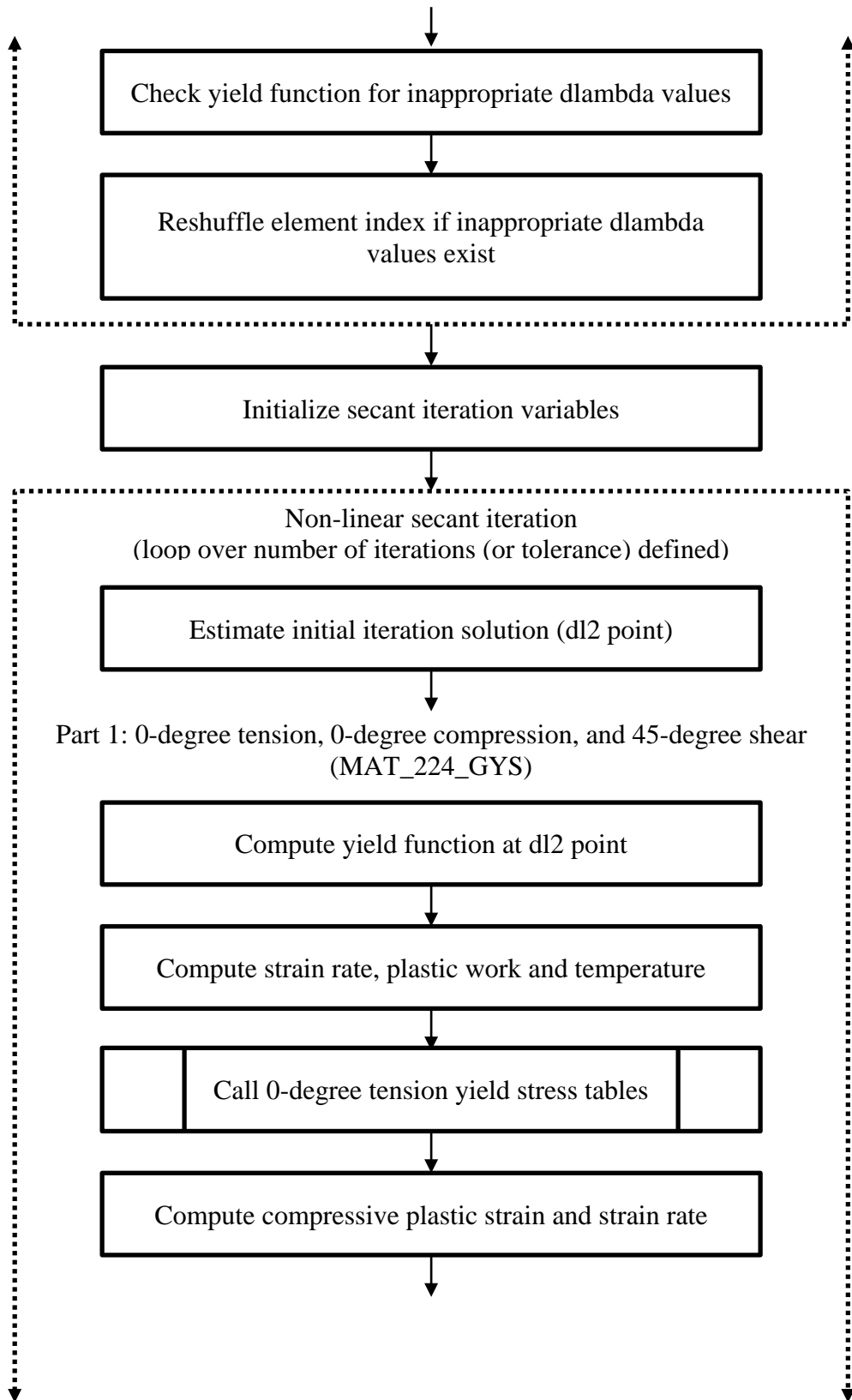


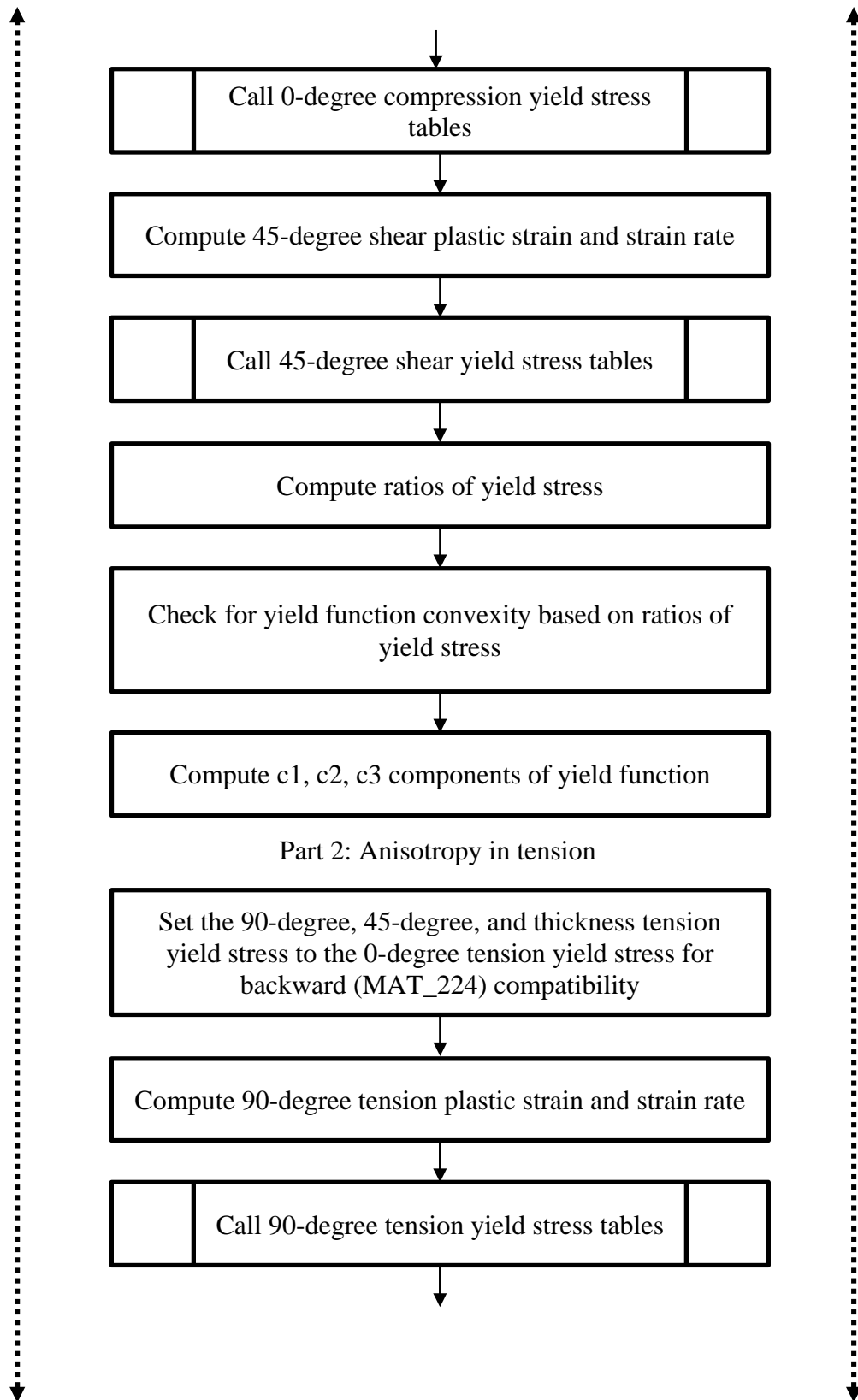


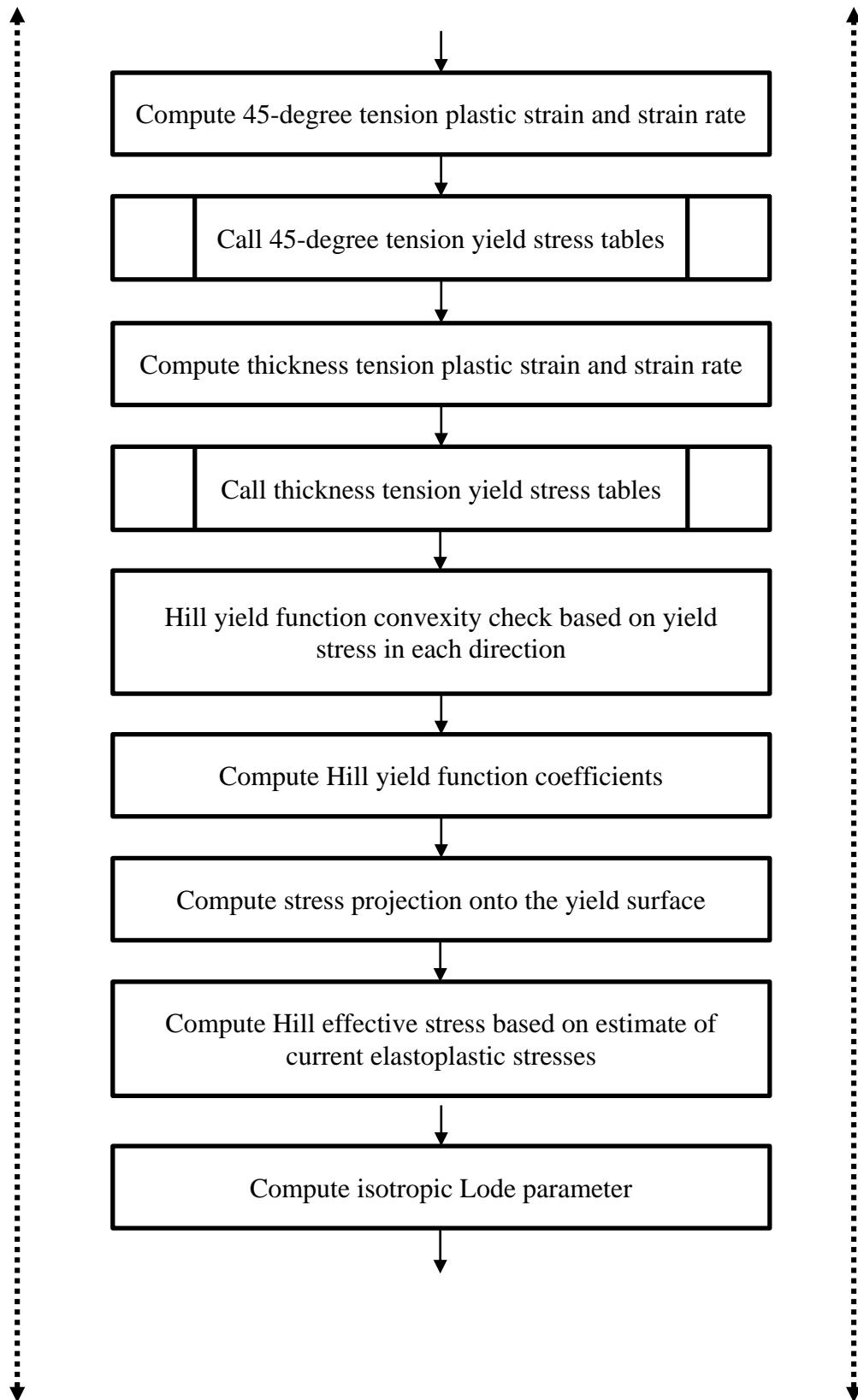


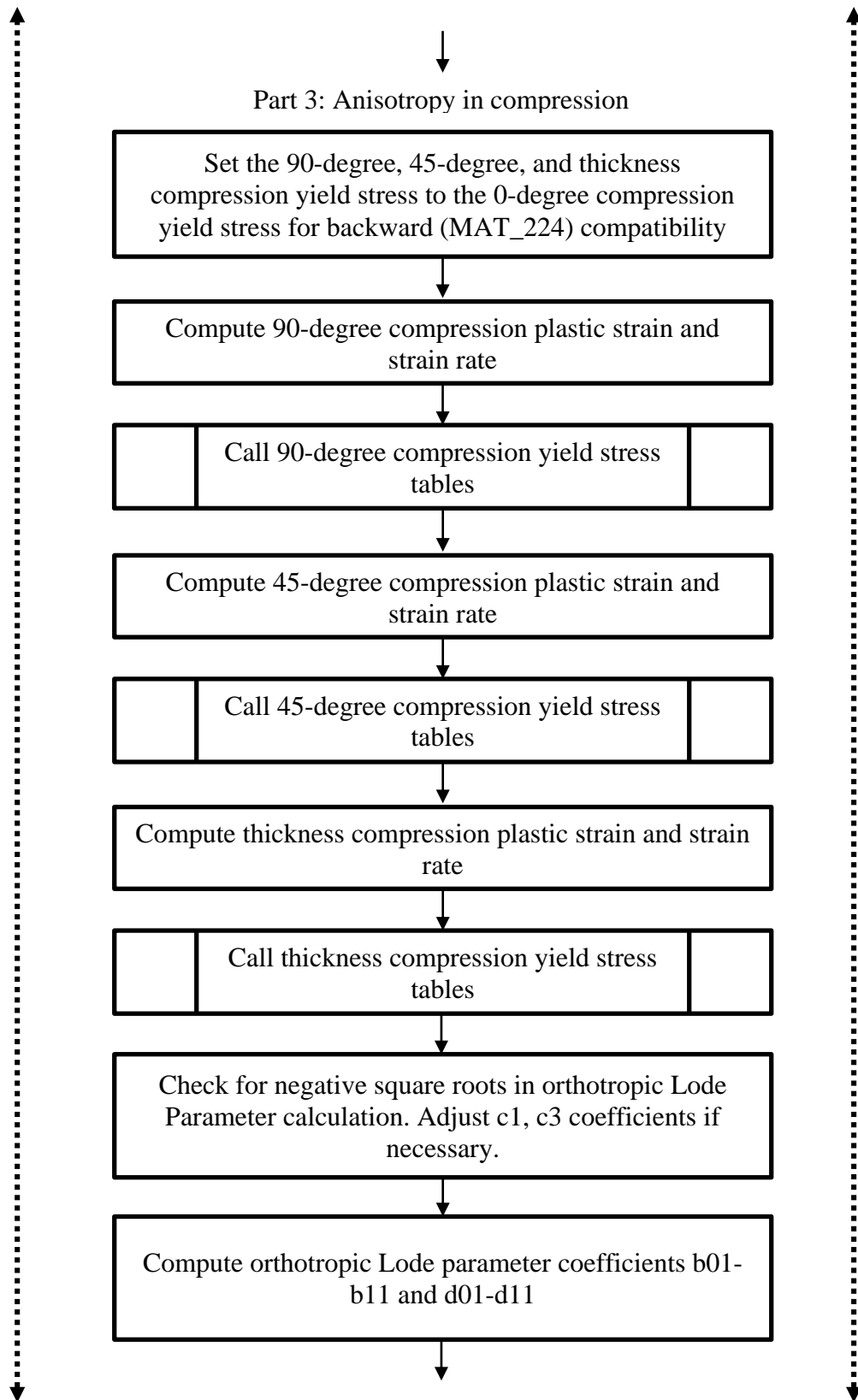


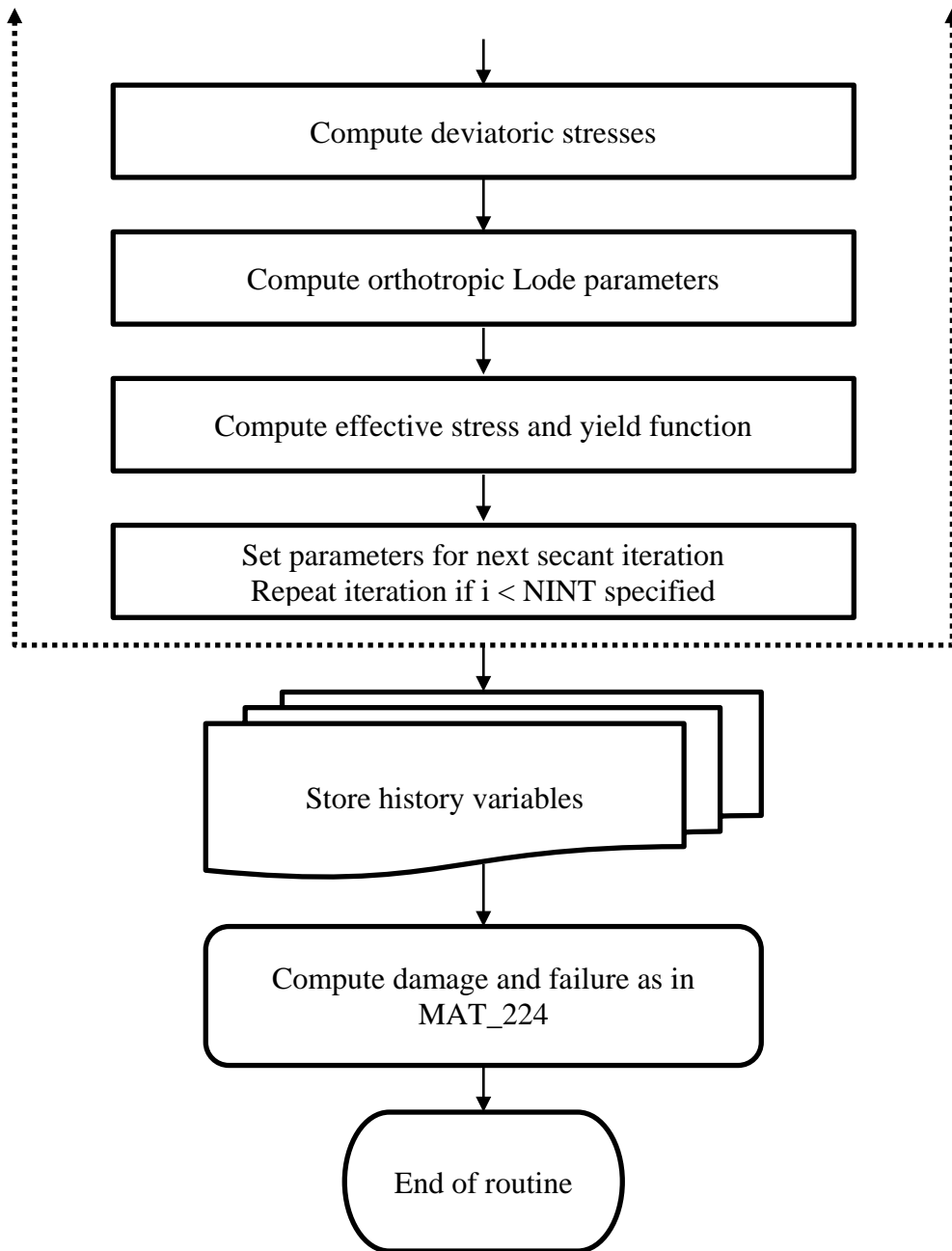












3.2.2 – Single Element Verification

To verify this material model, a set of single element simulations are conducted. The benefit of single element simulations is that in uniaxial tension and compression, the resulting stress as a function of equivalent plastic strain should be equal to the input yield curves due to the uniformity of the strain and stress fields. While this method does not fully test the computational robustness of the model, it does provide a critical verification step.

The initial single element simulation set was to verify that the model is backwards compatible with previously existing isotropic models. To test the hypothesis that this model is backward compatible, single elements are simulated with this new material model on a virtual test bed next to a set of elements simulated with the Generalized Yield Surface model.

In total, 10 elements were created and placed in the array shown in Figure 11. A prescribed tensile displacement was applied to the first row of five elements in the set and a prescribed compressive displacement was applied to the second row of elements. The first column, red elements, is modeled using the anisotropic material model with the material axis in the 0-degree direction. This means that the rolling direction is in the same direction as the tensile or compressive displacements. The second column, green elements, is modeled with the anisotropic material model in the 45-degree direction. The third column, blue elements, is modeled with the anisotropic material model in the 90-degree direction. The fourth column, gold elements, is modeled with the anisotropic

material model in the thickness direction. Lastly, the fifth column, brown elements, is modeled using the isotropic Generalized Yield Surface material model.

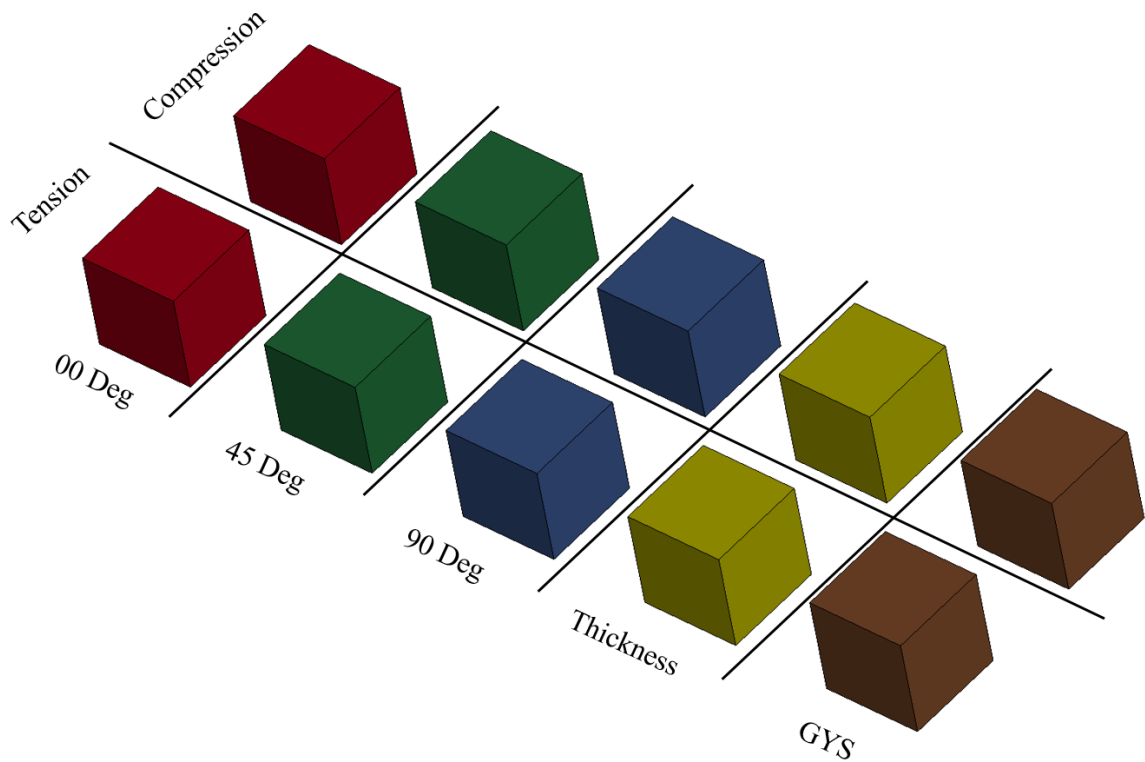


Figure 11: Isotropic single element verification

The keyword input for the Generalized Yield Surface elements (brown) are shown in Figure 12. The keyword input for the anisotropic material model elements are shown in Figure 13. For these elements, the only difference between each of the directional elements are the values of the material axis vectors.

*MAT_TABULATED_JOHNSON_COOK_GYS								
\$	MID	RO	E	PR	CP	TR	BETA	NUMINT
	9	2.7E-6	74.66	0.3	8.75E+2	300	1E-10	0.0
\$	LCK1	LCKT	LCF	LCG	LCH	LCI		
	100							
\$	LCCR	LCCT	LCSR	LCST	IFLAG	SFIEPM	NITER	
	200		300			2	10	

Figure 12: Isotropic Generalized Yield Surface input

*MAT_TABULATED_JOHNSON_COOK_ORTHO_PLASTICITY								
\$	MID	RO	E	PR	CP	TR	BETA	NUMINT
	1	2.7E-6	74.66	0.3	8.75E+2	300	1E-10	0.0
\$	T00R	T00T	LCF	LCG	LCH	LCI		
	100							
\$	C00R	C00T	S45R	S45T		SFIEPM	NITER	AOPT
	200		300			2	10	2
\$	T90R	T45R	TTHR	C90R	C45R	CTHR		
	100	100	100	200	200	200		
\$	T90T	T45T	TTHT	C90T	C45T	CTHT		
\$	XP	YP	ZP	A1	A2	A3	MACF	
				0.0	0.0	1.0		
\$	V1	V2	V3	D1	D2	D3	BETA	
				0.0	-1.0	0.0		

Figure 13: Isotropic implementation of the anisotropic material model

The results of this simulation can be seen graphically in Figure 14 and Figure 15. Figure 14 shows the longitudinal stress of each element at a specific displacement. At this particular displacement, the tensile stress is about 1.3 GPa and the compressive stress is about 1.4 GPa. Figure 15 shows the longitudinal stress of each element as a function of plastic strain along with the input yield curves for tension (red) and compression (blue).

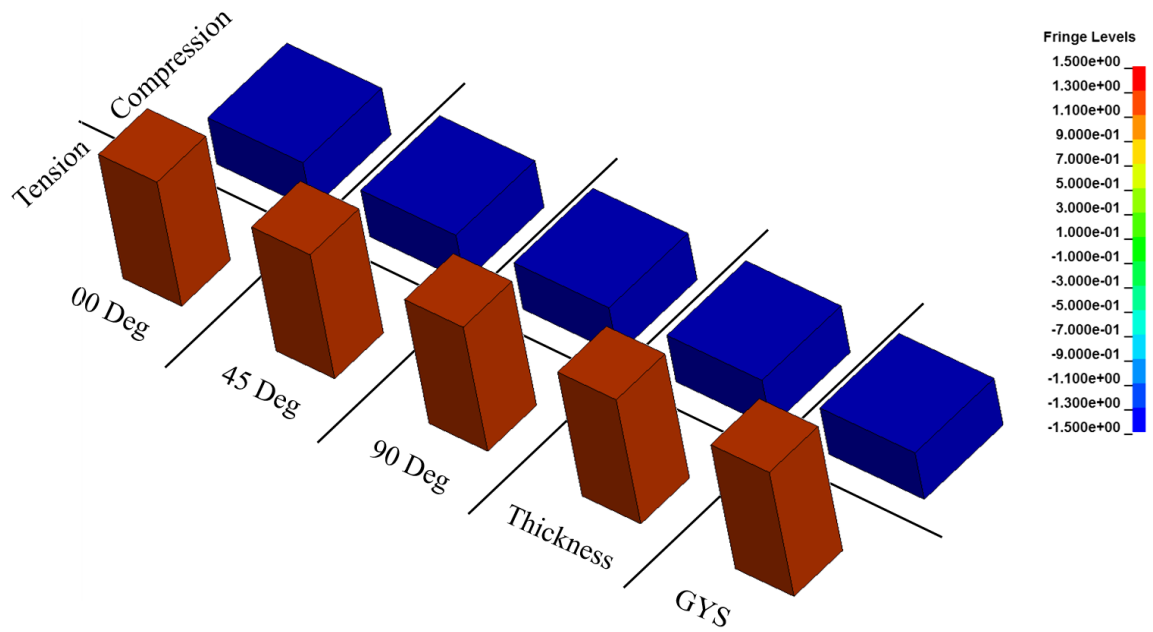


Figure 14: Isotropic single element verification simulation longitudinal stress

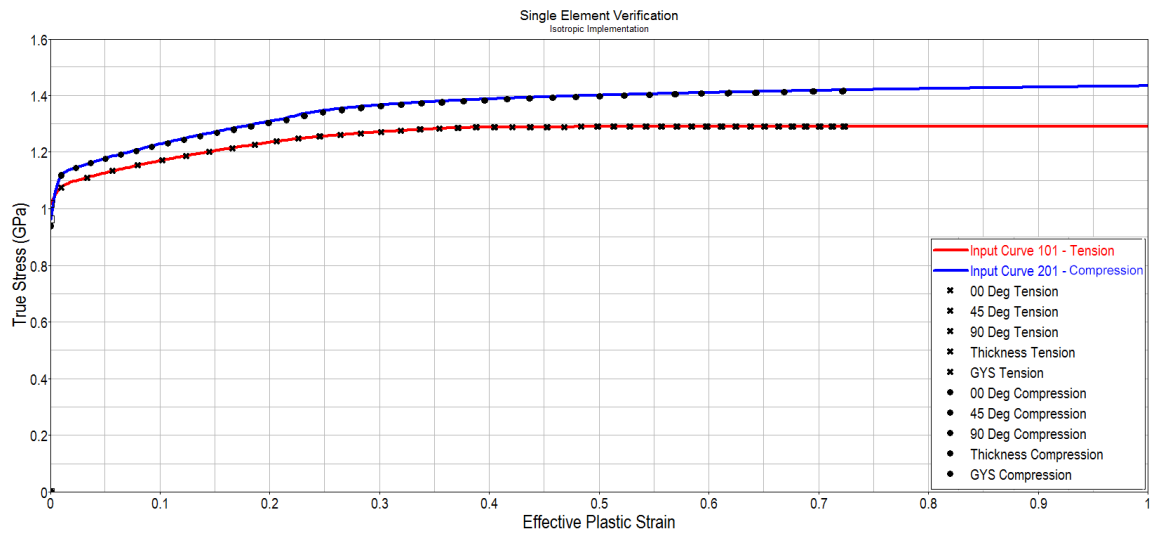


Figure 15: Isotropic single element verification simulation results

These simulation results show that the isotropic implementation of this new anisotropic model does replicate a previously developed isotropic asymmetric model. It is

important to note that all of the directional elements have the same stress values as the Generalized Yield Surface elements. This result is expected because all of the directional tension and compression inputs are all referencing the same input yield curve. Since the simulation results and the input yield curves are equal for both tension and compression, this shows that the tabulated input component of this new material model are appropriately reading the input curves.

The second single element simulation is used to verify this anisotropic material model with different yield curves in each direction. The purpose of this simulation is to determine if each element, in each direction, results in a flow stress equal to the input yield curve for that direction. To accomplish this, input yield curves are varied in each direction and those curves are referenced in the material keyword format (Figure 16).

*MAT_TABULATED_JOHNSON_COOK_ORTHO_PLASTICITY								
\$	MID	RO	E	PR	CP	TR	BETA	NUMINT
	1	2.7E-6	74.66	0.3	8.75E+2	300	1E-10	0.0
\$	T00R	T00T	LCF	LCG	LCH	LCI		
	100							
\$	C00R	C00T	S45R	S45T		SFIEPM	NITER	AOPT
	200		300			2	10	2
\$	T90R	T45R	TTHR	C90R	C45R	CTHR		
	400	500	600	700	800	900		
\$	T90T	T45T	TTHT	C90T	C45T	CTHT		
\$	XP	YP	ZP	A1	A2	A3	MACF	
				0.0	0.0	1.0		
\$	V1	V2	V3	D1	D2	D3	BETA	
				0.0	-1.0	0.0		

Figure 16: Anisotropic material model input

This simulation is set up similarly to the isotropic single element verification simulation. Figure 17 shows a simulation with eight anisotropic elements, four in tension

and four in compression. The first row of elements undergo a prescribed displacement in tension while the second row of elements undergo a prescribed displacement in compression. The first column (red) are elements with material axis defined so that the 0-degree direction is in the same direction as the tensile or compressive displacement. The second column (green) are 45-degree elements, the third column (blue) are 90-degree elements and the last column (gold) are elements through the thickness.

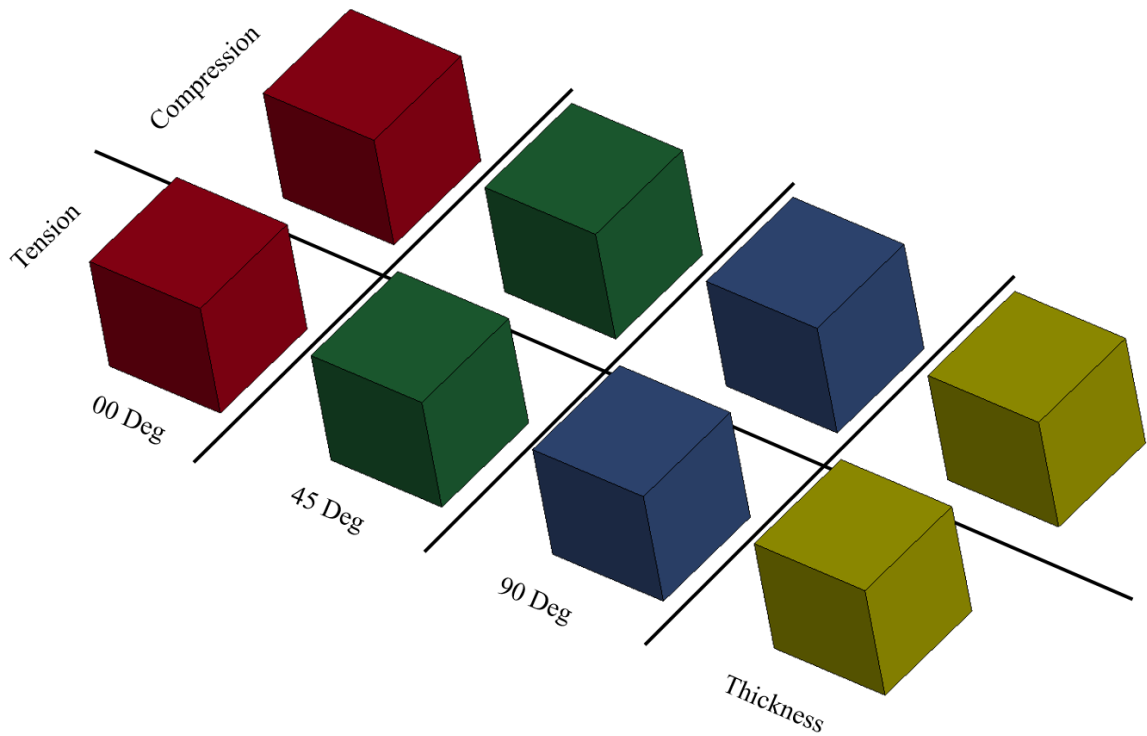


Figure 17: Anisotropic single element verification

The results of this simulation can be seen in Figure 18 and Figure 19. Figure 18 shows the longitudinal stress in each element at a specific point in time. Since every

material direction has a different specified yield curve in the input keyword, it is expected that the stress in each element would result in a different value. This result is verified in this simulation in that each element exhibits a unique stress value at this time in the simulation. Figure 19 shows the input yield curve as a function of plastic strain with the resulting elemental stress as a function of plastic strain. This plot is created for each element in the simulation, both in tension and compression. Not only does the stress in each element vary during the simulation, the result for each element is equal to the input yield curve. This result verifies that this model is both anisotropic, asymmetric and can match the input yield curve data at all strains.

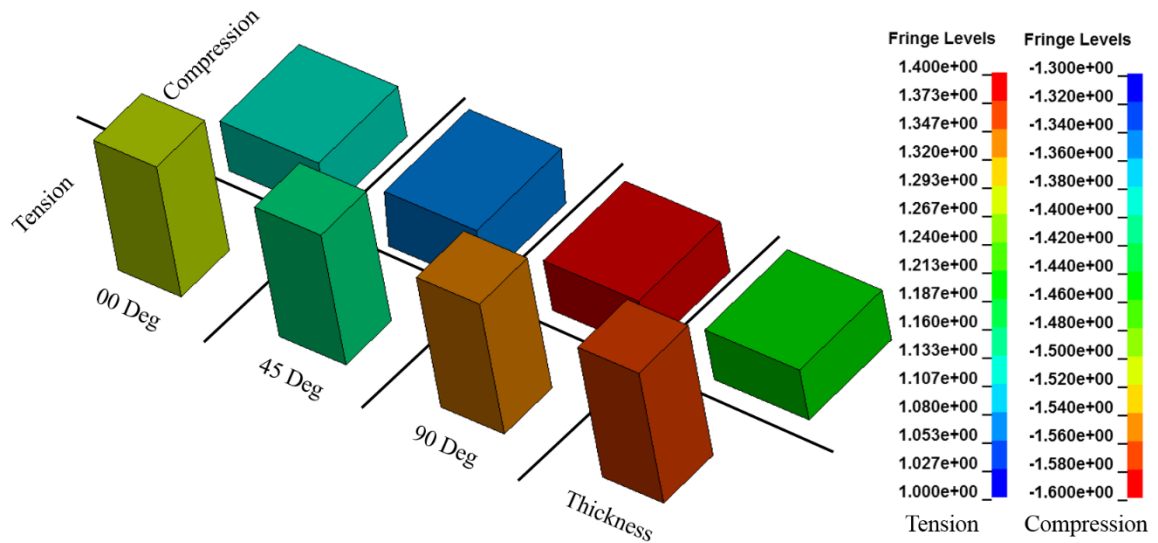


Figure 18: Anisotropic single element verification simulation longitudinal stress

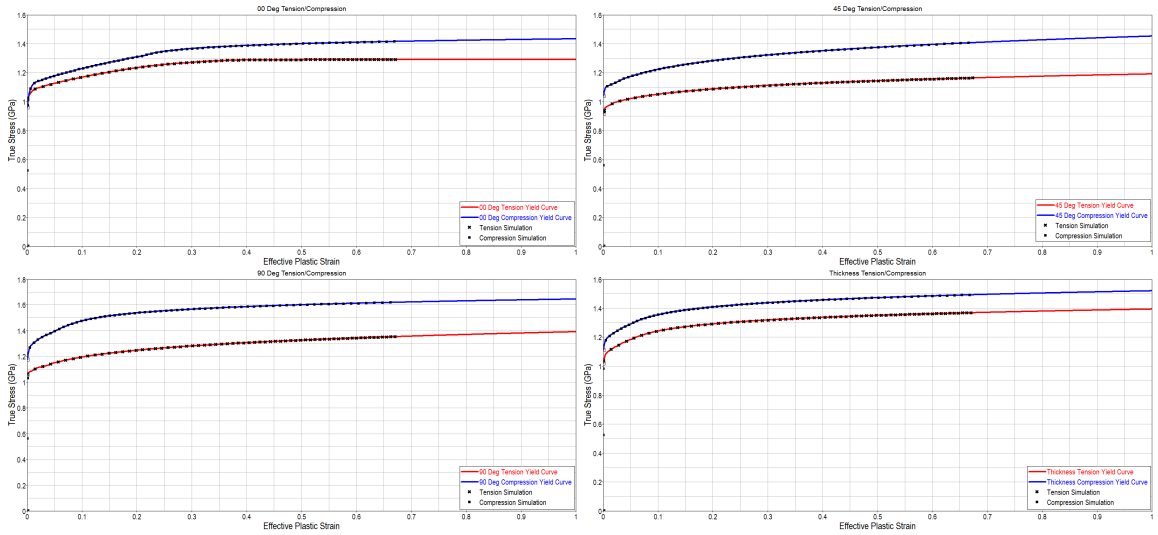


Figure 19: Anisotropic single element simulation results

The third single element verification simulation is to verify the strain rate dependency portion of this material model. To accomplish this, four unique simulations are designed so that the strain rate for each element can be varied at a constant rate. The overall set up for this simulation set is similar to the anisotropic single element verifications previously discussed. There are two rows of elements: one in tension and one in compression. There are also four columns of elements, one in each material direction. To implement strain rate dependency in the material input keyword, tables were used with varying strain rates as the abscissa.

```

*MAT_TABULATED_JOHNSON_COOK_ORTHO_PLASTICITY
$      MID      RO      E      PR      CP      TR      BETA      NUMINT
      1      2.7E-6      74.66      0.3      8.75E+2      300      1E-10      0.0
$      T00R      T00T      LCF      LCG      LCH      LCI
      100
$      C00R      C00T      S45R      S45T      SFIEPM      NITER      AOPT
      200      300      2      200      2
$      T90R      T45R      TTHR      C90R      C45R      CTHR
      400      500      600      700      800      900
$      T90T      T45T      TTHT      C90T      C45T      CTHT

$      XP      YP      ZP      A1      A2      A3      MACF
      0.0      0.0      1.0
$      V1      V2      V3      D1      D2      D3      BETA
      0.0      -1.0      0.0

*DEFINE_TABLE
$ 0-degree Tension Rate Table
$#      TBID
      100
$#      STRAIN RATE      LCID
      0.0000000      101
      0.0010000      102
      0.0100000      103
      0.1000000      104
      0.5000000      105
      1.0000000      106

```

Figure 20: Anisotropic and strain rate dependent material model input

Figure 20 shows the input used for the 0-degree element and an example table used for the 0-degree tension input. The table referenced in the T00R input position references multiple yield curves at specific strain rates. The strain rates for these yield curves are: 0.0 /ms (quasistatic), 0.001 /ms, 0.010 /ms, 0.100 /ms, 0.500 /ms and 1.000 /ms. To assure that the high strain rates are not extrapolated, the 1.000 /ms yield curves are equal to the 0.500 /ms curves. Each of the yield curves at each strain rate and material directions are scaled by scale factors. These scale factors are applied to the original quasistatic input yield curve at each point. This results in a table of yield curves with increasing yield stress as strain rate increases.

Table 4: Single element strain rate yield curve scale factors

Strain Rate	Scale Factor
0.000	1.00
0.001	1.05
0.010	1.10
0.100	1.15
0.500	1.20
1.0	1.20

In order to verify that the flow stress of the element is equal to the input yield curve, for a given strain rate, is to impose a nodal velocity that results in a specific strain rate. To accomplish this, prescribed velocities are generated that would result in strain rates of: 0.001 /ms, 0.01 /ms, 0.100 /ms and 0.500 /ms. Each of these prescribed velocities are shown in Figure 21.

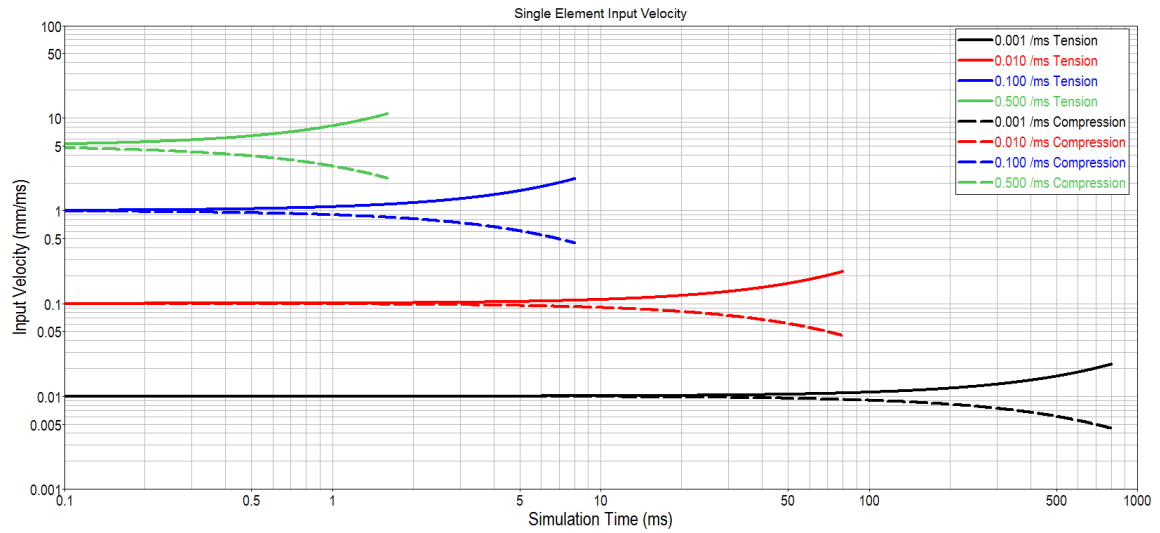


Figure 21: Single element input velocities for strain rate verification

After each simulation was completed, the resulting stress vs. plastic strain is plotted against the original input yield curves. Figure 22 shows these results for each material direction. The solid lines are the input yield curves at varying strain rates. The symbols represent the resulting stress vs. strain for each simulation, at a given strain rate.

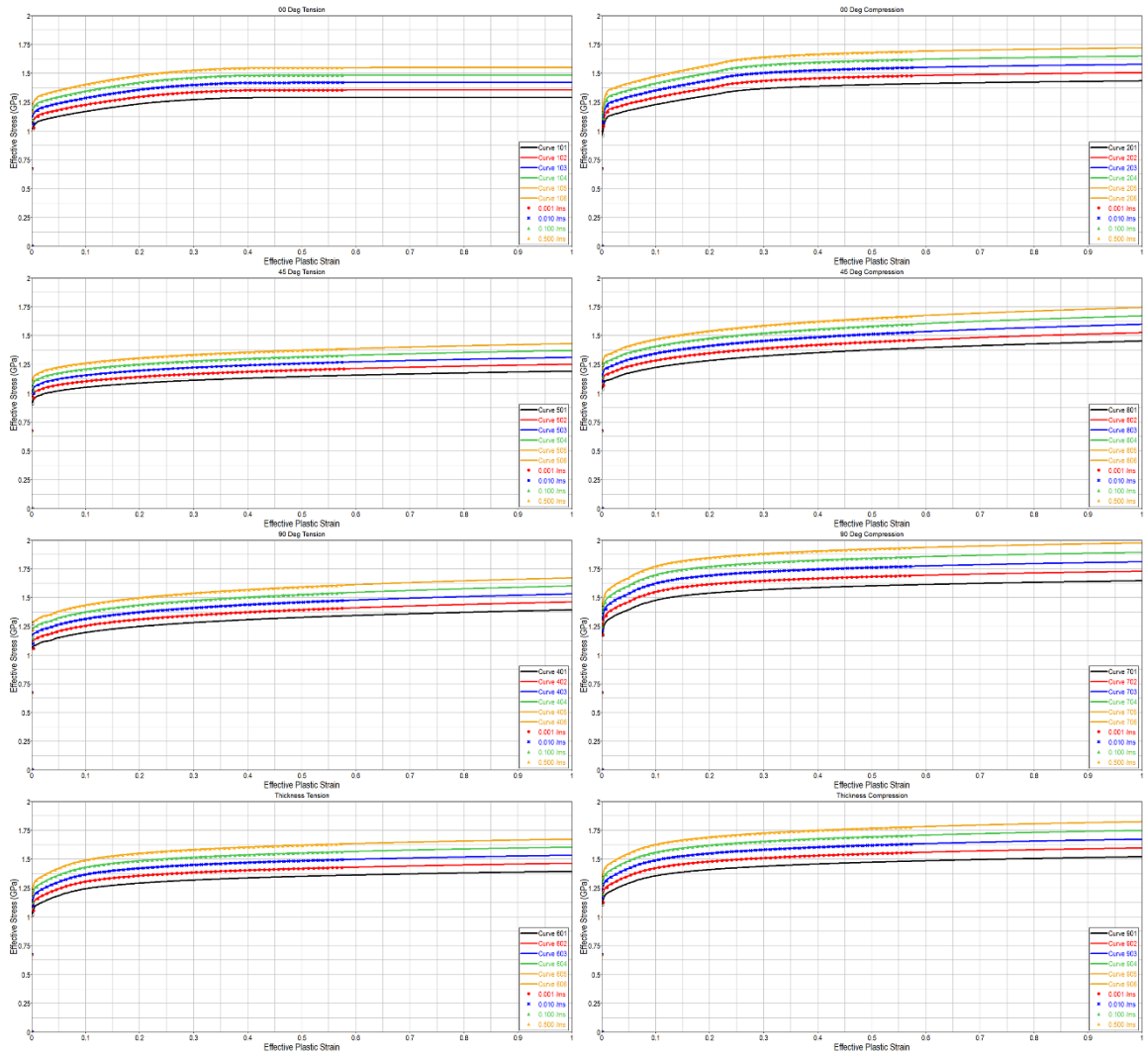


Figure 22: Single element verification for strain rate results

Based on the results shown in Figure 22, all of the individual strain rate simulations match the input yield curves for that strain rate. This is expected because this material model is based on tabulated inputs. The actual measured strain rate for each element in each strain rate simulation is shown in Figure 23. This plot shows the strain rate for each element, as a function of simulation time. This plot verifies that the actual

input strain rate is equal to the proposed value, and that the material routine is calculating the appropriate stress value. Therefore, the strain rate dependency portion of the material routine is verified for single elements.

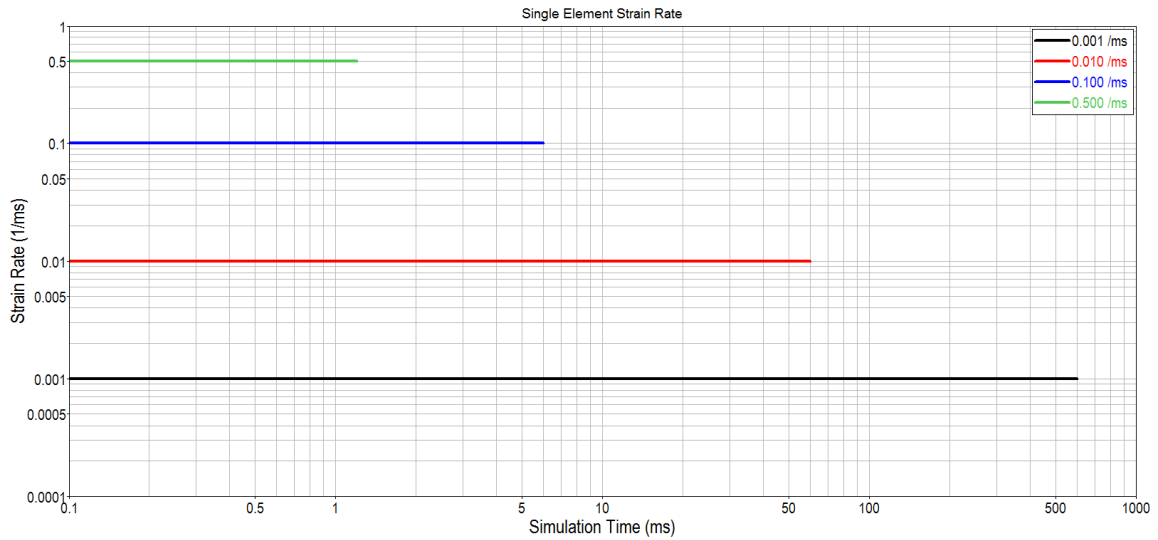


Figure 23: Single element strain rate verification

The next single element verification simulation is to test the thermal portion of the material model. These simulation tests both the flow stress, at varying temperatures, and the effect of the beta coefficient. The beta coefficient is the fraction of plastic work that is converted to heat. Therefore, if beta is equal to zero, the element should not change temperature as it is deformed. The larger the value of beta, the more the element will heat up, due to plastic work from deformation.

To test this part of the routine, a material input keyword is created where each material direction has multiple yield curves that are dependent on temperature. Like the

strain rate dependent table, these thermal tables reference different yield curves that depend on the value of the temperature for that element. Also similar to the strain rate dependency verification, the quasi-static room temperature yield curve for each direction was scaled for each point in the curve. Scaled input yield curves are generated for temperatures of: 293 K, 393 K, 493 K, and 593 K (Table 5).

```

*MAT_TABULATED_JOHNSON_COOK_ORTHO_PLASTICITY
$      MID      RO      E      PR      CP      TR      BETA      NUMINT
$      1      2.7E-6      74.66      0.3      8.75E+2      293      1E-10      0.0
$      T00R      T00T      LCF      LCG      LCH      LCI
$      100      1100
$      C00R      C00T      S45R      S45T      SFIEPM      NITER      AOPT
$      200      1200      300      1300      2      10      2
$      T90R      T45R      TTHR      C90R      C45R      CTHR
$      400      500      600      700      800      900
$      T90T      T45T      TTHT      C90T      C45T      CTHT
$      1400      1500      1600      1700      1800      1900
$      XP      YP      ZP      A1      A2      A3      MACF
$      V1      V2      V3      D1      D2      D3      BETA
$      0.0      0.0      1.0
$      0.0      -1.0      0.0

*DEFINE_TABLE
$ 0-degree Tension Temperature Table
$#      TBID
$#      1100
$#      TEMPERATURE      LCID
$#      293.0000000      1101
$#      393.0000000      1102
$#      493.0000000      1103
$#      593.0000000      1104

```

Figure 24: Anisotropic and temperature dependent material model input

Table 5: Single element temperature yield curve scale factors

Temperature	Scale Factor
293 K	1.00
393 K	0.95
493 K	0.90
593 K	0.85

For each element material direction, the stress and temperature is plotted as a function of plastic strain (Figure 25). The solid red line is the simulation result for that element with the beta coefficient equal to zero. The dashed red line is the simulation result for that element with the beta coefficient equal to one. The blue lines in Figure 25 are the input yield curves at varying temperatures.

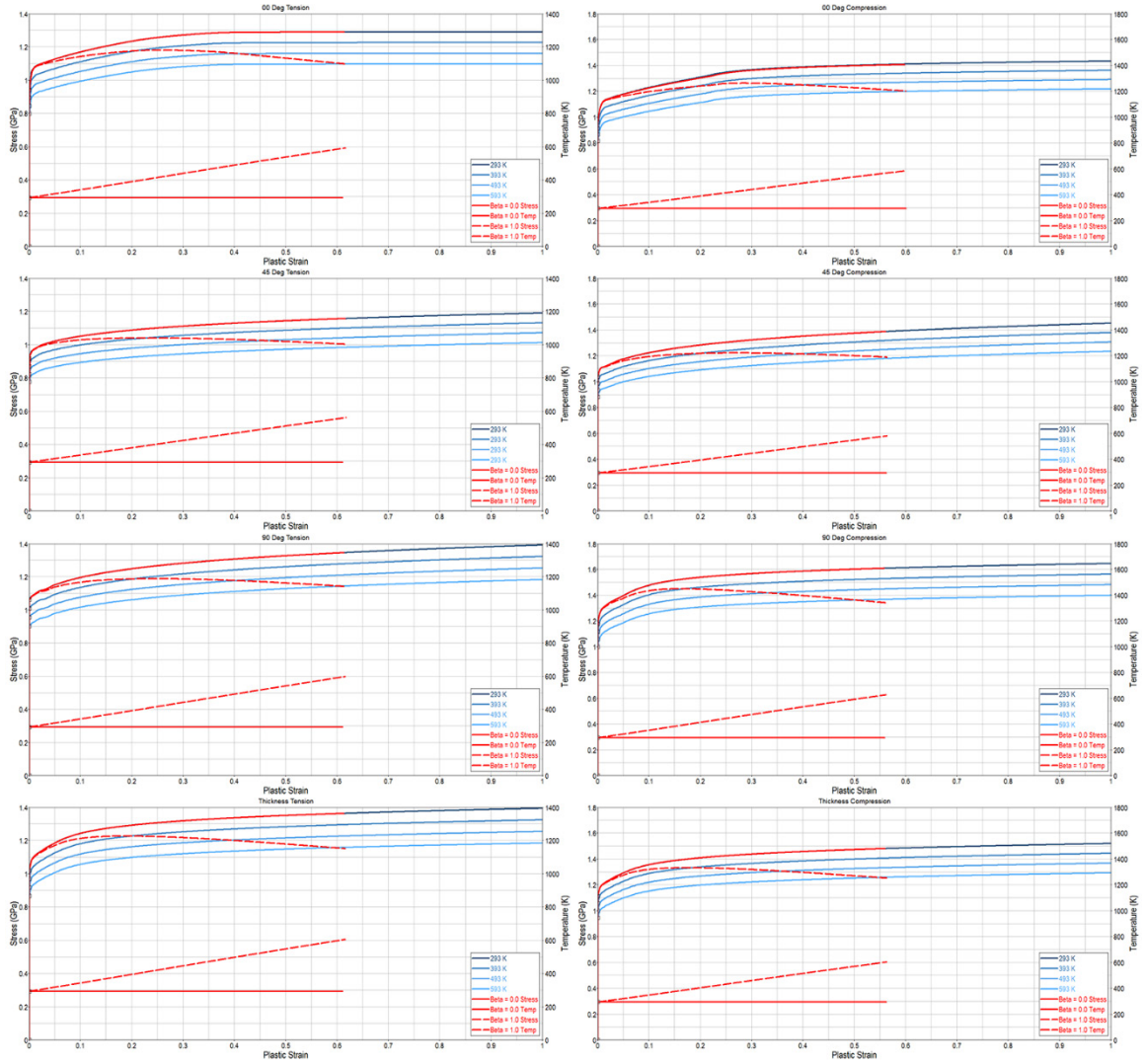


Figure 25: Single element verification for thermal results

As expected, when the beta coefficient is zero, the resulting flow stress matches the input yield curve for the 293 K (room) temperature. Additionally, the temperature of the element stays constant at 293 K. However, if the beta coefficient is set to unity, the element will increase in temperature and the flow stress will match (or interpolate) the input yield curve at that instantaneous temperature. For example, as the temperature of an

element rises to 593 K at a given plastic strain, the stress in that element should match the value of stress for the 593 K input yield curve at that specific plastic strain. This result verifies that the thermal component of this material model is correct.

In this material routine, the plasticity portion is an iterative process that will repeat until convergence is ensured. The number of iterations for this plasticity process is determined explicitly by the user. For example, the user can specify that the plasticity algorithm is repeated 200 times to ensure convergence. To test this specification, a set of single element simulations, similar to the strain rate verification simulations, were conducted to further understand the sensitivity of the number of specified iterations.

The single element simulation setup used for the 0.01 /ms was also used to test the number of iteration sensitivity. Originally, the number of iterations for the strain rate verification was set to 100. For this experiment, the number of iterations is varied from 5 to 100. The results from each element (0-degree, 45-degree, 90-degree and thickness) were compared to see how the number of iterations affects the material response.

Figure 26 shows the results from these single element simulations. It is clear that the number of specified iterations does affect the material response of the element. For this simulation, 5 and 10 iterations are not enough to ensure convergence of the plasticity algorithm. However, 25 iterations (and above) do seem to be sufficient to obtain convergence. Therefore it is recommended that the number of iterations when using this material model should be no less than 25 iterations. This is especially important when incorporating strain rate dependency.

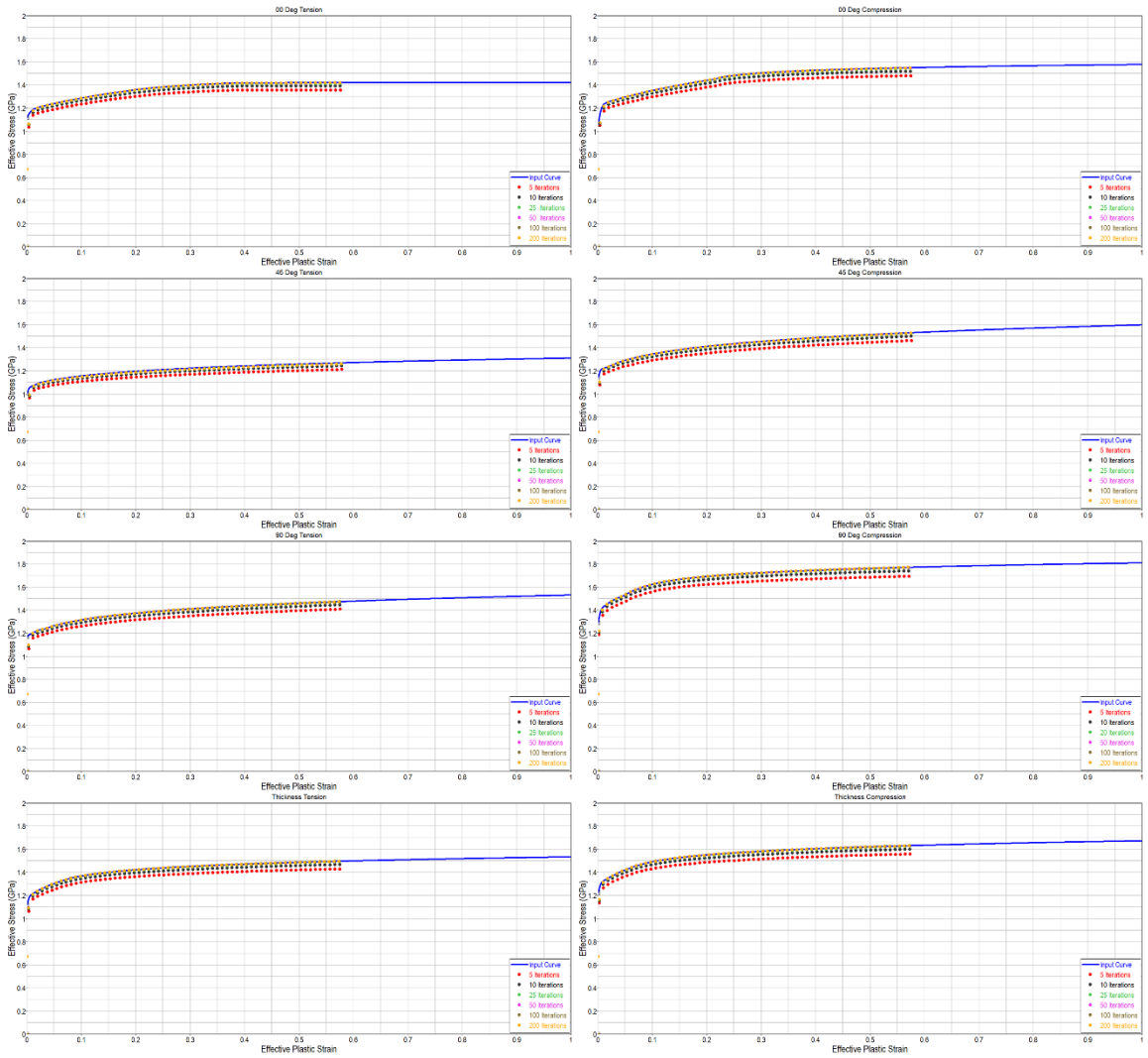


Figure 26: Single element simulation results with varying number of iterations

Another way to ensure that the plasticity algorithm has reached convergence is to apply a specific level of tolerance between iterations. This can be accomplished by allowing the user to specify a level of tolerance that will be compared to the result of the iteration. If the iteration for a specific element has converged to that level of tolerance, then that element will no longer iterate until the next time step. A similar study was

performed to test the sensitivity of the tolerance level. Using the single element 0.01 /ms strain rate simulation, the input tolerance was varied from 0.00001 to 0.01.

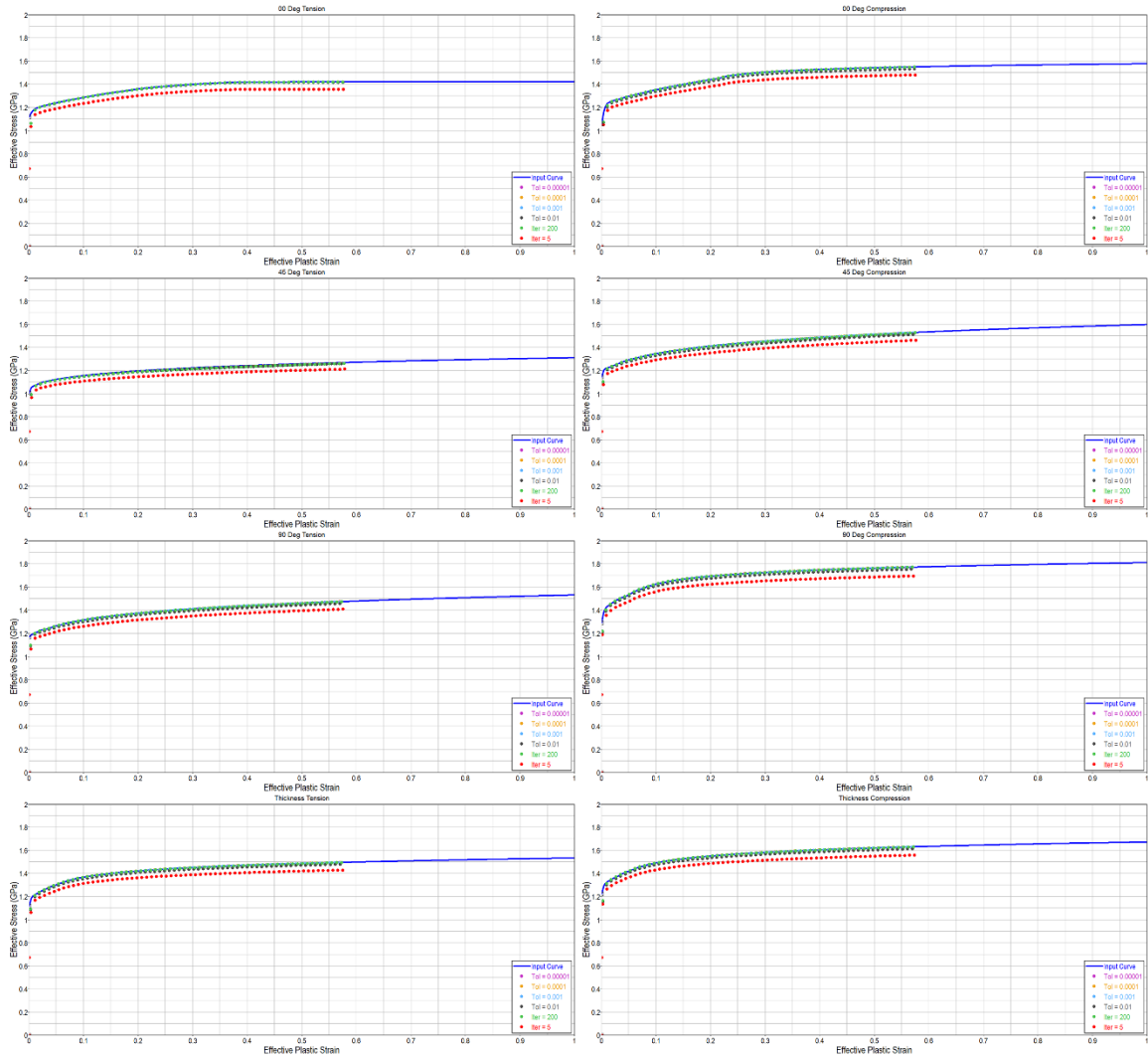


Figure 27: Single element simulation results with varying convergence tolerance

Figure 27 shows the results from the simulations with varying convergence tolerance. It is clear that a convergence tolerance of 0.001 (or smaller) does provide

appropriate results for this simulation. The default value, and recommended convergence tolerance for this material routine is set at 0.0001. However, this tolerance can be changed by the user for decreased computational time.

Using this single element simulation set up, the number of iterations and tolerance can be varied to determine the overall cost of the iterative process. This simulation was first conducted with a mandatory 5 iterations. Then, the simulation was repeated with a mandatory 200 iterations. Finally, the number of iterations was set to 200 but the tolerance was varied from 0.01 to 0.00001. The computation time varied from 12 seconds (with 5 iterations per time step) to 94 seconds (with 200 iterations per time step.) Table 6 shows a summary of the results.

Table 6: Computational cost as a function of number of iterations

Tolerance/Iterations	Computation Time	Average number of iterations
5 iterations	12 seconds	5
0.01 tolerance	26 seconds	13-28
0.001 tolerance	32 seconds	20-40
0.0001 tolerance	44 seconds	25-70
0.00001 tolerance	50 seconds	40-100
200 iterations	94 seconds	200

3.3 – Visualization of the Yield Surface

The visualization of the yield surface can sometimes be very important for research and development of industrial material models. A quick visualization of the yield surface will show the user if there are any apparent issues (ie. units) with any of the tabulated yield curves. Since there are many yield curves in this model, user error is a possibility and a quick visualization will alert the user to avoid such error.

Additionally, having a visualization of the yield surface will alert the developer if there are any portions of the yield surface that are not convex. Since a convex yield surface can be a numerical problem in some simulations, it is best to have it completely convex. As discussed in section 3.1.3, this material model does have enforced convexity conditions for most implementations. However, when attempting to model anisotropic and directional asymmetric materials, convexity is not necessarily enforced internally. In this case, it is advisable for the user of this material model to visualize the yield surface manually.

All of the coefficients needed to plot the yield surface are exported automatically for each element in LS-DYNA. This is accomplished by storing these yield surface coefficients as history variables, which can be analyzed and exported in a finite element post processor. The history variables that are used for the visualization of the yield surface are shown in Table 7.

Table 7: History variables used to visualize yield surface

History Variable #	Symbol	Description
21	c_1	Lode parameter coefficient
22	c_2	Lode parameter coefficient
23	c_3	Lode parameter coefficient
27	b_3	1 st Orthotropic third invariant coefficient
28	b_4	1 st Orthotropic third invariant coefficient
29	b_{10}	1 st Orthotropic third invariant coefficient
30	d_3	2 nd Orthotropic third invariant coefficient
31	d_4	2 nd Orthotropic third invariant coefficient
32	d_{10}	2 nd Orthotropic third invariant coefficient
33	F	Hill yield function coefficient
34	G	Hill yield function coefficient
35	H	Hill yield function coefficient
36	N	Hill yield function coefficient
37	s_y	Yield stress in current iteration

Using the equation of the yield surface (Equation 32) and the history variables defined in Table 7, individual equations for 2-D sections of the yield surface can be developed. For this analysis, three section equations (in polar coordinates, where α is the

angle) are developed to visualize the yield surface: 00-90 plane, 00-Shear45 plane, and 00-Thickness plane.

Equation 48: Yield surface visualization equation for 00-90 plane

$$\sigma(\alpha) = \frac{\sigma_y}{\sigma_{hill} * (c_1 + c_2\theta_1 + c_3\theta_2^2)}$$

Where:

$$\sigma_{hill} = \sqrt{F \tan(\alpha)^2 + G + H(1 - \tan(\alpha))^2}$$

$$\theta_1 = \frac{27 * \left(\frac{2}{27} + \frac{b_{03} + b_{04}}{27} \tan(\alpha)^3 - \frac{1}{9} \tan(\alpha) - \frac{1}{9} b_4 \tan(\alpha)^2 \right)}{2 * (1 + \tan(\alpha)^2 - \tan(\alpha)^{3/2})}$$

$$\theta_2 = \frac{27 * \left(\frac{2}{27} + \frac{d_{03} + d_{04}}{27} \tan(\alpha)^3 - \frac{1}{9} \tan(\alpha) - \frac{1}{9} d_{04} \tan(\alpha)^2 \right)}{2 * (1 + \tan(\alpha)^2 - \tan(\alpha)^{3/2})}$$

Equation 49: Yield surface visualization equation for 00-45Shear plane

$$\sigma(\alpha) = \frac{\sigma_y}{\sigma_{hill} * (c_1 + c_2\theta_1 + c_3\theta_2^2)}$$

Where:

$$\sigma_{hill} = \sqrt{G + H + 2N \tan(\alpha)^2}$$

$$\theta_1 = \frac{27 * \left(\frac{2}{27} - \frac{\tan(\alpha)^2}{3} (1 - 2b_{10}) \right)}{(1 + 3 \tan(\alpha)^2)^{3/2}}$$

$$\theta_2 = \frac{27 * \left(\frac{2}{27} - \frac{\tan(\alpha)^2}{3} (1 - 2d_{10}) \right)}{(1 + 3 \tan(\alpha)^2)^{3/2}}$$

Equation 50: Yield surface visualization equation for 00-Thickness plane

$$\sigma(\alpha) = \frac{\sigma_y}{\sigma_{hill} * (c_1 + c_2\theta_1 + c_3\theta_2^2)}$$

Where:

$$\sigma_{hill} = \sqrt{F \tan(\alpha)^2 + G + H(1 - \tan(\alpha))^2}$$

$$\theta_1 = \frac{27 * \left(\frac{2}{27} + \frac{1 + 2b_4 - b_3}{27} \tan(\alpha)^3 - \frac{1}{9} \tan(\alpha) - \frac{1}{9} b_4 \tan(\alpha)^2 \right)}{2 * (1 + \tan(\alpha)^2 - \tan(\alpha)^{3/2})}$$

$$\theta_2 = \frac{27 * \left(\frac{2}{27} + \frac{d_{03} + d_{04}}{27} \tan(\alpha)^3 - \frac{1}{9} \tan(\alpha) - \frac{1}{9} d_{04} \tan(\alpha)^2 \right)}{2 * (1 + \tan(\alpha)^2 - \tan(\alpha)^{3/2})}$$

By using the history variables from a simulation, like the single element simulations described in section 3.2.2, each variable can be imported into a graphing program or tool. Since the history variables are stored for each LS-DYNA D3PLOT time step, the yield surface can be visualized at multiple time steps. Since the yield surface is distortional, it is expected that the size and shape of the surface may change as a function of simulation time (or deformation). Therefore, each of these plots have many surfaces plotted on top of each other, representing the surface at a specified simulation time.

Figure 28 shows each of the three yield surface section visualizations for an anisotropic and symmetric implementation of this material model. This means that there is different input yield curves in each of the four material directions, however there is no tension/compression asymmetry. For this model, the input yield curves are exactly the same for tension and compression for a specific material direction. Using this implementation of the material model, convexity is enforced internally in the subroutine.

Figure 29 shows each of the three yield surface section visualizations for an anisotropic and directionally asymmetric implementation of this material model. This

means that there is unique input yield curves for each of the four material directions in tension and compression. This one implementation of the material model does not internally enforce convexity, so it is recommended that this visualization procedure is conducted to see the extent of any possible concave areas. If the surface is not convex, numerical issues may arise in a simulation. The user can manually adjust the input yield curves until the yield surface is convex. The code used to visualize this yield surface can be found in the appendix.

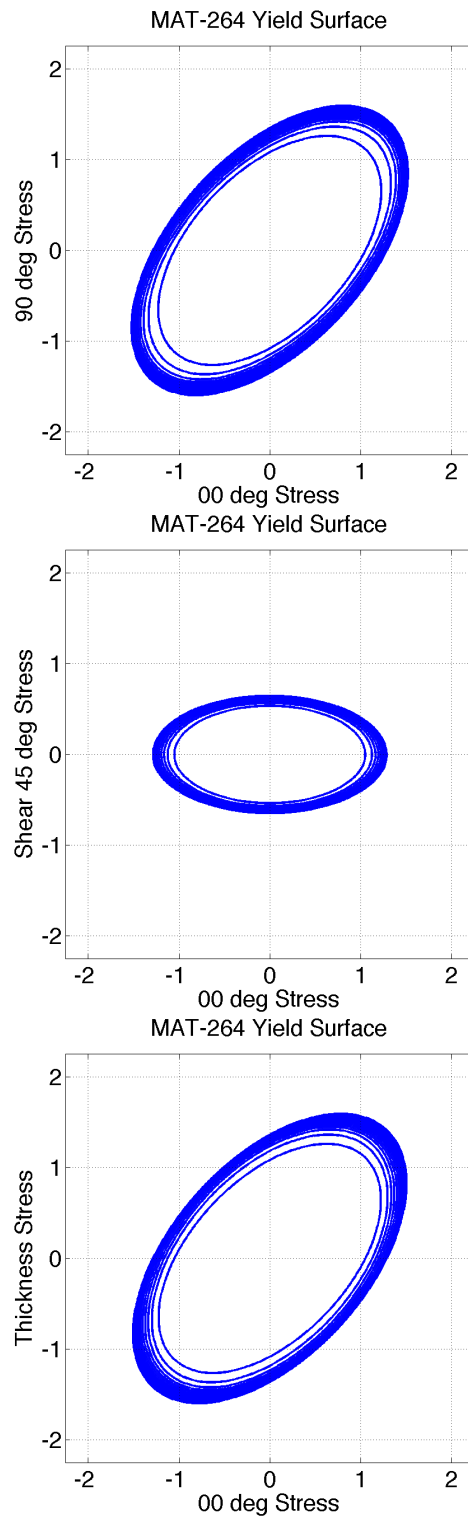


Figure 28: Visualization of Anisotropic symmetric yield surface

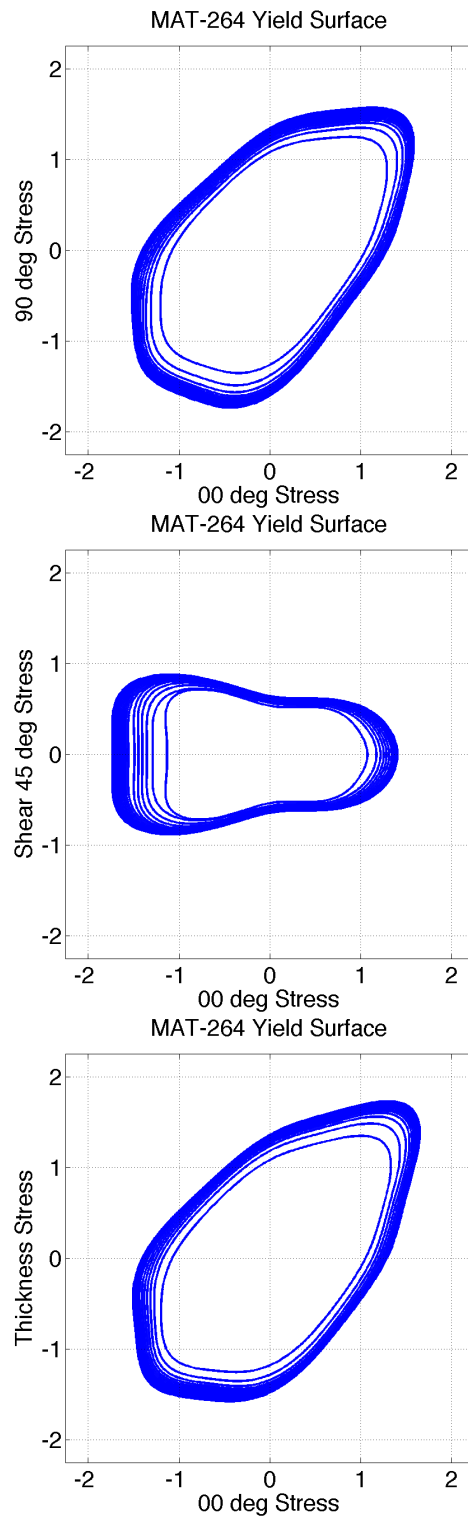


Figure 29: Visualization of Anisotropic and directional asymmetric yield surface

CHAPTER 4 - MATERIAL MODEL VALIDATION

4.1 – Al-2024 Material Validation

This section describes the Al-2024 material testing and model development programs. First, the material will be fully defined and the design of the material testing specimens will be described. The results from the material tests will be presented and a material characterization is performed. Lastly, the results of the specimen simulations will be compared to the physical test data.

4.1.1 – Al-2024 Material Testing Program

The first material used for validation of this new model is a 12.7 mm (0.50 inch) rolled aluminum plate. This material is often used in both automotive and aerospace applications. Since cubic crystal structures, such as steel and aluminum, typically have similar yield stress in tension and compression [38], this material will be used to validate tension anisotropy portion of the material model. The chemical composition of the Al-2024-T351 plate is shown in Table 8 [14].

Table 8: Composition of 12.7mm thick 2024-T351 aluminum plate [14]

Plate Stock	Chemistry									
Alloy/ Treatment	Si	Fe	Cu	Mn	Mg	Cr	Zn	Ti	V	Zr
2024-T351	0.08	0.22	4.47	0.59	1.37	0.01	0.18	0.02	0.01	0.01

Tension specimens were conducted in several directions relative to the plate's rolling axis. The tests were conducted at The Ohio State University [14] on a servohydraulic load frame at room temperature. Each tension and compression specimen was deformed at an approximate strain rate of 1.00 (1/s).

The smooth uniaxial tension specimen has a nominal gage length of 5.08 mm and a nominal gage width of 3.05 mm. The thickness of the uniaxial tension specimen is 0.76 mm. A technical drawing of the uniaxial tension specimen is showing in Figure 30.

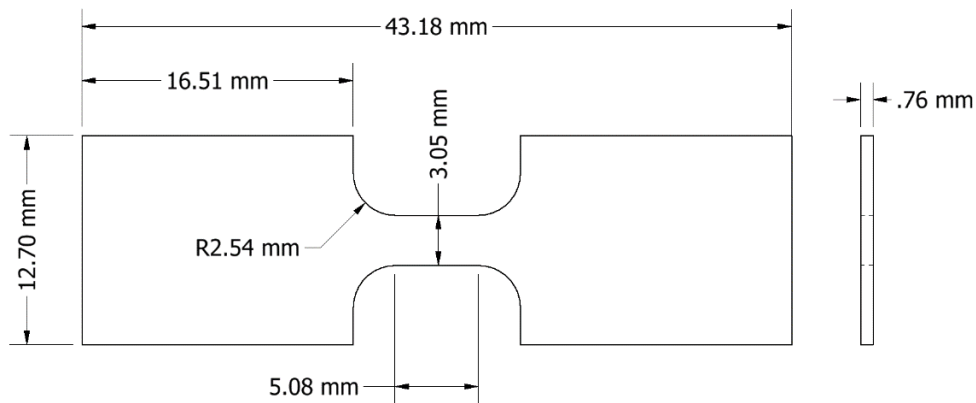


Figure 30: Al-2024 uniaxial tension specimen specifications

These uniaxial tension specimens were cut from the aluminum plate in three directions relative to the rolling axis: 0-degree, 45-degree, and 90 deg. Each specimen was tested multiple times and the results from those tests are shown in Figure 31. Orientation 1 (O1 in the plot legend) is the rolling direction, orientation 2 is the 45-degree direction and orientation 3 is in the 90-degree direction relative to the rolling axis.

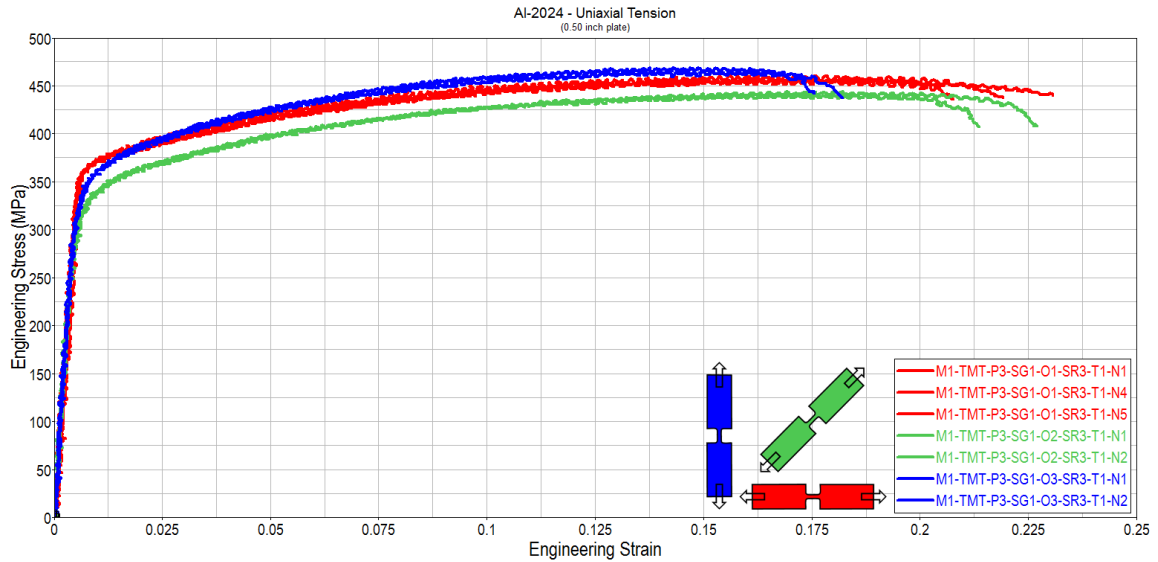


Figure 31: Al-2024 uniaxial tension test data

Figure 31 shows that this aluminum plate does exhibit some amount of anisotropy in tension. Both the initial yield stress and the flow stress for each specimen direction seem to have different values which makes this material an acceptable candidate for use in this validation.

4.1.2 – Al-2024 Material Model Parameters

To properly simulate the uniaxial tension specimens for the 2024-T351 aluminum sheet using this new model, appropriate material properties must be determined. This process occurs in two phases: determination of basic material properties and development of tabulated yield curves in each direction.

This material model requires the user to provide specific material properties such as density, Young’s modulus and Poisson’s ratio. The properties used for this material model are show in Table 9.

Table 9: Material model properties for Al-2024

Density <i>Kg/mm³</i>	Young's Modulus <i>GPa</i>	Poisson's Ratio	Specific Heat <i>J/kgK</i>
2.6 E-06	70.0	0.33	900.0

In addition to these material parameters, input yield curves must be determined for each direction. To accomplish this, each material specimen direction was simulated individually using the Tabulated Johnson-Cook material model in LS-DYNA [11]. After the appropriate yield curve was found for each individual material direction, they could be combined in to this anisotropic material model.

The process for determining an appropriate yield curve can be outlined in previous work by the U. S. Federal Aviation Administration [39]. By using the engineering stress and engineering strain data provided by the material testing program, the true stress and true strain for this material can be calculated.

Equation 51: True stress calculation

$$\sigma_{true} = \sigma_{eng}(1 + \varepsilon_{eng})$$

Equation 52: True strain calculation

$$\varepsilon_{true} = \ln(1 + \varepsilon_{eng})$$

For this type of uniaxial tension test, the conversion of engineering stress/strain to true stress/strain requires the following assumptions:

1. Stress is uniform over the center cross section of the specimen at all times
2. Cross sectional area is constant in the area measured by the extensometer (constant in space and not in time)
3. There is no stress in the transverse and thickness directions
4. Strain components in the transverse and thickness directions are -0.5 times the longitudinal strain
5. Strain is uniform in the area measured by the extensometer

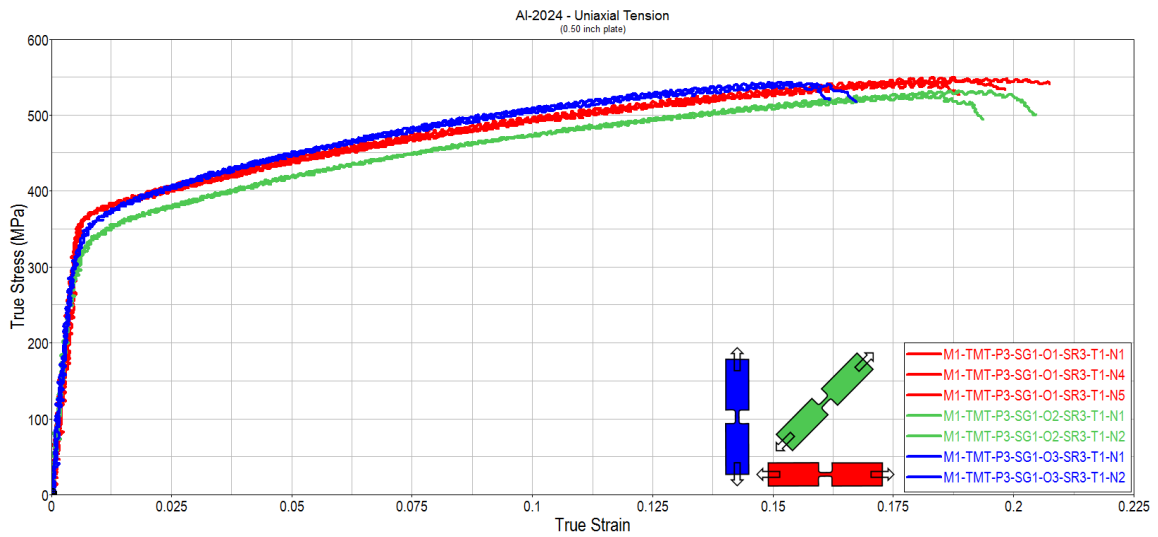


Figure 32: Al-2024 true stress vs. true strain

The next step in determining the input yield curve for each material specimen direction is to find the appropriate yield point. For this application, the yield point is chosen at the point at which the stress-strain curve is no longer linear.

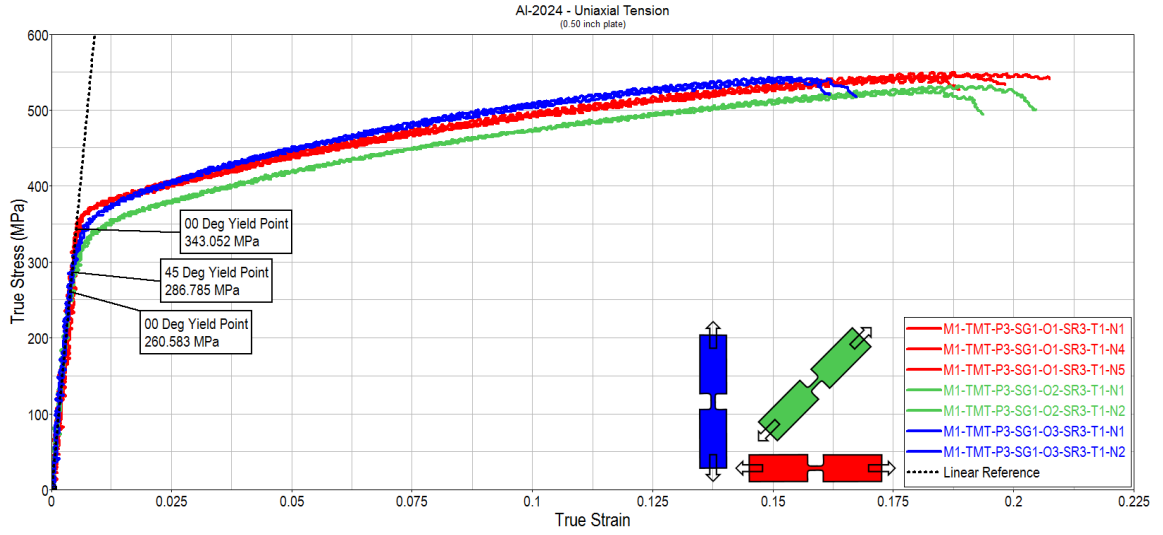


Figure 33: Al-2024 yield point

After the yield point is chosen, the elastic portion of the curve is removed so that only the plastic component remains. The plastic strain, ε_p , can be calculated for the input yield curve.

Equation 53: Plastic strain calculation

$$\varepsilon_p = \varepsilon - \frac{\sigma}{E}$$

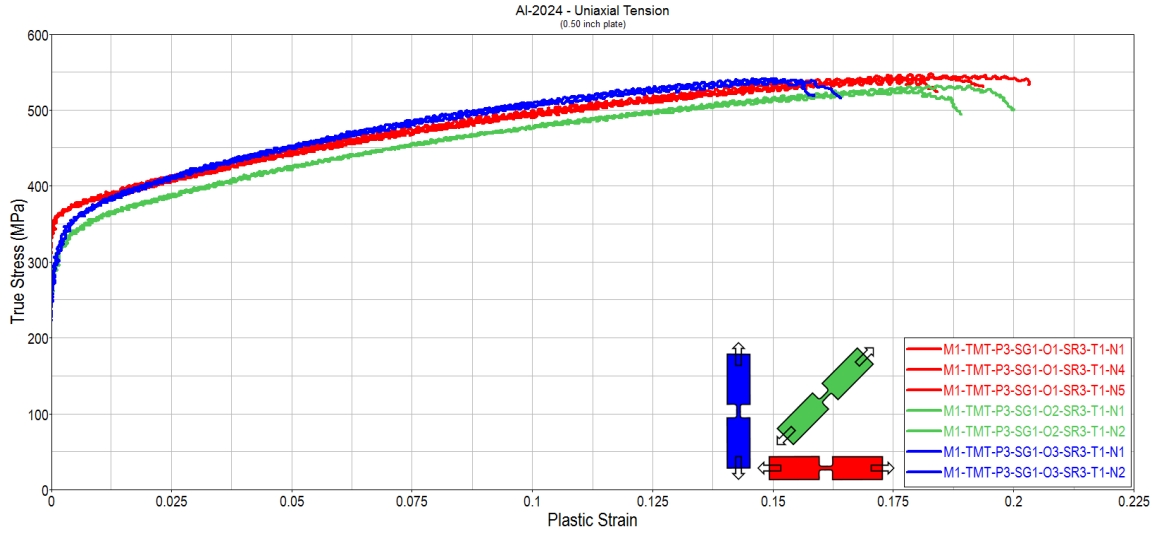


Figure 34: Al-2024 true stress vs. plastic strain

At this stage in the yield curve generation process, the flow stress after the necking point must be reevaluated against the initial assumptions. After necking, the cross sectional is much smaller in the localized region and therefore not constant in the area covered by the extensometer. After the necking point, transversal and thickness stresses will develop. Beyond the necking point, the specimen is no longer in a uniaxial tension state of stress.

Equation 54 shows the state of stress in the gage length before necking. Note that the only component of stress is the longitudinal stress and the von Mises stress is equal to the longitudinal stress (σ_l). Equation 55 shows the state of stress after the necking point. At this point, a transverse stress (σ_t) appears in the stress tensor and the von Mises stress does not equal the longitudinal stress. Lastly, Equation 56 shows the state of stress after necking and some localized thinning. At this point, some thickness stress (σ_{tt}) exists due to the material resistance against thinning.

Equation 54: State of stress before necking

$$\boldsymbol{\sigma} = \begin{pmatrix} \sigma_l & 0 & 0 \\ 0 & 0 & 0 \\ 0 & 0 & 0 \end{pmatrix} \quad \sigma_{vm} = \sigma_l$$

Equation 55: State of stress after diffuse necking

$$\boldsymbol{\sigma} = \begin{pmatrix} \sigma_l & 0 & 0 \\ 0 & \sigma_t & 0 \\ 0 & 0 & 0 \end{pmatrix} \quad \sigma_{vm} \neq \sigma_l$$

Equation 56: State of stress after local necking

$$\boldsymbol{\sigma} = \begin{pmatrix} \sigma_l & 0 & 0 \\ 0 & \sigma_t & 0 \\ 0 & 0 & \sigma_{tt} \end{pmatrix} \quad \sigma_{vm} \neq \sigma_l$$

Since any experimental data after the necking point cannot be used to generate an appropriate yield curve, only the data prior to necking can remain. To find the necking point, the derivative of the stress vs. strain curve was calculated and plotted together with the original experimental data [39]. This process may require some smoothing of the original data in order to get a smooth curve for the tangent modulus. Figure 35 shows an example of the process for determining the necking point of the 0-degree specimen. All of the stress and strain data beyond the necking point can be removed.

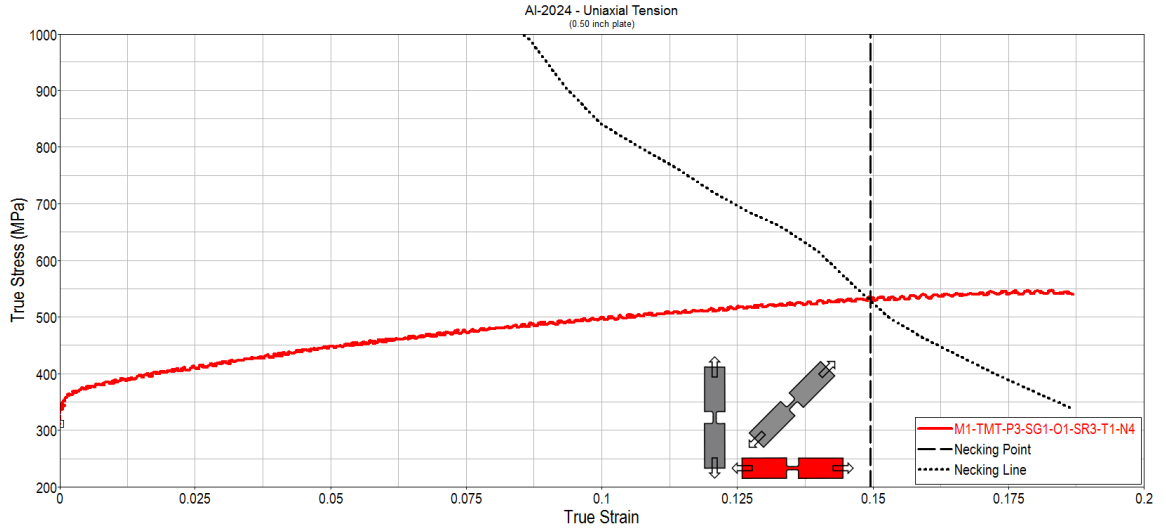


Figure 35: Al-2024 determination of the necking point for the 0-degree specimen

After the necking point is determined an extrapolation process is required to determine the part of the yield curve after the necking point. The extrapolated portion of the yield curve can be calculated from Equation 57 where: k , ε_e , and n are fitting parameters.

Equation 57: Yield curve extrapolation equation

$$\sigma = k(\varepsilon_e + \varepsilon_p)^n$$

The exponent, n , varies from 0 to 1 as the yield curve is expected to monotonically increase and have a monotonically decreasing tangent. Additionally, the transition between the true stress vs. true strain curve and the extrapolated curve should be continuous and smooth.

Equation 58: Yield curve continuous extrapolation

$$A = \sigma|_{\varepsilon=\varepsilon_0}, B = \varepsilon|_{\varepsilon=\varepsilon_0}$$

Equation 59: Yield curve smooth extrapolation

$$A = \sigma|_{\varepsilon=\varepsilon_0}, C = \frac{d\sigma}{d\varepsilon}|_{\varepsilon=\varepsilon_0}$$

Equation 58 and Equation 59 have three additional coefficients, A , stress at necking, B , plastic strain at necking and C , the slope (hardening modulus). Since there are three variables and only two boundary conditions, the extrapolation is not uniquely defined and one the parameter can be freely chosen. Typically, the parameter n is freely chosen and the other two parameters are calculated in Equation 60 and Equation 61. At the necking point, $A = C$ and therefore the extrapolation equation for parameter e can be simplified to $\varepsilon_e = n - B$.

Equation 60: Yield curve extrapolation equation for parameter k

$$k = A \left(\frac{An}{C} \right)^{-n}$$

Equation 61: Yield curve extrapolation equation for parameter e

$$\varepsilon_e = \frac{An}{C} - B$$

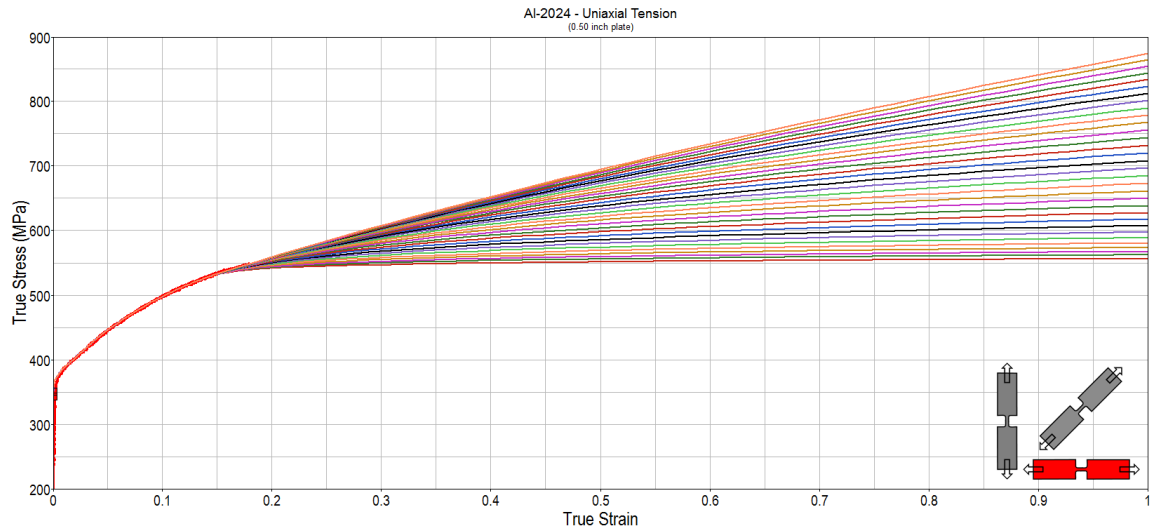


Figure 36: Al-2024 extrapolated yield curves for 0-degree specimen

For each specimen, 32 unique yield curves were generated and formatted as a LS-DYNA *DEFINE_CURVE keyword. A simulation was designed to replicate the uniaxial tension experiment. A finite element mesh of the tensile test specimen was created with 46,208 solid elements (0.2 mm element size). The dimensions of each specimen direction were applied to the finite element mesh so that the cross sectional area, gage length, and curvature were identical to the measured test values. Using the Tabulated Johnson-Cook material model in LS-DYNA, each individual yield curve was simulated and the results were analyzed. By using this method, each specimen direction yield curve can be generated independently of the other specimen directions. After each yield curve was simulated, one candidate was selected to represent that material specimen direction. The results from the isotropic Tabulated Johnson-Cook material model are shown in Figure 38.

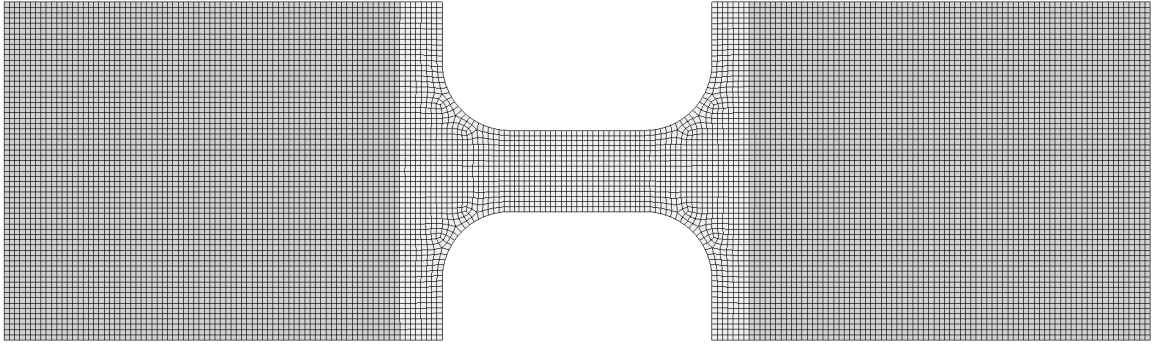


Figure 37: Al-2024 uniaxial tension specimen finite element mesh

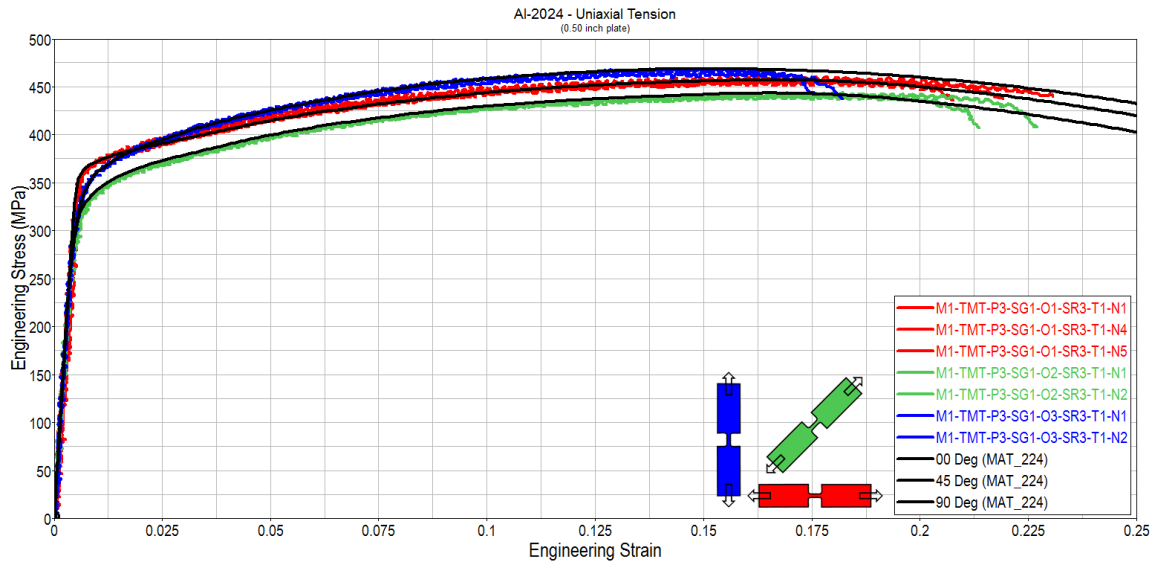


Figure 38: Al-2024 simulation results with Tabulated Johnson-Cook material model

Now that three independent tabulated yield curves have been selected to represent the 0-degree, 45-degree and 90-degree tension directions, they can be used in the anisotropic material model presented in this dissertation. The final yield curves for each material direction are shown in Figure 39.

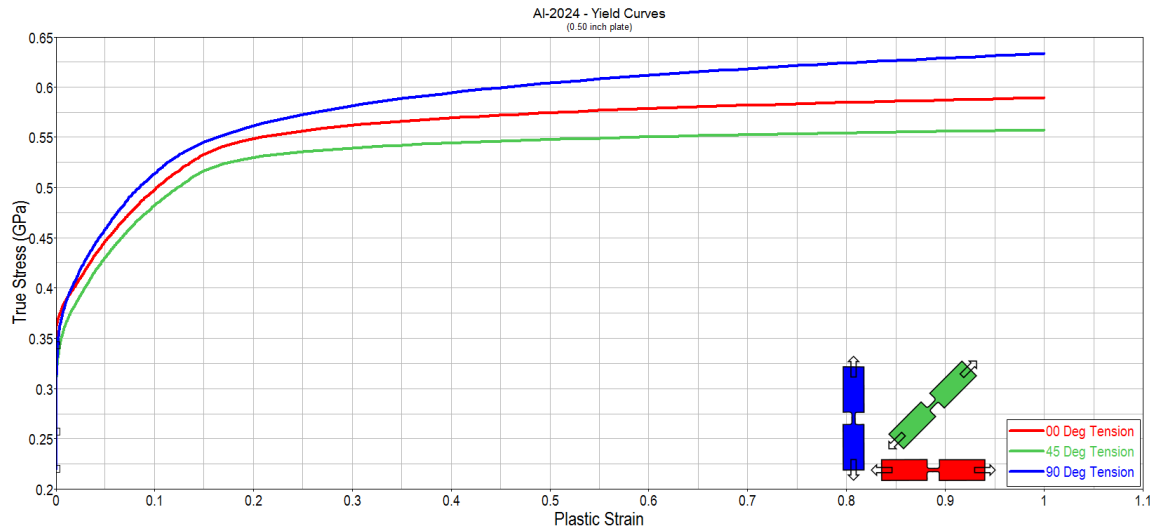


Figure 39: Al-2024 selected yield curves

4.1.3 – Al-2024 Material Model Validation Program

With the input yield curves generated in section 4.1.2, a full anisotropic material model for Al-2024 can be compiled. This material is used to validate the tension component of the model and therefore the yield curves in tension (Figure 39) are used. In order to verify each material direction, three unique simulations are designed using the same material model. The only difference between each model is the specimen dimensions, which are specified for each individual specimen, and the definition of the material axis in the material axis option (AOPT) portion of the model. The total material input is shown in Figure 40. The material axis option, for each specimen direction, is shown in Table 10. These options assume that the specimen is on the simulation x-y plane and pulled in the +x direction (thickness in the +z direction).

*MAT_TABULATED_JOHNSON_COOK_ORTHO_PLASTICITY								
\$	Al-2024	00	DEG					
\$	MID	RO	E	PR	CP	TR	BETA	NUMINT
	2	2.6000E-6	70.00000	0.333000	900.00000	293.00000	1.000000	1.000000
\$	T00R	T00T	LCF	LCG	LCH	LCI		
	100							
\$	C00R	C00T	S45R	S45T		SFIEPM	NITER	AOPT
	200		300			2	200	2
\$	T90R	T45R	TTHR	C90R	C45R	CTHR		
	400	500	600					
\$	T90T	T45T	TTHT	C90T	C45T	CTHT		
\$	XP	YP	ZP	A1	A2	A3	MACF	
				1.0	0.0	0.0		
\$	V1	V2	V3	D1	D2	D3	BETA	
				0.0	1.0	0.0		

Figure 40: Material input card for Al-2024 (0-degree)

Table 10: Al-2024 material axis options for each specimen direction in tension

Specimen direction	A1	A2	A3	D1	D2	D3
00 deg	1.0	0.0	0.0	0.0	1.0	0.0
45 deg	1.0	-1.0	0.0	1.0	1.0	0.0
90 deg	0.0	-1.0	0.0	1.0	0.0	0.0

Each specimen was simulated using the same material model (with the exception of the material axis options) and the resulting engineering stress/strain was compared to the original test data described in section 4.1.1. These results are shown in Figure 41.

It should be noted that there is some interaction between the three directions after necking occurs. However, the influence of this seems to be small enough to be neglected in this case (and for the purposes of generating yield curves).

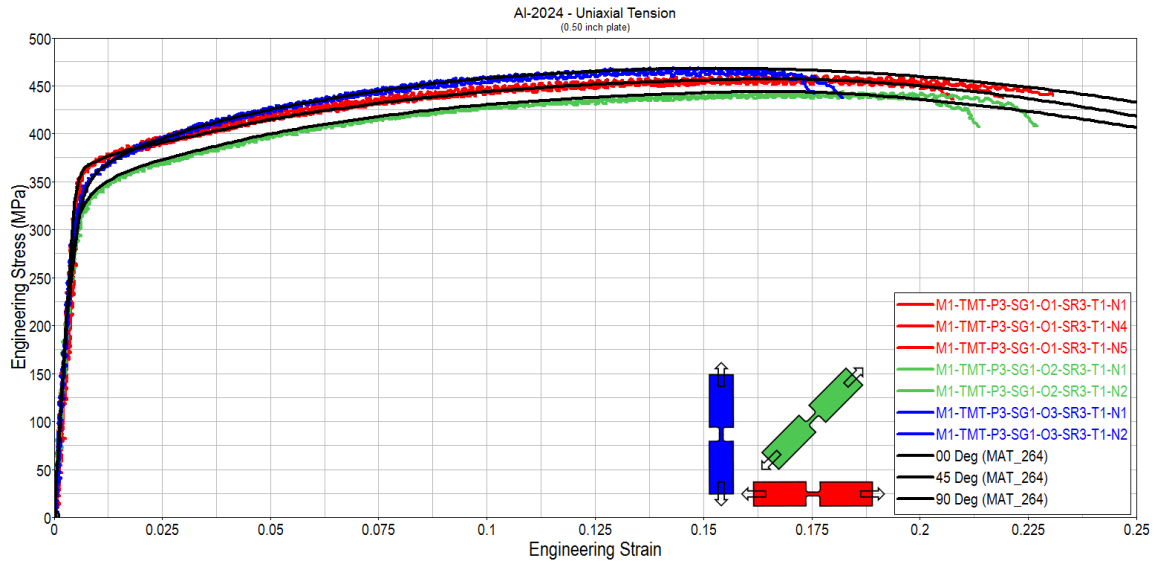


Figure 41: Al-2024 simulation results with anisotropic material model

4.2 – Ti-6Al-4V Material Validation

This section describes the Ti-6Al-4V material testing and model development programs. First, the material will be fully defined and the design of the material testing specimens will be described. The results from the material tests will be presented and a material characterization is performed. Lastly, the results of the specimen simulations will be compared to the physical test data.

4.2.1 – Ti-6Al-4V Material Testing Program

The second material used for validation of this material model is a 6.35 mm (0.25 inch) titanium alloy rolled plate [15]. This material is often used in the aerospace industry due to its high strength-density ratio. Ti-6Al-4V is a hexagonal closed packed (HCP) structure and its flow stress is strongly dependent on both the strain rate and temperature

[40]. Unlike cubic centered crystal structures, Ti-6Al-4V exhibits a strength asymmetry between tension and compression. This asymmetry makes Ti-6Al-4V an excellent candidate to validate the tension and compression components of this material model. The chemical composition of this specific Ti-6Al-4V plate is shown in Table 11.

Table 11: Composition of 6.35mm thick Ti-6Al-4V plate [15]

Plate Stock	Chemistry					
Alloy/Treatment	Al	V	Fe	O	C	N
Ti-6Al-4V	6.13	3.94	0.18	0.173	0.016	0.006

Uniaxial tension specimens were manufactured from this Ti-6Al-4V plate in the 0-degree, 45-degree and 90-degree directions relative to the rolling axis. Additionally, cylindrical compression specimens were manufactured in the 0-degree, 45-degree, 90-degree and thickness directions relative to the rolling axis. Both the tension and compression material tests were conducted at The Ohio State University [15] on a hydraulic load frame at a strain rate of 1.00 (1/s) at room temperature.

The uniaxial tension specimen has a gage length of 5.08 mm, a gage width of 2.03 mm, a thickness of 0.67 mm and a transition radius of 1.19 mm. The total width of the tension specimen is 12.70 mm and the total length of the specimen is 63.50 mm. The uniaxial cylindrical compression specimen has an overall diameter of 3.81 mm and a total length of 3.81 mm. Technical drawings of the uniaxial tension specimen and the uniaxial cylindrical compression specimen are shown in Figure 42 and Figure 43.

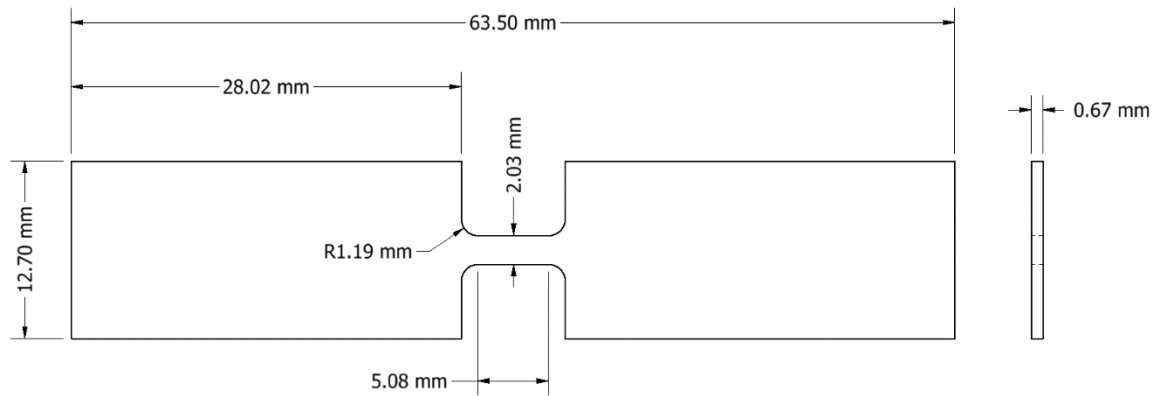


Figure 42: Ti-6Al-4V uniaxial tension specimen specifications

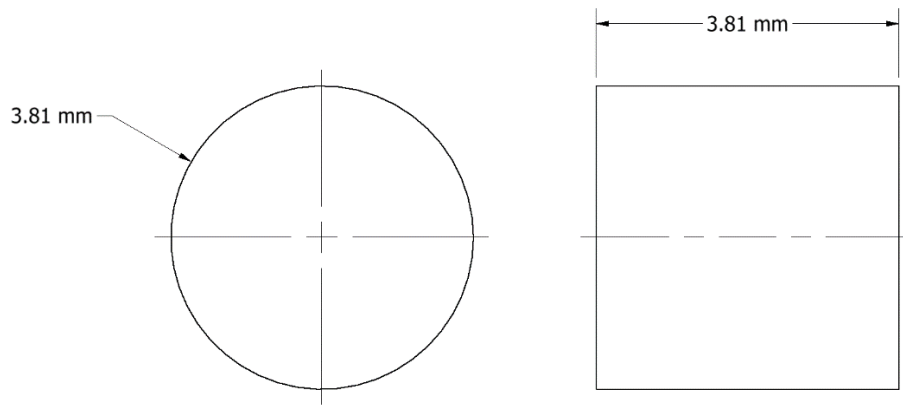


Figure 43: Ti-6Al-4V compression specimen specifications

The uniaxial tension specimens were cut from the titanium plate in three directions relative to the rolling axis: 0-degree, 45-degree, and 90 deg. Each specimen was tested multiple times and the results from those tests are shown in Figure 44. Orientation 1 (O1 in the plot legend) is the rolling direction, orientation 2 is the 45-degree direction and orientation 3 is in the 90-degree direction relative to the rolling axis.

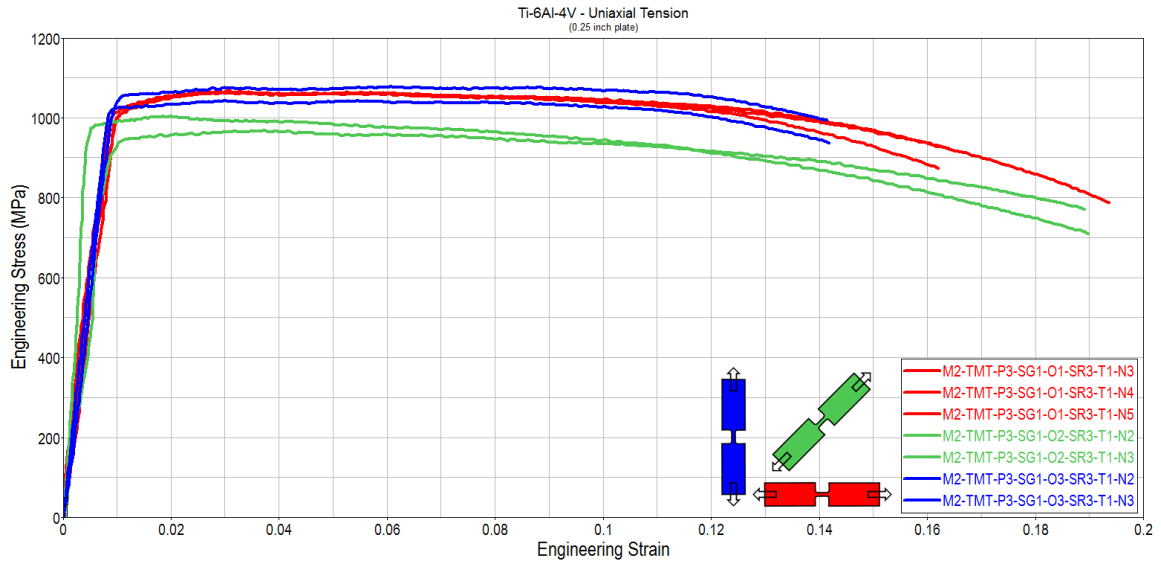


Figure 44: Ti-6Al-4V uniaxial tension test data

The uniaxial compression specimens were cut from the titanium plate in four directions relative to the rolling axis: 0-degree, 45-degree, 90-degree, and thickness. Each specimen was tested multiple times and the results from those tests are shown in Figure 45. Orientation 1 (O1 in the plot legend) is the rolling direction, orientation 2 is the 45-degree direction, orientation 3 is in the 90-degree direction and orientation 5 is the thickness direction relative to the rolling axis.

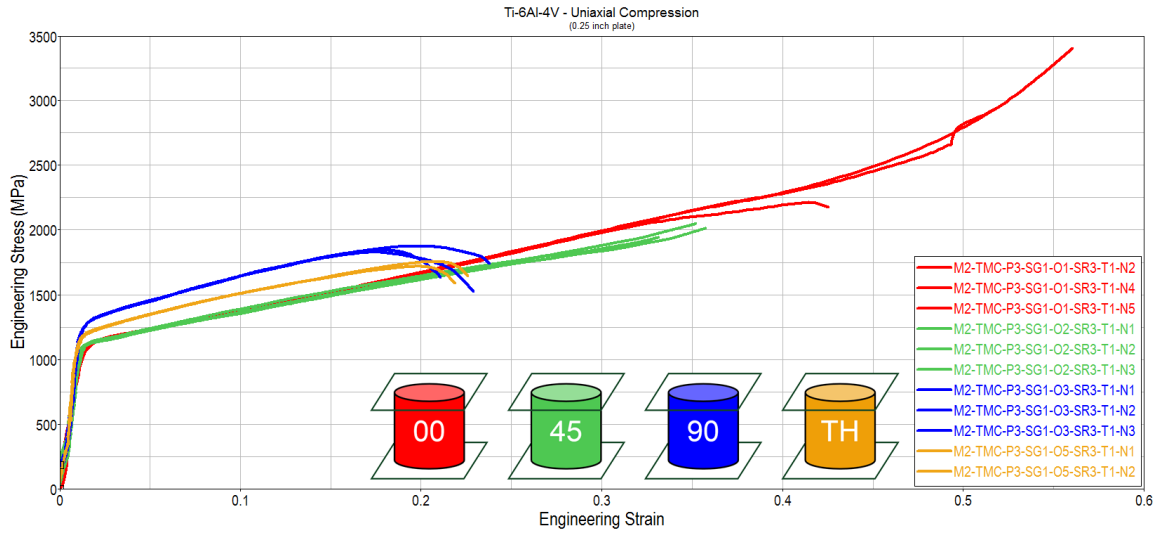


Figure 45: Ti-6Al-4V uniaxial compression test data

The uniaxial tension test results do show some material anisotropy, especially in the 45-degree direction. However, there seems to be very little anisotropy between the 0-degree and 90-degree directions. The uniaxial compression test results also show some material anisotropy. While there is little difference in the flow stress between the 0-degree and the 45-degree, there is some significant differences in the 90-degree and thickness directions. It is also important to note that there is significant tension-compression asymmetry in this Ti-6Al-4V plate.

4.2.2 – Ti-6Al-4V Material Model Parameters

To properly simulate the uniaxial tension specimens for the Ti-6Al-4V plate using this new model, appropriate material properties must be determined. This process occurs in two phases: determination of basic material properties and development of tabulated yield curves in each direction.

This material model requires the user to provide specific material properties such as density, Young's modulus and Poisson's ratio. The properties used for this material model are shown in Table 12.

Table 12: Material model properties for Ti-6Al-4V

Density <i>Kg/mm³</i>	Young's Modulus <i>GPa</i>	Poisson's Ratio	Specific Heat <i>J/kgK</i>
4.4 E-06	110.0	0.34	540.0

In addition to these material parameters, input yield curves must be determined for each direction. To accomplish this, each material specimen direction (in tension and compression) was simulated individually using the Tabulated Johnson-Cook material model in LS-DYNA [11]. After the appropriate yield curve was found for each individual material direction, they could be combined in to this anisotropic material model.

The process for determining an appropriate yield curve can be outlined in previous work by the U. S. Federal Aviation Administration [39]. By using the engineering stress and engineering strain data provided by the material testing program, the true stress and true strain for this material can be calculated. This section describes the process for determining the yield curves for the uniaxial tension specimens. The approach for generating yield curves for the uniaxial compression specimens is similar.

Equation 62: True stress calculation

$$\sigma_{true} = \sigma_{eng}(1 + \epsilon_{eng})$$

Equation 63: True strain calculation

$$\varepsilon_{true} = \ln(1 + \varepsilon_{eng})$$

For this type of uniaxial tension test, the conversion of engineering stress/strain to true stress/strain requires the following assumptions:

1. Stress is uniform over the center cross section of the specimen at all times
2. Cross sectional area is constant in the area measured by the extensometer (constant in space in not time)
3. There is no stress in the transverse and thickness directions
4. Strain components in the transverse and thickness directions are -0.5 times the longitudinal strain
5. Strain is uniform in the area measured by the extensometer

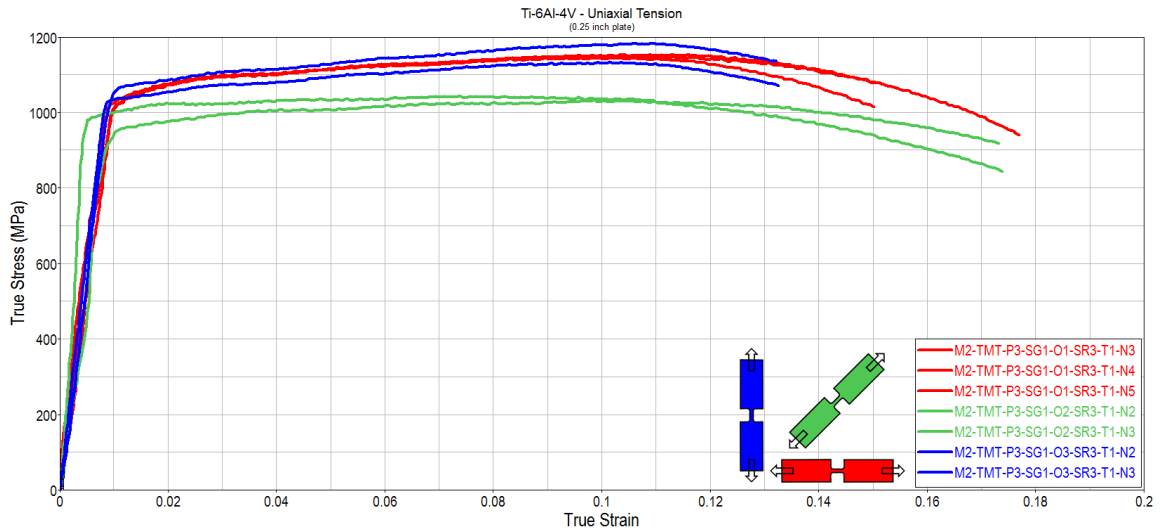


Figure 46: Ti-6Al-4V true stress vs. true strain

The next step in determining the input yield curve for each material specimen direction is to find the appropriate yield point. For this application, the yield point is chosen at the point at which the stress-strain curve is no longer linear.

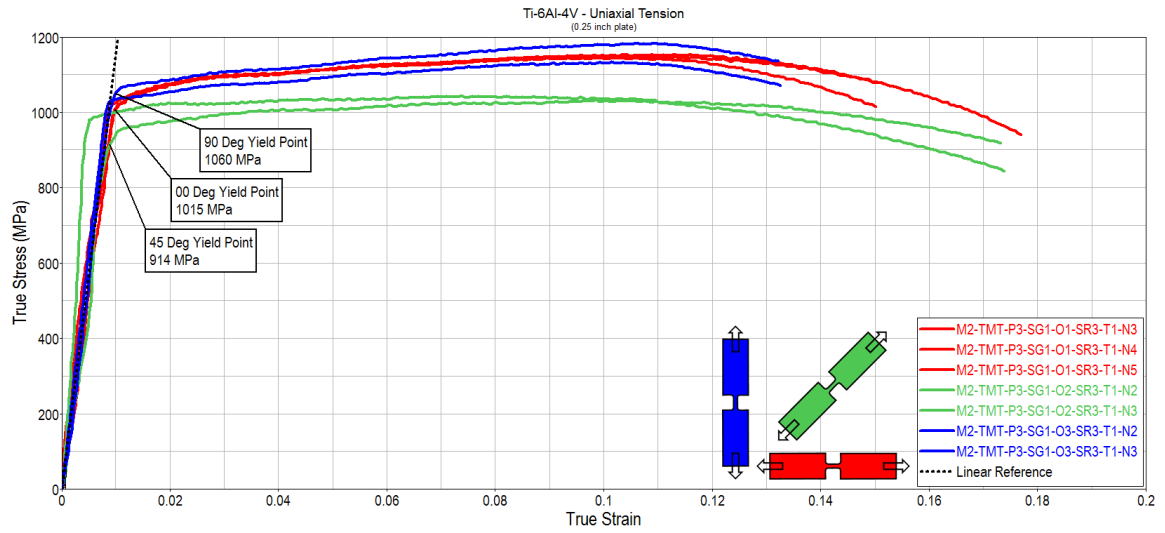


Figure 47: Ti-6Al-4V yield point

After the yield point is chosen, the elastic portion of the curve is removed so that only the plastic component remains. The plastic strain, ε_p , can be calculated for the input yield curve.

Equation 64: Plastic strain calculation

$$\varepsilon_p = \varepsilon - \frac{\sigma}{E}$$

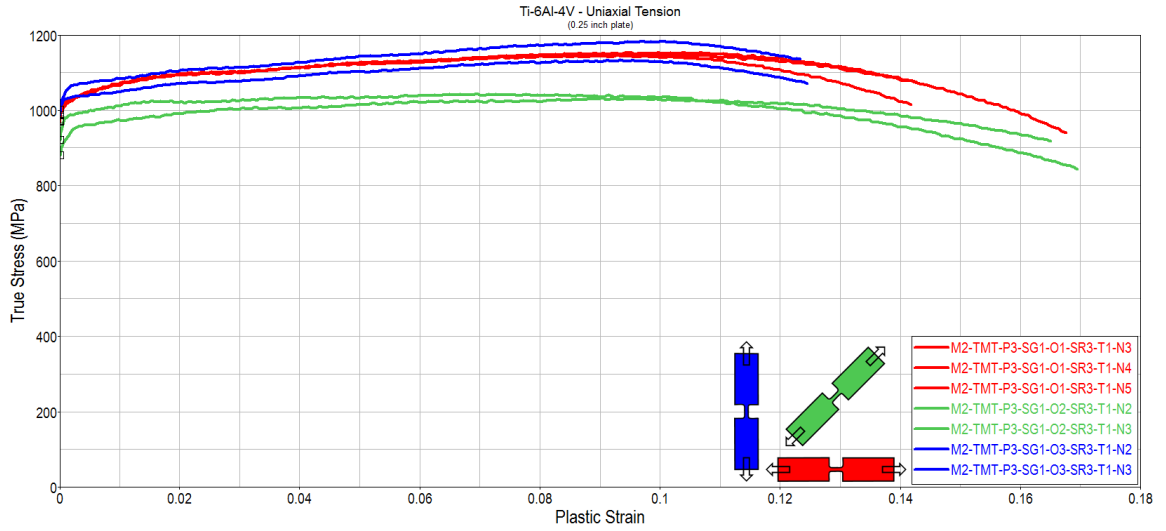


Figure 48: Ti-6Al-4V true stress vs. plastic strain

At this stage in the yield curve generation process, the flow stress after the necking point must be reevaluated against the initial assumptions. After necking, the cross sectional is much smaller in the localized region and therefore not constant in the area covered by the extensometer. Additionally, the transversal stresses develop after the initial necking point and additional stresses in the thickness direction will develop. Beyond the necking point, the specimen is no longer in a uniaxial tension state of stress.

Equation 65 shows the state of stress in the gage length before necking. Note that the only component of stress is the longitudinal stress and the von Mises stress is equal to the longitudinal stress (σ_l). Equation 66 shows the state of stress after the necking point. At this point, a transverse stress (σ_t) appears in the stress tensor and the von Mises stress does not equal the longitudinal stress. Lastly, Equation 67 shows the state of stress after necking and some localized thinning. At this point, some thickness stress (σ_{tt}) exists due to the material resistance against thinning.

Equation 65: State of stress before necking

$$\boldsymbol{\sigma} = \begin{pmatrix} \sigma_l & 0 & 0 \\ 0 & 0 & 0 \\ 0 & 0 & 0 \end{pmatrix} \quad \sigma_{vm} = \sigma_l$$

Equation 66: State of stress after diffuse necking

$$\boldsymbol{\sigma} = \begin{pmatrix} \sigma_l & 0 & 0 \\ 0 & \sigma_t & 0 \\ 0 & 0 & 0 \end{pmatrix} \quad \sigma_{vm} \neq \sigma_l$$

Equation 67: State of stress after local necking

$$\boldsymbol{\sigma} = \begin{pmatrix} \sigma_l & 0 & 0 \\ 0 & \sigma_t & 0 \\ 0 & 0 & \sigma_{tt} \end{pmatrix} \quad \sigma_{vm} \neq \sigma_l$$

Since any experimental data after the necking point cannot be used to generate an appropriate yield curve, only the data prior to necking can remain. To find the necking point, the derivative of the stress vs. strain curve was calculated and plotted together with the original experimental data [39]. This process may require some smoothing of the original data in order to get a smooth curve for the tangent modulus. Figure 49 shows an example of the process for determining the necking point of the 0-degree specimen. All of the stress and strain data beyond the necking point can be removed.

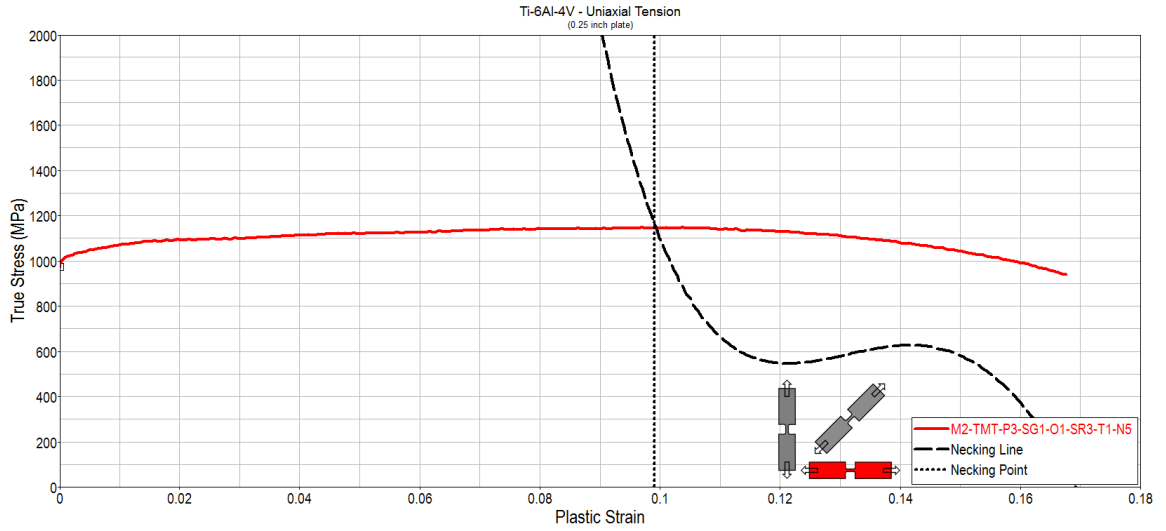


Figure 49: Ti-6Al-4V determination of the necking point for the 0-degree specimen

After the necking point is determined an extrapolation process is required to determine the part of the yield curve after the necking point. The extrapolated portion of the yield curve can be calculated from Equation 68 where: k , ε_e , and n are fitting parameters.

Equation 68: Yield curve extrapolation equation

$$\sigma = k(\varepsilon_e + \varepsilon_p)^n$$

The exponent, n , varies from 0 to 1 as the yield curve is expected to monotonically increase and have a monotonically decreasing tangent. Additionally, the transition between the true stress vs. true strain curve and the extrapolated curve should be continuous and smooth.

Equation 69: Yield curve continuous extrapolation

$$A = \sigma|_{\varepsilon=\varepsilon_0}, B = \varepsilon|_{\varepsilon=\varepsilon_0}$$

Equation 70: Yield curve smooth extrapolation

$$A = \sigma|_{\varepsilon=\varepsilon_0}, C = \frac{d\sigma}{d\varepsilon}|_{\varepsilon=\varepsilon_0}$$

Equation 69 and Equation 70 have three additional coefficients, A , stress at necking, B , plastic strain at necking and C , the slope (hardening modulus). Since there are three variables and only two boundary conditions, the extrapolation is not uniquely defined and one the parameter can be freely chosen. Typically, the parameter n is freely chosen and the other two parameters are calculated in Equation 71 and Equation 72. At the necking point, $A = C$ and therefore the extrapolation equation for parameter e can be simplified to $\varepsilon_e = n - B$.

Equation 71: Yield curve extrapolation equation for parameter k

$$k = A \left(\frac{An}{C} \right)^{-n}$$

Equation 72: Yield curve extrapolation equation for parameter e

$$\varepsilon_e = \frac{An}{C} - B$$

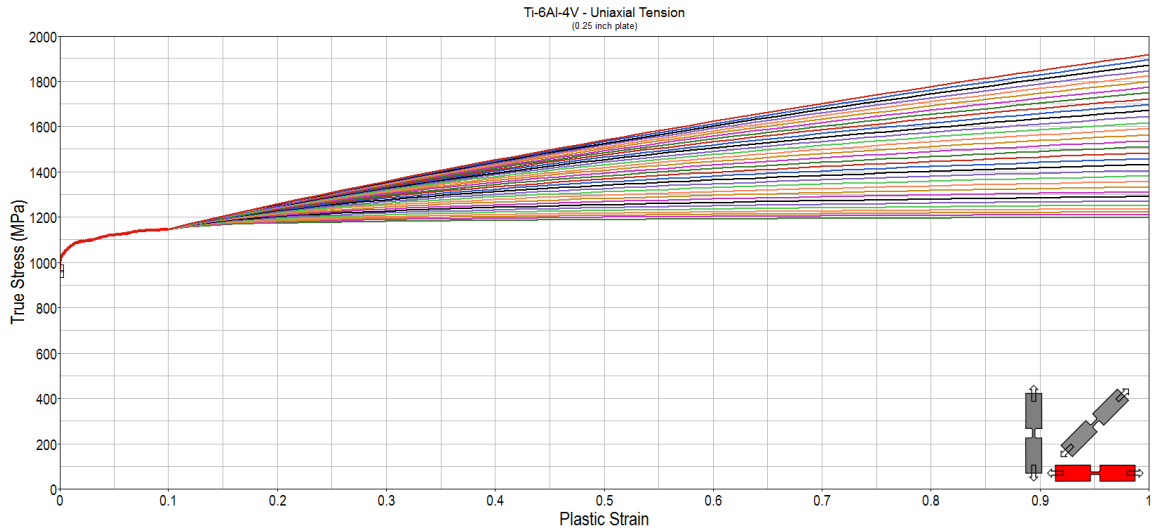


Figure 50: Ti-6Al-4V extrapolated yield curves for 0-degree specimen

For each specimen, 32 unique yield curves were generated and formatted as a LS-DYNA *DEFINE_CURVE keyword. A simulation was designed to replicate the uniaxial tension experiment. A finite element mesh of the tensile test specimen was created with 46,208 solid elements (0.2 mm element size). The dimensions of each specimen direction were applied to the finite element mesh so that the cross sectional area, gage length, and curvature were identical to the measured test values. By using the Tabulated Johnson-Cook material model in LS-DYNA, each individual yield curve was simulated and the results were analyzed. With this method, each specimen direction yield curve can be generated independently of the other specimen directions. After each yield curve was simulated, one candidate was selected to represent that material specimen direction. The results from the isotropic Tabulated Johnson-Cook material model are shown in Figure 52.

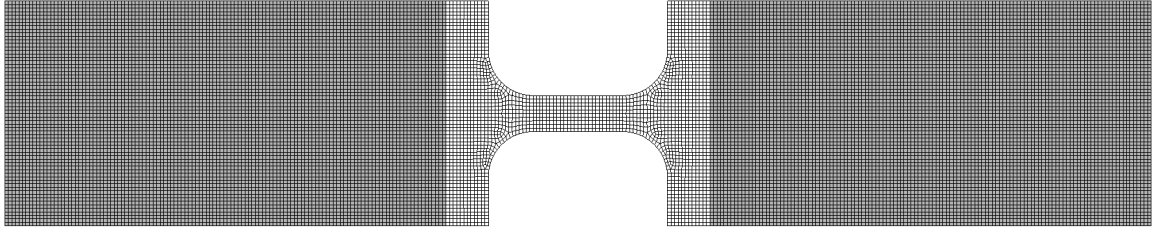


Figure 51: Ti-6Al-4V uniaxial tension specimen finite element mesh

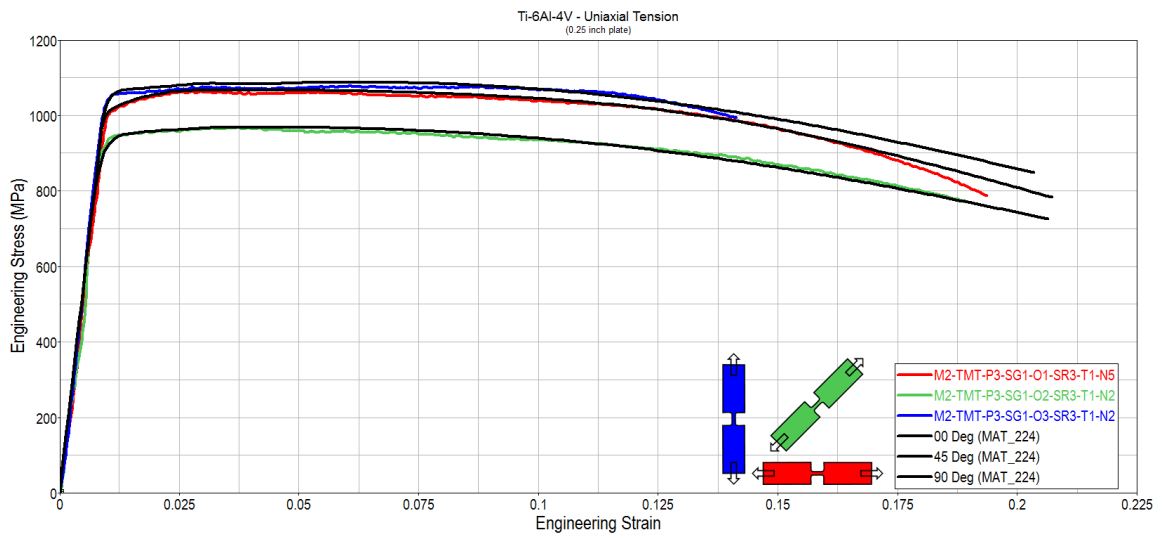


Figure 52: Ti-6Al-4V tension simulation results with Tabulated Johnson-Cook material model

Now that three independent tabulated yield curves have been selected to represent the 0-degree, 45-degree and 90-degree tension directions, they can be used in the anisotropic material model presented in this dissertation. The final selected yield curves for all the tension specimens are shown in Figure 53.

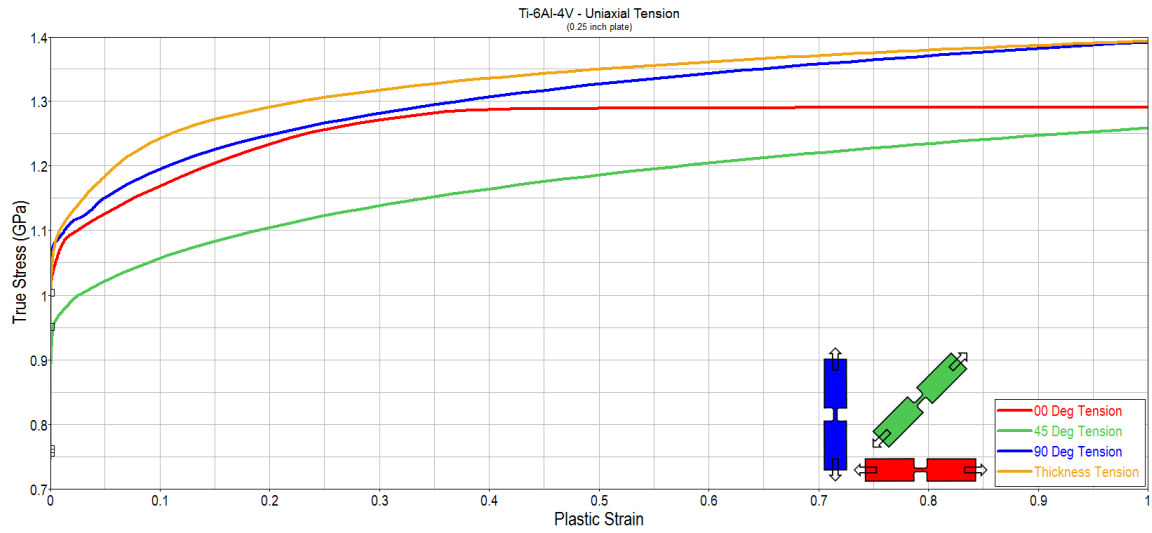


Figure 53: Ti-6Al-4V selected tension yield curves

Following the same procedure, the compressive yield curves for the 0-degree, 45-degree, 90-degree and thickness directions were generated for the Ti-6Al-4V plate. Figure 54 shows the final yield curves used to model each of the compression specimens individually. Figure 55 shows the results from the Tabulated Johnson-Cook material model using the yield curves generated in Figure 54.

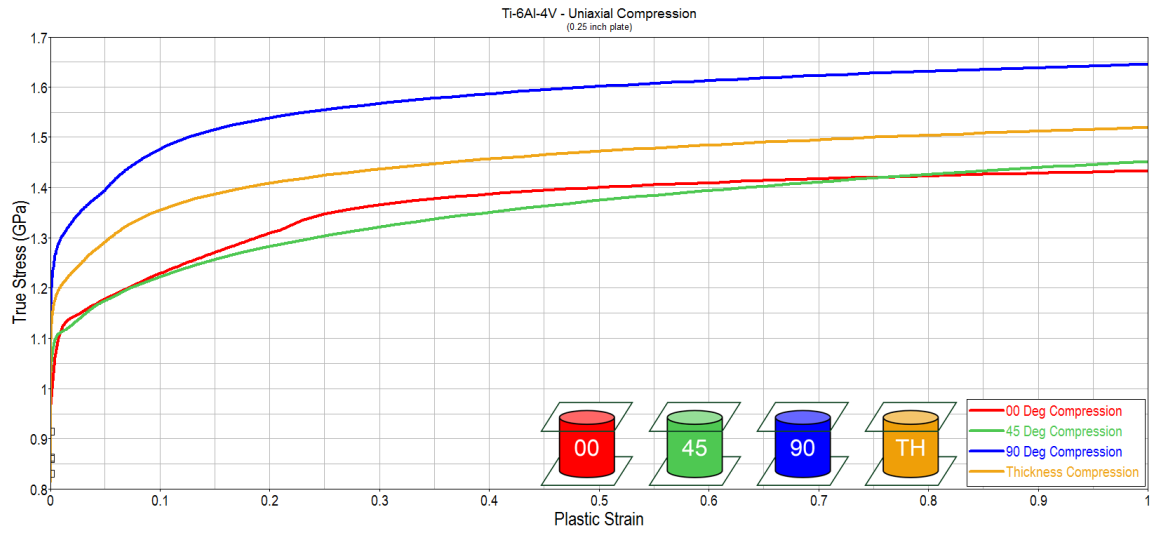


Figure 54: Ti-6Al-4V selected compression yield curves

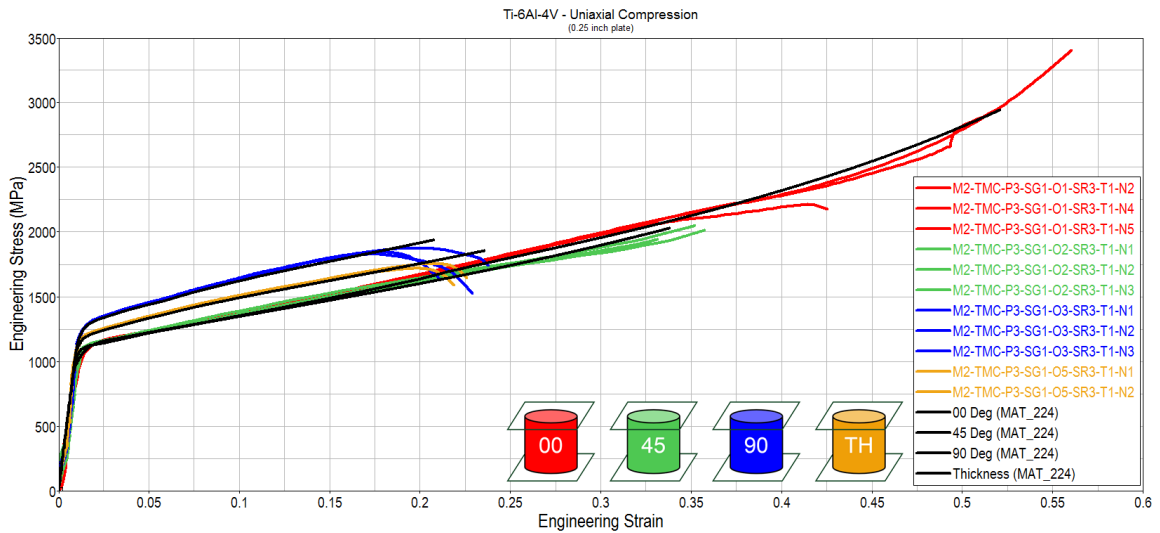


Figure 55: Ti-6Al-4V compression simulation results with Tabulated Johnson-Cook material model

Since the titanium plate used for the material tests was only 0.25 inches thick, it was not possible to manufacture a tension specimen in the thickness direction of the material. Therefore, a yield curve in the thickness direction was derived from the

relationship between the tension/compression yield curve in the 0-degree direction and the compression yield curve in the thickness direction. Equation 73 shows this derivation where: σ_{t-tt} is the tensile yield stress in the thickness direction, σ_{t-00} is the tensile yield stress in the 0-degree direction, σ_{c-00} is the compressive yield stress in the 0-degree direction and σ_{c-tt} is the compressive yield stress in the thickness direction.

Equation 73: Tension in thickness direction

$$\sigma_{t-tt}(\varepsilon_p) = \frac{\sigma_{t-00}(\varepsilon_p)}{\sigma_{c-00}(\varepsilon_p)} \sigma_{c-tt}(\varepsilon_p)$$

4.2.3 – Ti-6Al-4V Material Model Validation Program

With the input yield curves generated in section 4.2.2, a full anisotropic material model for Ti-6Al-4V can be compiled. This material is used to validate the tension and compression components of the model and therefore the yield curves in tension (Figure 53) and compression (Figure 54) are used. In order to verify each material direction, unique simulations are designed using the same material model input. The only difference between each model is the specimen dimensions, which are specified for each individual specimen, and the definition of the material axis in the material axis option (AOPT) portion of the model. The total material input is shown in Figure 56. The material axis options, for each specimen direction, is shown in Table 13 and Table 14. These options assume that the tension specimen is on the simulation x-y plane and pulled in the +x direction (thickness in the +z direction). For compression, the specimen sits on the simulation x-y plane and is pushed in the –z direction.

```

*MAT_TABULATED_JOHNSON_COOK_ORTHO_PLASTICITY
$ Ti-6Al-4V 00 DEG
$      MID      RO      E      PR      CP      TR      BETA      NUMINT
      2 4.4300E-6 100.00000 0.342000 540.00000 293.00000 1.000000 1.000000
$      T00R      T00T      LCF      LCG      LCH      LCI
      100      0      0      0      0      0
$      C00R      C00T      S45R      S45T      SFIEPM      NITER      AOPT
      200      300      2      200      2
$      T90R      T45R      TTHR      C90R      C45R      CTHR
      400      500      600      700      800      900
$      T90T      T45T      TTHT      C90T      C45T      CTHT
$      XP      YP      ZP      A1      A2      A3      MACF
      1.0      0.0      0.0
$      V1      V2      V3      D1      D2      D3      BETA
      0.0      1.0      0.0

```

Figure 56: Material input card for Ti-6Al-4V (0-degree material axis options)

Table 13: Ti-6Al-4V material axis options for each specimen direction in tension

Specimen direction	A1	A2	A3	D1	D2	D3
00 deg	1.0	0.0	0.0	0.0	1.0	0.0
45 deg	1.0	-1.0	0.0	1.0	1.0	0.0
90 deg	0.0	-1.0	0.0	1.0	0.0	0.0

Table 14: Ti-6Al-4V material axis options for each specimen direction in compression

Specimen direction	A1	A2	A3	D1	D2	D3
00 deg	0.0	0.0	1.0	0.0	-1.0	0.0
45 deg	0.0	1.0	1.0	0.0	-1.0	1.0
90 deg	0.0	1.0	0.0	0.0	0.0	1.0
Thickness	1.0	0.0	0.0	0.0	0.0	1.0

Each specimen was simulated using the same material model (with the exception of the material axis options) and the resulting engineering stress/strain was compared to the original test data described in section 4.2.1. These tensile specimen results are shown in Figure 57 and the compression specimen results are shown in Figure 58. It should be noted that there is some interaction between the three directions after necking occurs.

However, the influence of this seems to be small enough to be neglected in this case (and for the purposes of generating yield curves).

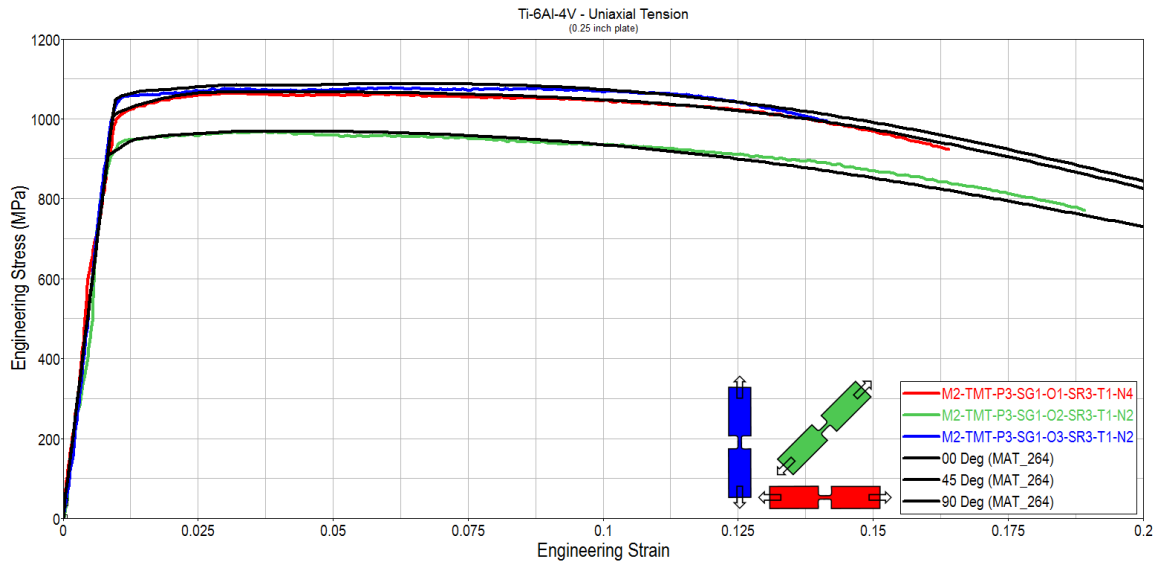


Figure 57: Ti-6Al-4V tension simulation results with anisotropic material model

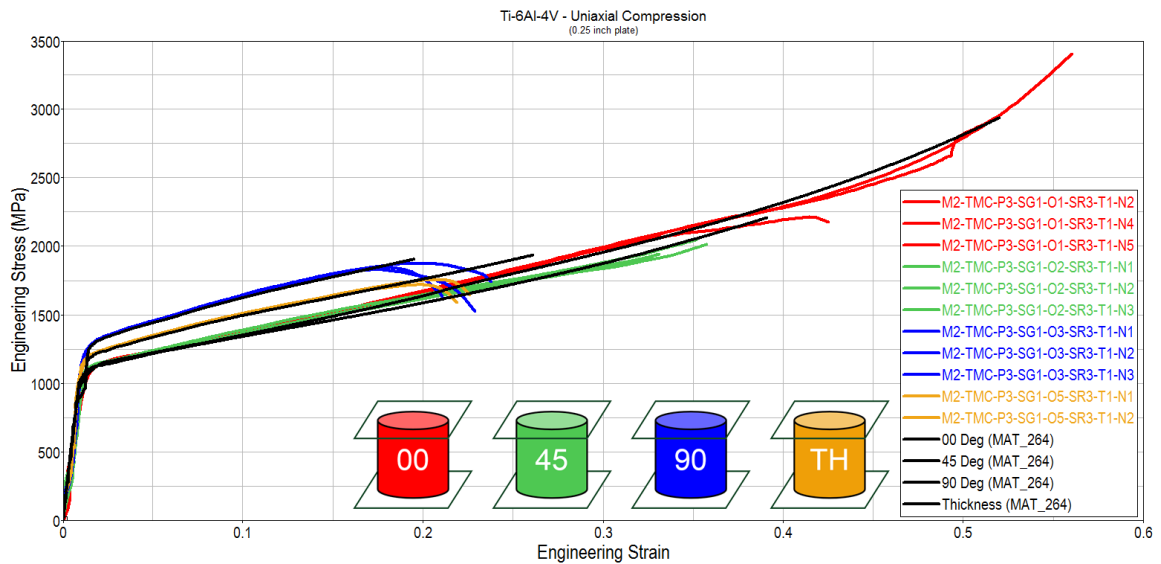


Figure 58: Ti-6Al-4V compression simulation results with anisotropic material model

4.2.4 – Ti-6Al-4V Ballistic Impact Simulations

To test the application and robustness of this material routine in a large finite element model, a simulation was designed to replicate a series of ballistic impact tests performed by the National Aeronautics and Space Administration (NASA) at the Glenn Research Center [16]. These tests consisted of a 381 mm x 381 mm Ti-6Al-4V plate with a thickness of 6.35 mm. These plates were mounted to a frame that had an inner diameter of 254 mm. A cylindrical projectile was manufactured with a diameter of 12.7 mm and a length of 22.225 mm. These projectiles were manufactured from an A2 tool steel material. This projectile was shot into the center of the plate from a gas gun at velocities ranging from 189 m/s to 278 m/s. Figure 59 shows a diagram of the experimental set-up and the projectile geometry.

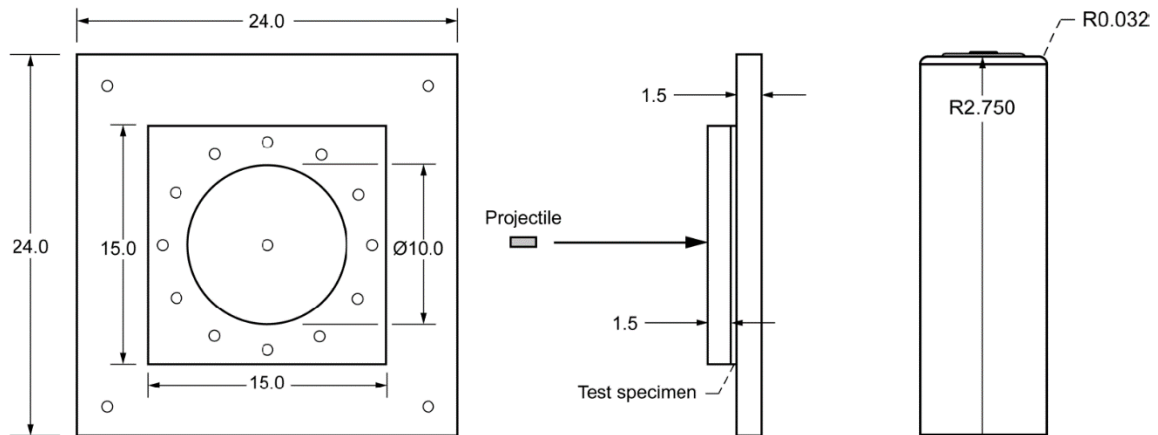


Figure 59: Ti-6Al-4V ballistic impact test set up [16]

Several high speed cameras were positioned around the area of impact to measure the velocity of the projectile prior to impact. If the projectile penetrated the plate specimen, then the exit velocity was also measured using a similar camera system.

To simulate this experiment, input yield curves for each material direction are required. In addition, since this material model is asymmetric, both tension and compression input yield curves should be used. Lastly, the strain rate and temperature effects for each direction can be factored into the model. Therefore, all 18 tables available in the material model input should be used to fully test the capabilities of this model.

At the time of this writing, a limited material testing data set exists for this 0.25 inch (6.35 mm) Ti-6Al-4V plate. While high strain rate and high temperature series tests have been performed in the 0-degree direction, they have not been conducted for the 45-degree, 90-degree and thickness directions. Therefore, these effects will be estimated for all directions based on the strain rate effects seen in a similar 0.5 (12.7 mm) inch Ti-6Al-4V plate. A scale factor can be determined for the high strain rates and high temperatures. These scale factors are applied to the quasi-static input yield curves for the alternative directions. For example, to determine the input yield curve for 45-degree direction at a strain rate of $1.0\text{E-}5$ /ms, the 0-degree input yield curve at $1.0\text{E-}5$ is first divided by the 0-degree input yield curve at the quasi-static strain rate. The average value (as a function of plastic strain) of that resulting division operation is then multiplied by the 45-degree quasi-static input yield curve (at all values of plastic strain). This operation can be duplicated for all available strain rates and temperatures.

Table 15: Strain rate input yield curve scale factors

Rate	QS	0.01	0.10	1.50	2.50	5.00	10.0	15.0	20.0	30.0	40.0	50.0
00T	1.0	1.007	1.032	1.086	1.105	1.135	1.189	1.417	1.87	2.32	2.79	3.24
00C	1.0	1.007	1.032	1.086	1.105	1.135	1.189	1.417	1.87	2.32	2.79	3.24
45T	1.0	1.007	1.032	1.086	1.105	1.135	1.189	1.417	1.87	2.32	2.79	3.24
45C	1.0	1.007	1.032	1.086	1.105	1.135	1.189	1.417	1.87	2.32	2.79	3.24
90T	1.0	1.007	1.032	1.086	1.105	1.135	1.189	1.417	1.87	2.32	2.79	3.24
90C	1.0	1.007	1.032	1.086	1.105	1.135	1.189	1.417	1.87	2.32	2.79	3.24
ThT	1.0	1.007	1.032	1.086	1.105	1.135	1.189	1.417	1.87	2.32	2.79	3.24
ThC	1.0	1.007	1.032	1.086	1.105	1.135	1.189	1.417	1.87	2.32	2.79	3.24

Table 16: Temperature input yield curve scale factors

Temp	RT	473	673	873
00T	1.0	0.727	0.553	0.461
00C	1.0	0.727	0.553	0.461
45T	1.0	0.727	0.553	0.461
45C	1.0	0.727	0.553	0.461
90T	1.0	0.727	0.553	0.461
90C	1.0	0.727	0.553	0.461
ThT	1.0	0.727	0.553	0.461
ThC	1.0	0.727	0.553	0.461

Table 15 shows the scale factor for each strain rate (1/ms) in each material direction. The green scale factors are curves that have been generated directly from test data. The red scale factors have been estimated from the strain rate effects seen in a similar 0.5 inch Ti-6Al-4V plate. Table 16 shows the scale factor for each temperature (K) in each material direction (00 Tension, 00 Compression, 45 Tension, etc.)

Since all of the directional data is not available at high temperatures and strain rates, and this data is derived, the resulting inputs may not resemble reality. With this

approach, it is assumed that the strain rate and temperature sensitivities are not directionally dependent. It is just as possible that each direction has a unique strain rate and temperature dependency, which would not be simulated here. Ideally, material tests at high strain rates and high temperatures would have been performed for each material direction. This would allow for a full material characterization using this model. Since this data is derived, and not based on physical tests, the result of the ballistic simulation may not be necessarily predictive. The purpose of this simulation is to test the robustness and scalability of this model as well as to compare it to similar isotropic models with similar inputs.

The full anisotropic material input for the Ti-6Al-4V plate is shown in Figure 60. Tables 100, 300, 500, 700, 800, 900, 1000, 1100 and 1200 are the strain rate dependent yield curve tables for 0-degree tension, 0-degree compression, 45-degree shear, 90-degree tension, 45-degree tension, thickness tension, 90-degree compression, 45-degree compression and thickness compression. Tables 200, 400, 600, 1300, 1400, 1500, 1600, 1700 and 1800 are the temperature dependent yield curve tables for the 0-degree tension, 0-degree compression, 45-degree shear, 90-degree tension, 45-degree tension, thickness tension, 90-degree compression, 45-degree compression and thickness compression. Additionally, the failure model is adapted from previous research with a similar Ti-6Al-4V plate [39]. This failure model is based on a surface which is a function of triaxiality and Lode parameters (Table 3000). Additionally, the effect of strain rate (Table 4000) and temperature (Table 5000) are also incorporated into the failure model. Lastly, this model includes mesh regularization for failure (Table 6000). The failure model used in

this research was developed for a similar Ti-6Al-4V plate (0.5 inch). The development of this failure model is described in a Federal Aviation Administration report [39]. No changes or alterations are made to this failure model, even though it was developed for a different titanium plate.

Figure 61 is the isotropic material input card which will be used to compare to the isotropic Tabulated Johnson-Cook material model directly. This implementation uses the 0-degree tension rate and temperature input yield curves along with the previously described failure model.

*MAT_TABULATED_JOHNSON_COOK_ORTHO_PLASTICITY								
\$	MID	RO	E	PR	CP	TR	BETA	NUMINT
	1	4.4300E-6	100.00000	0.342000	526.30000	293.00000	0.800000	1.000000
\$	T00R	T00T	LCF	LCG	LCH	LCI		
	100	200	3000	4000	5000	6000		
\$	C00R	C00T	S45R	S45T		SFIEPM	NITER	AOPT
	300	400	500	600		2.5	100	2
\$	T90R	T45R	TTHR	C90R	C45R	CTHR		
	700	800	900	1000	1100	1200		
\$	T90T	T45T	THTT	C90T	C45T	CTHT		TOL
	1300	1400	1500	1600	1700	1800		0.001
\$	XP	YP	ZP	A1	A2	A3	MACF	
				1.0	0.0	0.0		
\$	V1	V2	V3	D1	D2	D3	BETA	
				0.0	1.0	0.0		

Figure 60: Anisotropic material input card for Ti-6Al-4V ballistic simulation

*MAT_TABULATED_JOHNSON_COOK_ORTHO_PLASTICITY								
\$	MID	RO	E	PR	CP	TR	BETA	NUMINT
	1	4.4300E-6	100.00000	0.342000	526.30000	293.00000	0.800000	1.000000
\$	T00R	T00T	LCF	LCG	LCH	LCI		
	100	200	3000	4000	5000	6000		
\$	C00R	C00T	S45R	S45T		SFIEPM	NITER	AOPT
	100	200				2.5	100	2
\$	T90R	T45R	TTHR	C90R	C45R	CTHR		
	100	100	100	100	100	100		
\$	T90T	T45T	TTHT	C90T	C45T	CTHT		TOL
	200	200	200	200	200	200		0.001
\$	XP	YP	ZP	A1	A2	A3	MACF	
				1.0	0.0	0.0		
\$	V1	V2	V3	D1	D2	D3	BETA	
				0.0	1.0	0.0		

Figure 61: Isotropic material input card to Ti-6Al-4V ballistic simulation

The plate and projectile is modeled with solid elements with a mesh size of 0.2 mm (around the impact area). The projectile consists of 106,480 solid elements. The plate is modeled with 944,944 solid elements. The outer boundary condition is modeled as a perfectly rigid and fixed edge. Since the test report describes the projectiles as having no “evidence of plasticity or macro deformation”, the A2 tool steel was modeled as an elastic element with no plastic deformation. This projectile is positioned so that it is pointed at the center of the specimen plate and normal to the surface of the plate. The initial velocity of the projectile is set based on the impact velocity described in the test report.

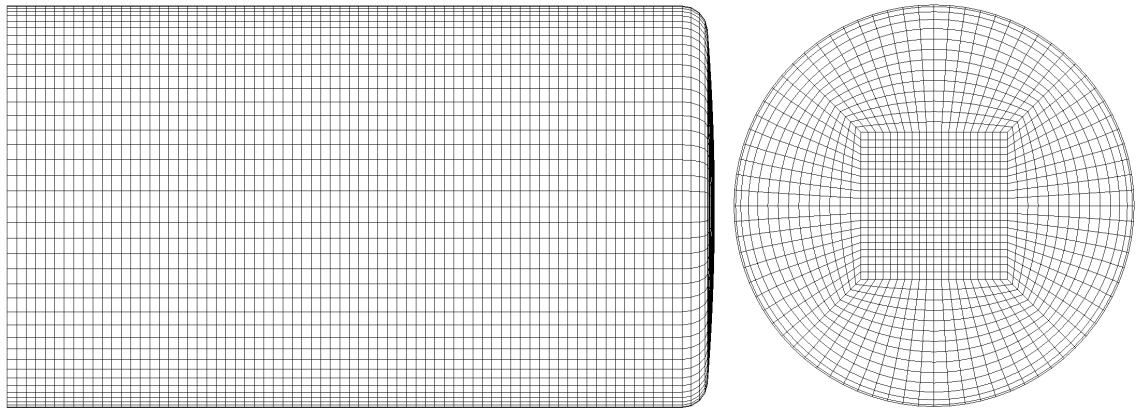


Figure 62: Ballistic projectile mesh

The first series of ballistic simulations was to see how the isotropic implementation of this model compared to the original (isotropic) tabulated Johnson-Cook material model. To accomplish this comparison, all of the anisotropic inputs for the material model were based on the 0-degree tension input tables. Therefore, only the 0-degree tension (with strain rate and temperature dependency) were used in both this anisotropic model and the original tabulated Johnson-Cook models. The simulations were initialized with initial projectile velocities of 229 m/s and 278 m/s.

For each simulation, the internal energy and the eroded (or failed) element internal energy was compared. Additionally, the velocity of the projectile as a function of simulation time was also compared for each material model. The contour of plastic strain at a specific simulation time was also compared for each model.

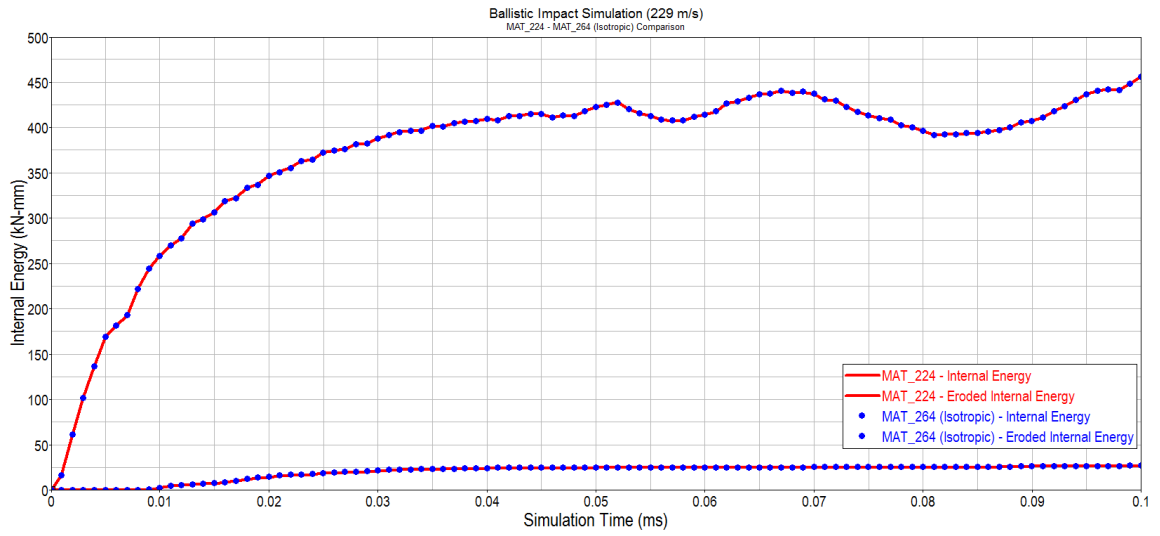


Figure 63: Comparison of isotropic models (internal energy) – 229 m/s initial velocity

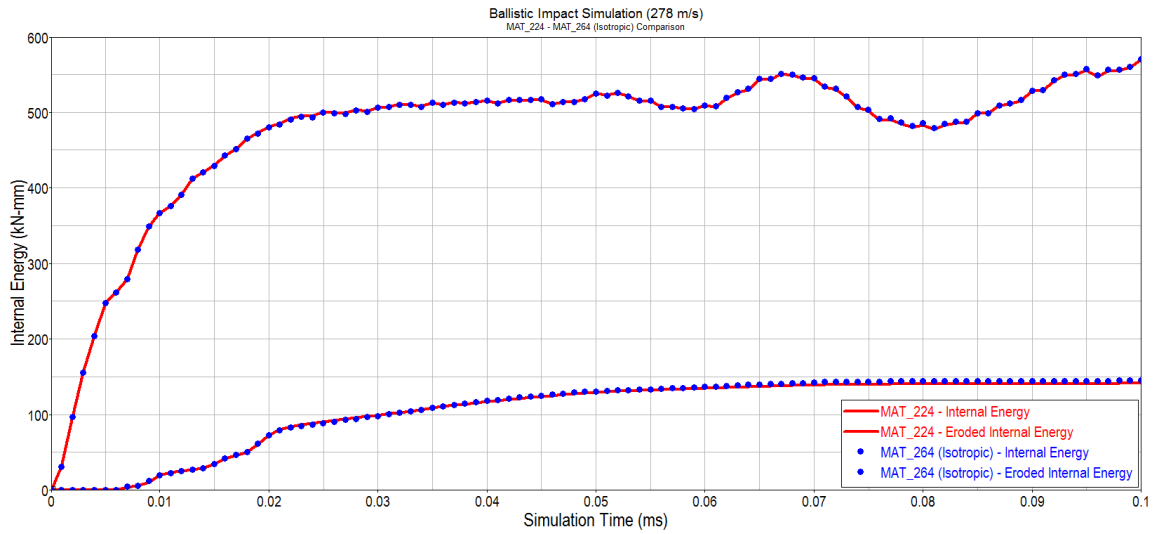


Figure 64: Comparison of isotropic models (internal energy) – 278 m/s initial velocity

Figure 63 and Figure 64 show the internal and eroded internal energies for the 229 m/s and 278 m/s impacts. It is clear from these results that the isotropic implementation of this model is equivalent to the original isotropic Tabulated Johnson-Cook model.

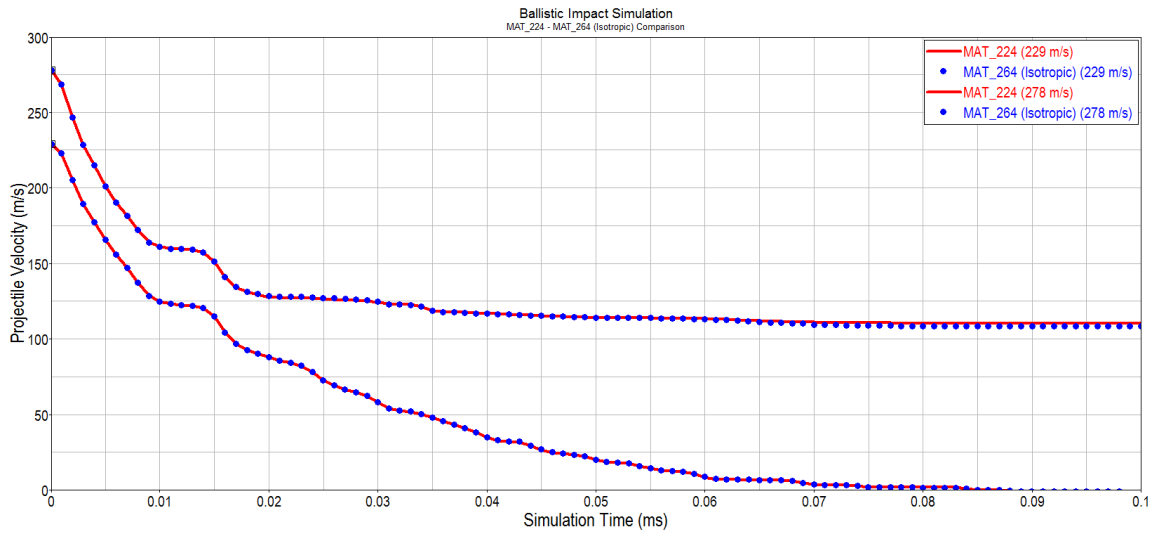


Figure 65: Comparison of isotropic models (projectile velocity)

Figure 65 shows the projectile velocities as a function of simulation time for both the 229 m/s and 278 m/s initial impact velocities. It is clear that the projectile is contained by the Ti-6Al-4V plate in the 229 m/s initial velocity simulation, but has penetrated the plate in the 278 m/s initial velocity simulation. It is also clear that both the isotropic implementation of this model and the isotropic Tabulated Johnson-Cook model result in similar velocity profiles.

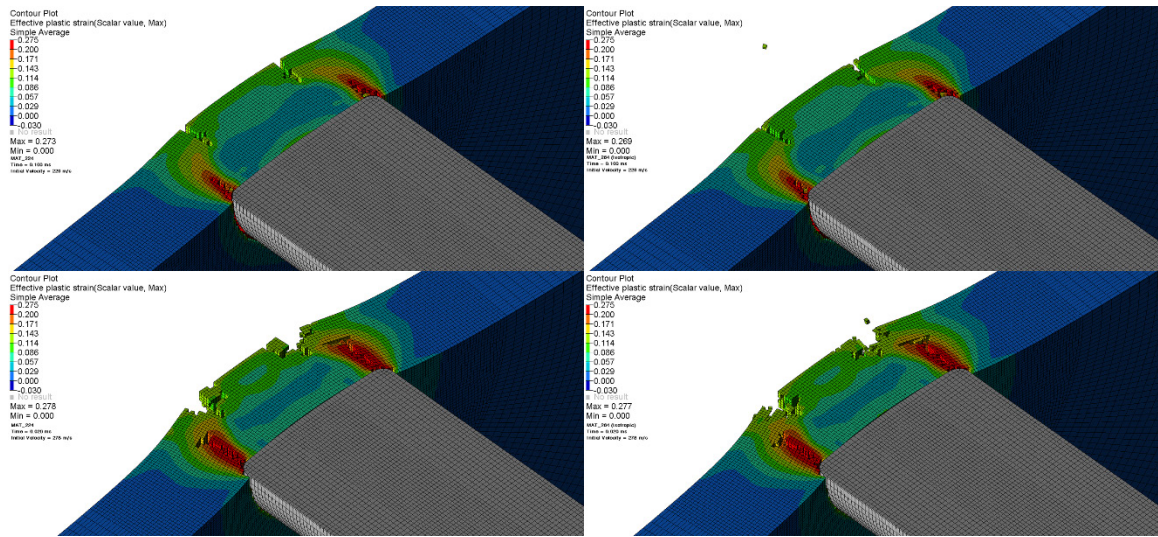


Figure 66: Comparison of isotropic models (plastic strain)

Figure 66 shows the contour of effective plastic strain for each of the simulations. The top portion of Figure 66 shows the results of the 229 m/s initial velocity for the original Tabulated Johnson-Cook model (left) and the isotropic implementation of this model (right). The bottom portion of Figure 66 is shown in a similar configuration, but for the initial velocity of 278 m/s.

The results from these comparison simulations show that the internal energies, projectile velocities, and plastic strains are very similar. This result is expected because the isotropic implementation of the anisotropic material model should be nearly identical to the original isotropic tabulated Johnson-Cook material model. This new anisotropic model should be backwards compatible if the user does not input any anisotropic data.

The second series of ballistic simulations is designed to compare the fully anisotropic version of this material model with the isotropic Tabulated Johnson-Cook material model. The simulation set-up for this series is exactly the same as the previous

series except the full material model shown in Figure 60 is used instead of the isotropic implementation. Again, the 229 m/s and 278 m/s impact velocities are used for comparison.

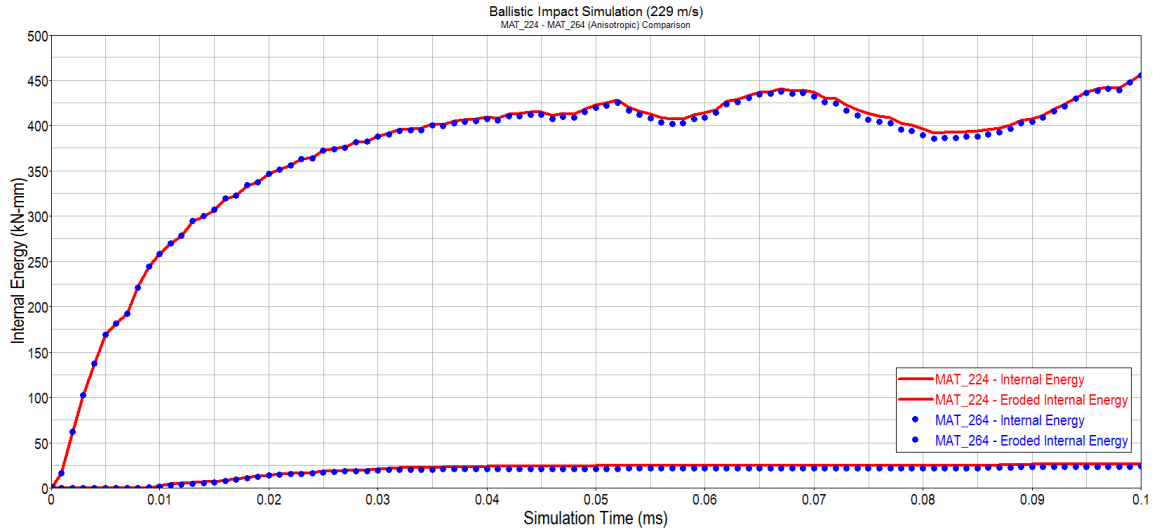


Figure 67: Comparison of isotropic and anisotropic models (internal energy) – 229 m/s initial velocity

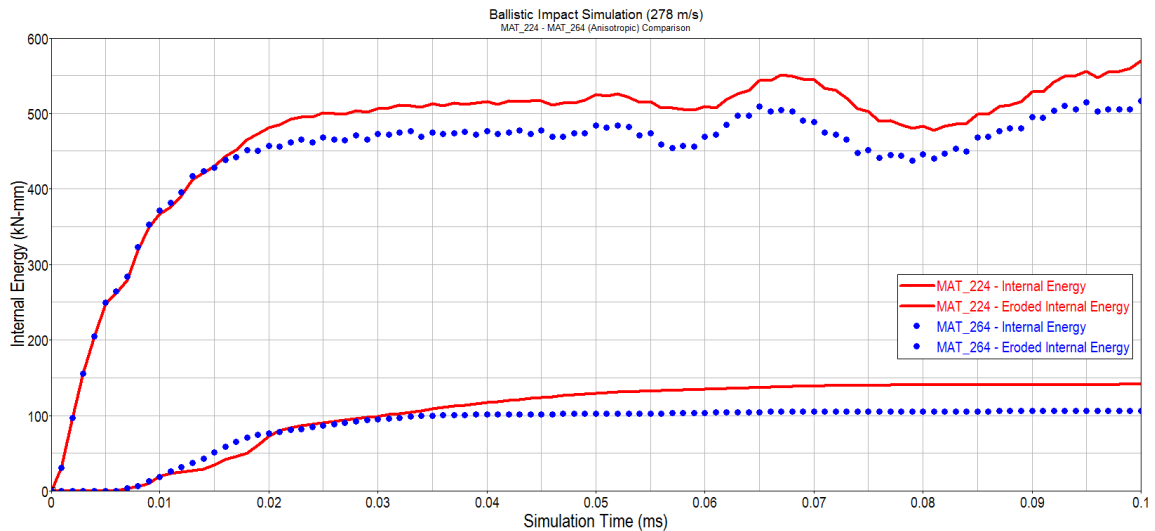


Figure 68: Comparison of isotropic and anisotropic models (internal energy) – 278 m/s initial velocity

Figure 67 and Figure 68 both show differences between the internal (and eroded internal) energies of each simulation. This is due to the fact that one simulation uses an anisotropic material model while the other uses an isotropic material model. This variation is more obvious in the higher velocity impact, where the projectile fully penetrates the plate, than in the lower velocity impact.

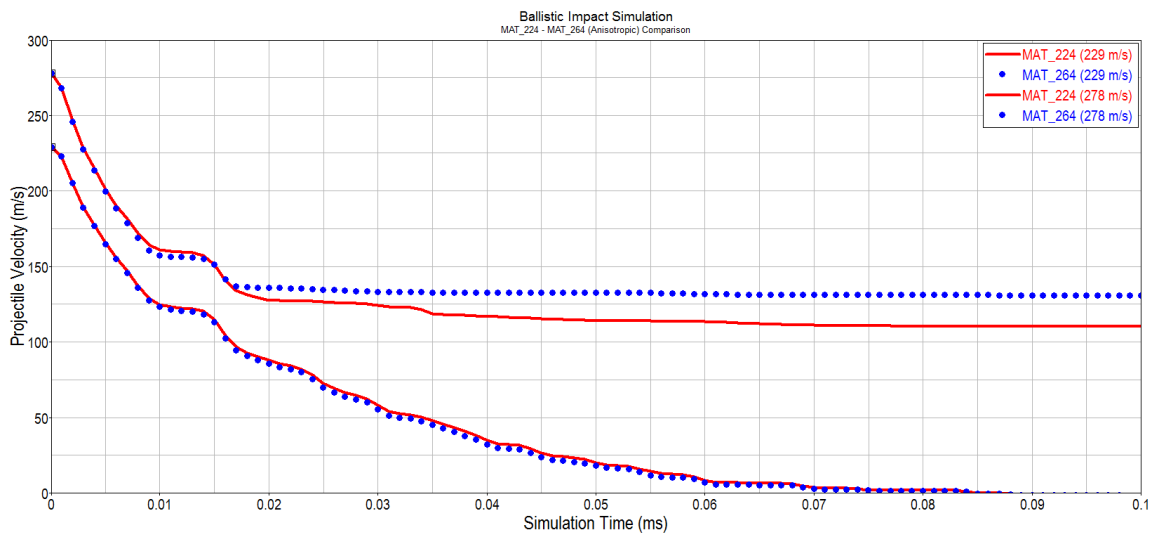


Figure 69: Comparison of isotropic and anisotropic models (projectile velocity)

Figure 69 shows the resulting projectile velocity profiles for both the 229 m/s and 278 m/s simulations. While there is only a slight difference between the anisotropic and isotropic models in the 229 m/s impact simulation, there is considerable difference between the two 278 m/s simulations.

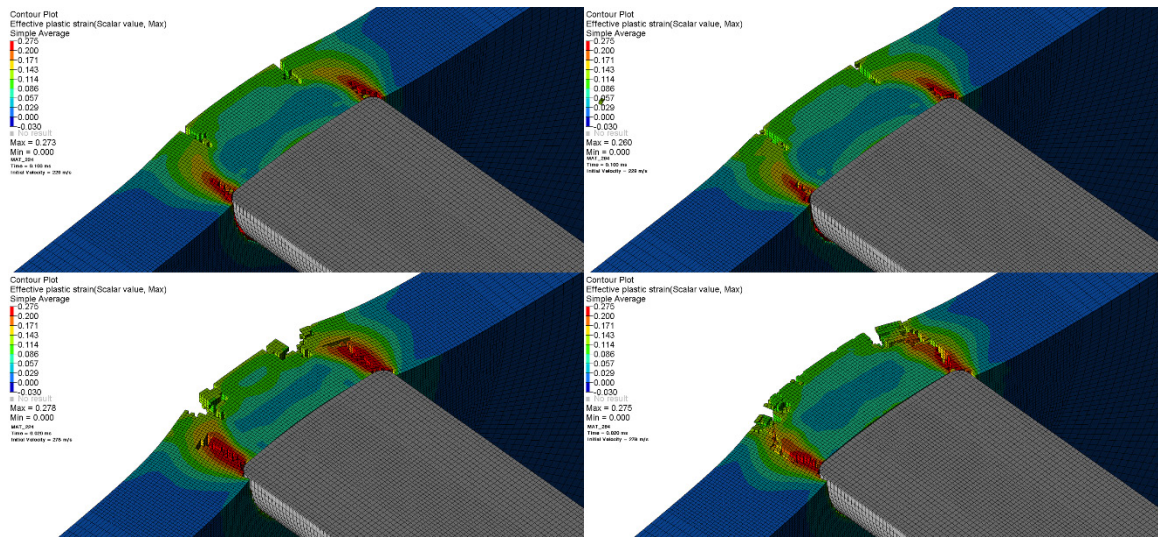


Figure 70: Comparison of isotropic and anisotropic models (plastic strain)

Figure 70 shows the plastic strain comparison of the isotropic (left) and anisotropic (right) models at 229 m/s (top) and 278 m/s (bottom). It is clear that there is a difference between the two material models, which is expected since one model is isotropic and the other is anisotropic. For example, the anisotropic simulation at 278 m/s impact velocity seems to have penetrated the plate in less time than the isotropic model. This can become important when attempting to design components that are meant to contain certain projectiles.

Another interesting comparison between the isotropic and anisotropic models is the distribution of stress on the impacted side of the titanium-alloy plate. Figure 71 and Figure 72 show this stress distribution at a specific simulation time. Figure 71 is the contour plot of the von Mises stress using the isotropic Tabulated Johnson-Cook material model. This model results in an even distribution of stress around the area of the impact. In comparison, Figure 72 shows the stress distribution using this anisotropic material

model. It is clear that the stress is larger in the 0-degree and 90-degree directions and lower in the 45-degree (and 135 degree) directions. This difference in stress distribution is expected because the input yield stress is lower for the 45-degree (and 135 degree) directions while the yield stress is higher in the 0-degree and 90-degree directions. This result confirms that the directionality of this model is working as expected.

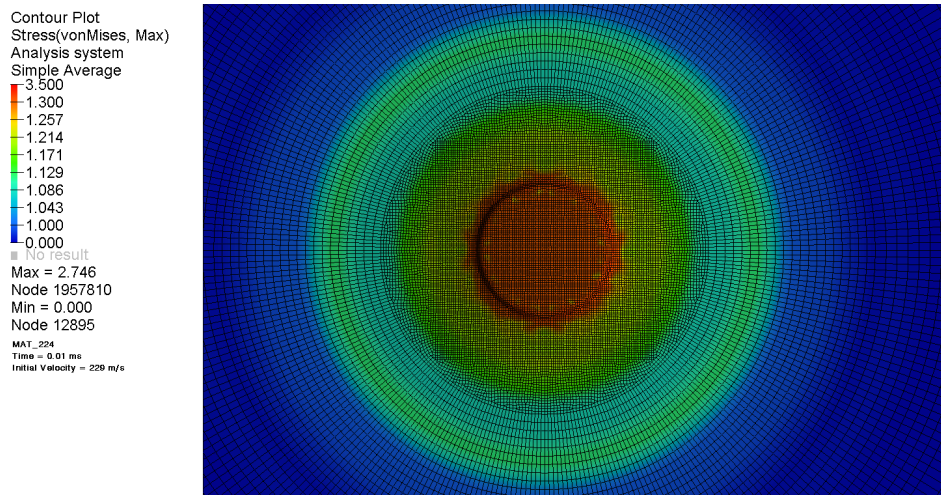


Figure 71: von Mises stress distribution with isotropic material model - 229 m/s

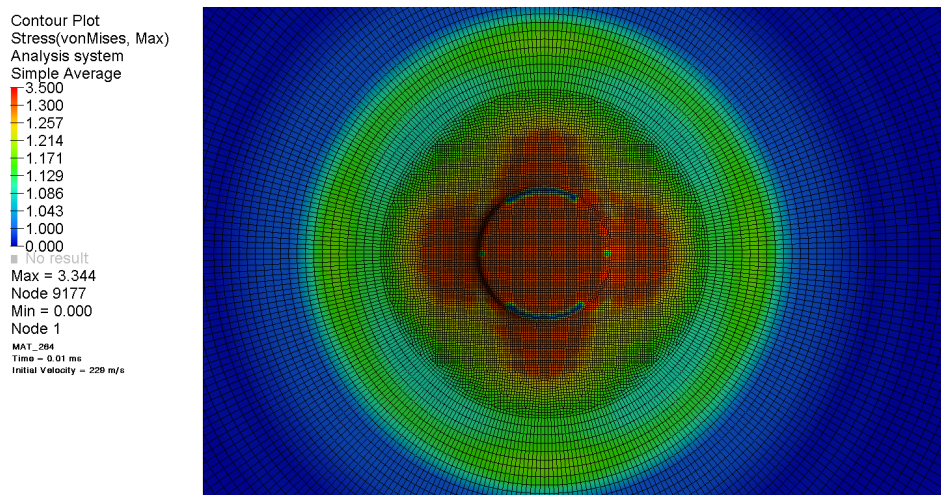


Figure 72: von Mises stress distribution with anisotropic material model - 229 m/s

These ballistic impact simulations show that this material model is robust and applicable to large finite element models (over 1 million elements). This is important because many models, such as aerospace turbine and full automobile models, consists of hundreds of thousands, if not millions, of elements. It is important to make sure that the development of new material models can be used in these large simulations. Furthermore, these ballistic simulations show that there is a considerable difference between isotropic and anisotropic material models. The projectile velocity, internal energies, eroded internal energies and the stress distributions are different between these two models. This implies that the use of anisotropic models may have a better ability to fully characterize and predict the material response under these load cases. Lastly, these ballistic simulations show that this anisotropic material model is backwards compatible with older versions of the Tabulated Johnson-Cook material model.

CHAPTER 5 - SUMMARY, CONCLUSIONS, AND RECOMMENDATIONS FOR FUTURE RESEARCH

This research has resulted in a new computational material model for simulating dynamic solid mechanics problems. This model is necessary to the engineering community because of the lack of tabulated anisotropic material models in finite element codes (such as LS-DYNA). In most finite element codes, to simulate an anisotropic material, engineers were forced to approximate the material with isotropic material models or utilize non-tabulated material models designed for forming applications. In contrast, this material model has been developed for use in dynamic impact or crash simulations.

The objective of this research is to design a material subroutine within an existing finite element code that can allow for the simulation of asymmetric and anisotropic materials. This means that the material exhibits different flow stress in tension, compression and shear. Additionally, the material can exhibit different flow stress in multiple different directions. These directions are usually with respect to the direction of the extrusion or rolling.

Not only is this material asymmetric and directional, but it is also fully tabulated. This means that the flow stress can be provided directly from test data as a function of the plastic strain. This is different than most existing material models that have limited flexibility of defining the flow stress. This method allows the user to have more control over the material response and therefore more precise results.

In addition to directionality and the ability to model asymmetric materials, this material model also allows for strain rate and temperature dependency. The formulation of this model is based on the Johnson-Cook and Tabulated Johnson-Cook material models that incorporate both strain rate and temperature effects. In this new model, the strain rate effects are tabulated and can be applied to each material direction. For a given strain rate, an input yield curve is provided. Thermal softening is also incorporated into this material model. Like the strain rate effects, the thermal effects are tabulated and applied to each material direction.

The methodology of this new material model has been clearly defined in this research. The yield function, which is a combination of the Hill (1948) yield function and an orthotropic Lode parameter have been developed and defined. The flow rule has also been discussed and described. This material incorporates that associated flow rule and its formulation is clearly described in this research. Convexity conditions for the yield functions have also been defined mathematically and checks have been implemented to ensure that the yield surface is convex in most situations.

The theory behind the new material model was implemented using the FORTRAN programming language and used in conjunction with the LS-DYNA finite element code. This research provides a full overview of the material routine in the form of a flow chart. In addition to the typical results provided by a finite element simulation, this research provides the ability to visualize the yield surface using the output parameters from the simulation.

Single element simulations were used to verify the material model. First, an isotropic implementation of this model was compared to similar isotropic tabulated Johnson-Cook models. It is shown that this model is backward compatible and when isotropic inputs are used, this model provides the same results as the previous isotropic models. Next, single element simulations were used to verify that the material response is equal to the input yield curve in each material direction (tension and compression). This verification step shows that the material is directional and asymmetric. Single elements were also used to verify the material response in varying strain rates. A tabulated input with different input yield curves for multiple strain rates were used to show that the strain rate dependency portion of the material model is correct. Lastly, single elements were used to verify the thermal component of this material routine. Simulations were conducted to show how the temperature of the element can change as a function of plastic work and that the stress of that element corresponds to the input yield curves as a function of temperature. Using all of these single element simulations, all the major components of the material model are verified.

Specimen testing of a rolled aluminum plate were used to generate inputs for this material model and test its capabilities. This aluminum plate was chosen because it exhibits some anisotropy in tension. Input yield curves were generated for each direction and were combined using this new material model. With a single model, each of the tension specimen directions were simulated and compared to the test data. It was shown that the resulting stress-strain relationships of the simulation matched the test data reasonably well for each material direction.

Specimen testing of a rolled titanium plate were also used to validate this material model. This material was chosen because it exhibits both anisotropy and asymmetry. Therefore, both tension and compression specimen test data were used to generate a material input for the titanium. Using this material model, all of the specimens (both in tension and compression) were simulated and compared to the original test data. All of the simulation results show a reasonable comparison to the test data.

Lastly, this model was tested with a large (1M+ element) finite element model to test the robustness of the routine. A model was created to simulate a high velocity impact between a projectile and a 0.25 inch titanium plate. Strain rate and temperature effects for the plate were assumed and a full implementation of the material model was generated. The impact was simulated and compared to similar isotropic material models.

The most significant contributions of this work to the engineering and scientific field are the development and verification of:

- A tabulated model with directional asymmetry.
- An anisotropic model with tabulated rate effects.
- An anisotropic model with tabulated thermal softening.
- A new material model that is able to simulate large (1M+ element) finite element models.
- An (industrial) anisotropic model characterization for two material plates (Al-2024 and Ti-64).

It is recommended that more research be completed on anisotropic materials. For example, while this model does include isotropic failure, it does not allow for anisotropic

failure. Anisotropic failure could be added to this material model, or as a separate additional routine, to more accurately define the failure as a function of material direction. Additionally, it is recommended that more research be conducted using this material routine with additional test data. For example, the strain rate and temperature data used in this research was assumed and not provided from actual material tests. Additional directional high rate and high temperature testing needs to be conducted in order to fully utilize all of the new and novel capabilities of this material model. Finally, an implementation of this material model for plane stress conditions (shell elements) would allow for it's use in many other (automotive) applications.

APPENDIX

This appendix provides some MATLAB routines that can be used to visualize the yield surface discussed in section 3.3. To use this code, you will need to save history variables 21-37 as a *.csv file for all time steps for a given element. This file should be called SURFACE.csv.

```
clear,clc
r=[]; t1=[];
% Inport history variable data
[time,c1,c2,c3,r00,r45,r90,b03,b04,b10,d03,d04,d10,F,G,H,N,sigy] =
ImportData('SURFACE.csv', 1, 500);
% Solve for yield function
a=0:.01:2*pi;
for j=1:10:length(time);
for alpha=0:.01:2*pi;
hill=sqrt(F(j).*tan(alpha).^2+G(j)+H(j)*(1-tan(alpha)).^2);
theta1=(27.*(2/27+(b03(j)+b04(j))./27.*tan(alpha).^3-1/9.*tan(alpha)-
1/9.*b04(j).*tan(alpha).^2))./(2.*(1+tan(alpha).^2-
tan(alpha)).^(3/2)));
theta2=(27.*(2/27+(d03(j)+d04(j))./27.*tan(alpha).^3-1/9.*tan(alpha)-
1/9.*d04(j).*tan(alpha).^2))./(2.*(1+tan(alpha).^2-
tan(alpha)).^(3/2)));
sigxx=sigy/(hill.*(c1(j)+c2(j).*theta1+c3(j).*theta2.^2));
if (alpha>=pi/2 && alpha<=3*pi/2)
sigxx=-sigy/(hill.*(c1(j)-c2(j).*theta1+c3(j).*theta2.^2));
end
r=[r sigxx/cos(alpha)];
end
% Plot surface for multiple time steps
[X,Y] = pol2cart(a,r(j,:));
r=[];
createfigure2(X, Y)
xlim([-5 5])
ylim([-5 5])
str = sprintf('%i',j);
print('-dpng',str)
close all
end
```

Routine for plotting 00-90 plane


```

clear,clc
% Initialize vectors
r=[]; t1=[];
% Import history variable data
[time,c1,c2,c3,r00,r45,r90,b03,b04,b10,d03,d04,d10,F,G,H,N,sigy] =
ImportData('SURFACE.csv', 1, 500);
% Solve for yield function
a=0:.01:2*pi;
for j=1:10:length(time);
for alpha=0:.01:2*pi;
hill=sqrt(G(j)+H(j)+2.*N(j).*(tan(alpha).^2));
theta1=(27.*(2/27-tan(alpha).^2./3.*(1-
2.*b10(j))))./((1+3.*tan(alpha).^2).^3/2));
theta2=(27.*(2/27-tan(alpha).^2./3.*(1-
2.*d10(j))))./((1+3.*tan(alpha).^2).^3/2));
sigxx=sigy/(hill.*(c1(j)+c2(j).*theta1+c3(j).*theta2.^2));
sigxx=sigy/(hill.*(c1(j)+c2(j).*theta1+c3(j).*theta2.^2));
if (alpha>=pi/2 && alpha<=3*pi/2)
sigxx=-sigy/(hill.*(c1(j)-c2(j).*theta1+c3(j).*theta2.^2));
end
r=[r sigxx/cos(alpha)];
end
% Plot surface for multiple time steps
[X,Y] = pol2cart(a,r(j,:));
r=[];
createfigure2(X, Y)
xlim([-5 5])
ylim([-5 5])
str = sprintf('%i',j);
print('-dpng',str)
close all
end

```

Routine for plotting 00-45 Shear plane

```

clear,clc
% Initialize vectors
r=[]; t1=[];
% Import history variable data
[time,c1,c2,c3,r00,r45,r90,b03,b04,b10,d03,d04,d10,F,G,H,N,sigy] =
ImportData('SURFACE.csv', 1, 500);
% Solve for yield function
a=0:.01:2*pi;
for j=1:10:length(time);
for alpha=0:.01:2*pi;
hill=sqrt(F(j).*tan(alpha).^2+G(j)*(tan(alpha)-1).^2+H(j));
theta1=(27.*(2/27+(1+2.*b04(j)-b03(j))./27.*tan(alpha).^3-
1/9.*tan(alpha)-1/9.*b04(j).*tan(alpha).^2))./(2.*(1+tan(alpha).^2-
tan(alpha)).^(3/2)));
theta2=(27.*(2/27+(1+2.*d04(j)-d03(j))./27.*tan(alpha).^3-
1/9.*tan(alpha)-1/9.*d04(j).*tan(alpha).^2))./(2.*(1+tan(alpha).^2-
tan(alpha)).^(3/2)));
sigxx=sigy/(hill.*(c1(j)+c2(j).*theta1+c3(j).*theta2.^2));
if (alpha>=pi/2 && alpha<=3*pi/2)
sigxx=-sigy/(hill.*(c1(j)-c2(j).*theta1+c3(j).*theta2.^2));
end
r=[r sigxx/cos(alpha)];
end
% Plot surface for multiple time steps
[X,Y] = pol2cart(a,r(j,:));
r=[];
createfigure2(X, Y)
xlim([-5 5])
ylim([-5 5])
str = sprintf('%i',j);
print('-dpng',str)
close all
end

```

Routine for plotting 00-Thickness plane

```

function createfigure2(X1, Y1)
figure1 = figure('Color',[1 1 1],'Position', [30, 30, 950, 950]);
axes1 = axes('Parent',figure1,'YTick',[-5 -4 -3 -2 -1 0 1 2 3 4
5],'YGrid','on',...
    'XGrid','on','XTick',[-5 -4 -3 -2 -1 0 1 2 3 4 5],...
    'PlotBoxAspectRatio',[1 1 1],...
    'FontSize',20);
zlim(axes1,[-5 5]);
box(axes1,'on');
hold(axes1,'all');
plot(X1,Y1,'LineWidth',2);
title('MAT-264 Yield Surface','FontSize',20);
xlabel('0-degree Stress','FontSize',20);
ylabel('Thickness Stress','FontSize',20);
axis equal
axis square

```

Plotting subroutine (createfigure2)

```

function
[time,c1,c2,c3,r00,r45,r90,b03,b04,b10,d03,d04,d10,F,G,H,N,sigy] =
importfile1(filename, startRow, endRow)
delimiter = ',';
if nargin<=2
    startRow = 1;
    endRow = inf;
end
formatSpec = '%s%s%s%s%s%s%s%s%s%s%s%s%s%s%s%s%s%[\n\r]';
fileID = fopen(filename,'r');
dataArray = textscan(fileID, formatSpec, endRow(1)-startRow(1)+1,
'Delimiter', delimiter, 'HeaderLines', startRow(1)-1,
'ReturnOnError', false);
for block=2:length(startRow)
    frewind(fileID);
    dataArrayBlock = textscan(fileID, formatSpec, endRow(block)-
startRow(block)+1, 'Delimiter', delimiter, 'HeaderLines',
startRow(block)-1, 'ReturnOnError', false);
    for col=1:length(dataArray)
        dataArray{col} = [dataArray{col};dataArrayBlock{col}];
    end
end
fclose(fileID);
raw = repmat({''},length(dataArray{1}),length(dataArray)-1);
for col=1:length(dataArray)-1
    raw(1:length(dataArray{col}),col) = dataArray{col};
end
numericData = NaN(size(dataArray{1},1),size(dataArray,2));

%(CONTINUED)

```

```

for col=[1,2,3,4,5,6,7,8,9,10,11,12,13,14,15,16,17,18]
    rawData = dataArray{col};
    for row=1:size(rawData, 1);
        regexstr = ' (?<prefix>.*?)(?<numbers>([-\
]*(\d+[\,\,]*)+[\.\.]{0,1}\d*[eEdD]{0,1}[-+]*\d*[iI]{0,1}))|([-\
]*(\d+[\,\,]*)*[\.\.]{1,1}\d+[eEdD]{0,1}[-+]*\d*[iI]{0,1})) (?<suffix>.*)';
        try
            result = regexp(rawData{row}, regexstr, 'names');
            numbers = result.numbers;
            invalidThousandsSeparator = false;
            if any(numbers==' ');
                thousandsRegExp = '^ \d+?( \, \d{3}) * \. {0,1} \d * $';
                if isempty(regexp(thousandsRegExp, ' ', 'once'));
                    numbers = NaN;
                    invalidThousandsSeparator = true;
                end
            end
            if ~invalidThousandsSeparator;
                numbers = textscan(strrep(numbers, ' ', ' '), '%f');
                numericData(row, col) = numbers{1};
                raw{row, col} = numbers{1};
            end
        catch me
        end
    end
end
R = cellfun(@(x) ~isnumeric(x) && ~islogical(x),raw); % Find non-
numeric cells
raw(R) = {NaN}; % Replace non-numeric cells
time = cell2mat(raw(:, 1));
c1 = cell2mat(raw(:, 2));
c2 = cell2mat(raw(:, 3));
c3 = cell2mat(raw(:, 4));
r00 = cell2mat(raw(:, 5));
r45 = cell2mat(raw(:, 6));
r90 = cell2mat(raw(:, 7));
b03 = cell2mat(raw(:, 8));
b04 = cell2mat(raw(:, 9));
b10 = cell2mat(raw(:, 10));
d03 = cell2mat(raw(:, 11));
d04 = cell2mat(raw(:, 12));
d10 = cell2mat(raw(:, 13));
F = cell2mat(raw(:, 14));
G = cell2mat(raw(:, 15));
H = cell2mat(raw(:, 16));
N = cell2mat(raw(:, 17));
sigy = cell2mat(raw(:, 18));

```

Subroutine for importing history variables (inportfile1)

REFERENCES

- [1] M. Buyuk, *Development of a Tabulated Thermo-Viscoplastic Material Model with Regularized Failure for Dynamic Ductile Failure Prediction of Structures Under Impact Loading*, Washington, DC: The George Washington University, 2013.
- [2] G. S. Cole and A. M. Sherman, "Lightweight Materials for Automotive Applications," *Materials Characterization*, vol. 35, pp. 3-9, 1995.
- [3] V. Banthia, J. Miller, R. Valisetty and E. Winter, "Lightweighting of Cars with Aluminum for Better Crashworthiness," *SAE Transactions: Journal of Materials and Manufacturing*, vol. 102, no. 5, 1993.
- [4] P. Weissler, "2015 F-150 aluminum body creates challenge for auto body shops," *Automotive Engineering Magazine*, 18 November 2014.
- [5] A. Smith, P. DuBois and T. Borvall, "Development of an Anisotropic Material Model for the Simulation of Extruded Aluminum under Transient Dynamic Loads," in *10th European LS-DYNA Conference*, Wurzburg, Germany, 2015.
- [6] A. Haufe, P. DuBois, F. Neukamm and M. Feucht, "GISSMO - Material Modeling with a sophisticated Failure Criteria," in *LS-DYNA Developer Forum*, Stuttgart, Germany, 2011.
- [7] K. S. Carney, C. Lawrence and D. V. Carney, "Aircraft Engine Blade-Out Dynamics," in *7th International LS-DYNA User Conference*, Stuttgart, Germany, 2009.
- [8] National Transportation Safety Board, "Aircraft Accident Report: Uncontained Engine Failure Delta Air Lines Flight 1288 McDonnell Douglas MD-88, N927DA Pensacola, Florida," Washington DC, 1996.
- [9] Australian Transport Safety Bureau, "In-flight uncontained engine failure Airbus A380-842, VH-OQA," ATSB, Canberra, Australia, 2010.
- [10] Federal Aviation Administration, "Failure Modeling of Titanium 6Al-4V and Aluminum 2024-T3 with the Johnson-Cook Material Model," United States Department of Transportation, Washington, DC, 2003.
- [11] Livermore Software Technology Corporation, *LS-DYNA Keyword User's Manual Material Models*, r:5991 ed., vol. II, Livermore, California, 2015.
- [12] Federal Aviation Administration, "Development of a New Metal Material Model in LS-DYNA," United States Department of Transportation, Washington, DC, 2014.

- [13] K. Sengoz, *Development of A Generalized Isotropic Yield Surface for Pressure Insensitive Metal Plasticity Considering Yield Strength Differential Effect in Tension, Compression and Shear Stress States*, Washington, DC: The George Washington University, 2015.
- [14] J. D. Seidt, *Plastic Deformation and Ductile Fracture of 2024-T351 Aluminum Under Various Loading Conditions*, Columbus, OH: The Ohio State University, 2010.
- [15] J. T. Hammer, *Plastic Deformation and Ductile Fracture of Ti-6Al-4V under Various Loading Conditions*, Columbus, OH: The Ohio State University, 2014.
- [16] J. M. Pereira, D. M. Revilock, B. A. Lerch and C. R. Ruggeri, "Impact Testing of Aluminum 2024 and Titanium 6Al-4V for Material Model Development," U.S. National Aeronautics and Space Administration / U.S. Department of Transportation (FAA), Cleveland, OH, 2013.
- [17] F. Mollica and A. R. Srinivasa, "A general framework for generating convex yield surfaces for anisotropic metals," *Acta Mechanica*, vol. 154, no. 1-4, pp. 61-84, 2002.
- [18] M. H. Tresca, "Mémoire sur l'écoulement des corps solides soumis à de fortes pressions," Paris, *Comptes rendus Hebdomadaires des seances de l'Academie des Sciences*, 1864, pp. 754-758.
- [19] R. von Mises, "Mechanik der festen Körper in plastisch-deformablen Zustand," *Göttin. Nachr. Math. Phys.*, vol. 1, pp. 582-592, 1913.
- [20] F. Barlat and J. Lian, "Plastic Behavior and Stretchability of Sheet Metals. Part I: A Yield Function for Orthotropic Sheets Under Plane Stress Conditions," *International Journal of Plasticity*, vol. 5, no. 1, pp. 51-66, 1989.
- [21] R. Hill, "A theory of the yielding and plastic flow of anisotropic metals," in *Proc. Royal Society London*, 1948, pp. 281-297.
- [22] R. Hill, "Theoretical Plasticity of Textured Aggregates," *Mathematical Proceedings of the Cambridge Philosophical Society*, vol. 85, no. 179, 1979.
- [23] A. V. Hershey, "The Plasticity of an Isotropic Aggregate of Anisotropic Face Centered Cubic Crystals," *Journal of Applied Mechanics*, vol. 76, p. 241, 1954.
- [24] W. F. Hosford, "A Generalized Isotropic Yield Criterion," *Journal of Applied Mechanics*, vol. 39, p. 607, 1972.
- [25] J. L. Bassani, "Yield Characterization of Metals with Transversely Isotropic Plastic Properties," *International Journal of Mechanical Science*, vol. 19, p. 651, 1977.
- [26] M. Gotoh, "A Theory of Plastic Anisotropy Based on a Yield Function of Fourth Order (Plane Stress State)," *International Journal of Mechanical Science*, vol. 19, p. 505, 1977.
- [27] R. W. H. W. F. Logan, "Upper Bound Anisotropic Yield Locus Calculations Assuming $\langle 111 \rangle$ -Pencil Glide," *International Journal of Mechanical Sciences*, vol. 22, p. 419, 1980.

- [28] S. E. G. P. P. Jones, "A Generalized Quadratic Flow Law for Sheet Metals," *Metallurgical and Materials Transactions*, vol. 15A, p. 129, 1984.
- [29] B. Budianski, "Anisotropic Plasticity of Plane-Isotropic Sheets," in *Mechanics of Material Behavior*, Amsterdam, Elsevier Science Publishers, 1984, p. 15.
- [30] F. Barlat, J. C. Brem, J. W. Yoon, K. Chung, R. E. Dick, D. J. Lege, F. Pourboghrat, S. H. Choi and E. Chu, "Plane stress yield function for aluminum allow sheets - part 1: threory," *International Journal of Plasticity*, vol. 19, no. 9, pp. 1297-1319, 2003.
- [31] F. Barlat, Y. Maeda, K. Chung, M. Yanagawa, J. C. Brem, Y. Hayashida, D. J. Lege, K. Matsui, S. J. Murtha, S. Hattori, R. C. Becker and S. Makosey, "Yield Function Development for Aluminum Alloy Sheets," *Journal of the Mechanical and Physics of Solids*, vol. 45, no. 11-12, pp. 1727-1763, 1997.
- [32] M. Fleischer, T. Borrvall and K.-U. Bletzinger, "Experince from using recently implemented enhancements for Material 36 in LS-DYNA 971 performing a virtual tensile test," in *6th Europlean LS-DYNA Users' Conference*, Gothenburg, 2007.
- [33] H. Aretz, "A non-quadratic plane stress yield function for orthotropic sheet metals," *Journal of Materials Processing Technology*, vol. 168, no. 1, pp. 1-9, 2005.
- [34] R. Hill, "Constitutive Modeling of Orthotropic Plasticity In Sheet Metals," *Journal of the Mechanics and Physics of Solids*, vol. 38, no. 3, pp. 405-417, 1989.
- [35] O. Cazacu and F. Barlat, "A criterion for description of anisotropy and yield differential effects in pressure-insensitive metals," *Journal of International Plasticity*, vol. 20, pp. 2027-2045, 2004.
- [36] A. S. Khan and S. Huang, *Continuum Theory of Plasticity*, John Wiley & Sons, 1995.
- [37] W. W. Feng and W. H. Yang, "General and Specific Quadratic Yield Functions," *Journal of Composites, Technology and Research*, vol. 6, no. 1, pp. 19-21, 1984.
- [38] C. Zengtao and C. Butcher, in *Micromechanics Modeling of Ductile Fracture*, Springer, 2013, pp. 79-80.
- [39] S. Haight, L. Wang, P. Du Bois, K. Carney and C.-D. Kan, "Development of a Titanium Alloy Ti6Al4V Material Model Used in LS-DYNA," U.S. Department of Transportation, Washington, DC., 2015.
- [40] V. Tuninetti, G. Gilles, O. Milis, T. Pardoen and A. M. Habraken, "Anisotropy and tension-compression asymmetry modeling of the room temperature plastic response of Ti-6Al-4V," *International Journal of Plasticity*, vol. 67, pp. 53-68, 2014.

BIOGRAPHY

Sean Harrison Haight graduated from Westview High School, San Diego, California, in 2005. In 2009, he received his Bachelor of Science from Texas Christian University in Mechanical Engineering. In 2012, he received his Master of Science from The George Washington University in Transportation Safety Engineering.